Technical Physics, Vol. 45, No. 3, 2000, pp. 285–289. Translated from Zhurnal Tekhnicheskoĭ Fiziki, Vol. 70, No. 3, 2000, pp. 1–5.

THEORETICAL AND MATHEMATICAL PHYSICS

Enhanced Response to a Signal from an Ensemble of Interacting Bistable Elements

S. A. Reshetnyak

Lebedev Physical Institute, Russian Academy of Sciences, Leninskiĭ pr. 53, Moscow, 117924 Russia

Received August 13, 1998; in final form, March 19, 1999

Abstract—A one-dimensional ensemble comprising a large number of interacting bistable elements was studied analytically. Formulas for a noiseless and a noise-driven response to a signal were derived for the steady-state case. Contrasting them with each other testifies to the enhancement of the response if noise is present in the ensemble. The response of the ensemble is found to exceed that of a single element by a quantity that exponentially rises with the coupling constant. It was inferred that the interaction of bistable elements makes stochastic resonance more pronounced. © *2000 MAIK "Nauka/Interperiodica"*.

INTRODUCTION

There is currently great interest in a phenomenon known as stochastic resonance (SR). Predicted in [1], SR was first observed in bistable optical systems [2, 3]. The bistability of a nonlinear dynamical system is favorable to the amplification of a weak periodic signal through its interaction with noise. SR has also become a subject of studies in solid-state physics (in the context of tunnel diodes [4] or Josephson junctions [5]), chemical physics [6], and biology (models of stimulated neurons [7]). Since SR has proven to be a widespread phenomenon, it is likely to be discovered in other fields of science.

In this connection, it should be pointed out that SR has been adequately explored only in isolated bistable systems [8–10]. It is therefore interesting to look at the case of coupled bistable systems. Numerical analysis suggests that interaction promotes SR [11]. SR manifests itself in anomalous enhancement of either system sensitivity, the signal-to-noise ratio, or the Fourier image of the autocorrelation function as the noise intensity increases in a certain frequency range. However, the essential feature of SR is an enhanced response of a noisy system to a signal in comparison with the response of its noiseless version.

This paper presents analytic formulas for a steady-state response from a one-dimensional ensemble of interacting bistable elements to a weak external field in the presence and absence of noise action. The two responses are contrasted with each other. The equations concerned are identical to a one-dimensional finite-difference Ginzburg–Landau equation. It will be demonstrated that the noise-driven response exceeds the noiseless response by a term that exponentially grows with the coupling constant. Thus, interaction between bistable elements may significantly amplify the signal-to-noise ratio.

NOISELESS RESPONSE

Consider a one-dimensional ensemble (chain) of N interacting bistable elements. The underlying system of equations is

$$\frac{d\eta_n}{dt} = -U'_n + g(\eta_{n+1} - 2\eta_n + \eta_{n-1}) + F\cos(\omega t), \quad (1)$$

where

$$U_n = -\frac{a}{2}\eta_n^2 + \frac{b}{4}\eta_n^4$$

is the potential of an element; a is the height of the potential barrier for the element; g is a factor representing the interaction between neighboring elements (coupling constant); F and ω are the amplitude and the frequency of an external field, respectively; t is time; and $n = 1, 2, \ldots, N$.

We place cyclic conditions on the chain boundaries as follows:

$$\eta_{N+1} = \eta_1, \quad \eta_N = \eta_0. \quad (2)$$

They mean that the first element interacts with the last and also the second element. It is convenient to introduce the dimensionless quantities $x_n = \eta_n\sqrt{b/a}$. Then (1) becomes

$$\frac{dx_n}{dt} = -\frac{\partial W}{\partial x_n} + h\cos(\omega t),$$
$$W = \sum_{n=1}^{N}(V_n - gx_nx_{n+1}), \quad (3)$$
$$V_n = -\frac{a-2g}{2}x_n^2 + \frac{a}{4}x_n^4,$$

where W is the potential function of the chain $h = F\sqrt{b/a}$. The quantities z_n will be called order parameters.

The chain is stable in the vicinity of points z_n, where W is minimum. Such points can be found from

$$-\frac{\partial W}{\partial x_n}\bigg|_{x_n = z_n} = a(z_n - z_n^3) + g(z_{n+1} - 2z_n + z_{n-1}) = 0. \quad (4)$$

We will consider bistable systems with small coupling constants: $g \ll a$. In this case, it possible to solve (4) via a power series in g. If $g = 0$, then $z_n = \sigma_n = \pm 1$. In a first approximation with respect to g,

$$z_n = \sigma_n + \frac{g}{2a}\Delta\sigma_n, \quad (5)$$

where $\Delta\sigma_n = \sigma_{n+1} - 2\sigma_n + \sigma_{n-1}$.

It can be shown that the second differential d^2W is positive near the points z_n and W does have local minima there. Starting from its initial state, the chain relaxates to the points of stable equilibrium, z_n. If an external field with a strength $h \ll a$ is applied to the chain, the motion is also confined to the neighborhood of z_n. Consequently, the chain response to the field is a solution of (3) in the form

$$x_n = \sigma_n + y_n, \quad |y| \ll 1.$$

Small deviations y_n can be found from the linearized version of (3):

$$\frac{dy_n}{dt} = -2ay_n + g(y_{n+1} + (-2y_n) + y_{n-1}) + g\Delta\sigma_n + h\cos(\omega t). \quad (6)$$

Any solution of (6) is the sum of the general solution to the related homogeneous equation and a particular solution to the inhomogeneous equation. The general solution is

$$y_n^{(0)} = \sum_\alpha C_\alpha e_n^{(\alpha)} \exp(\mu_\alpha t). \quad (7)$$

Here, C_α are constants determined by initial conditions, and $e_n^{(\alpha)}$ and μ_α are the eigenvectors and the eigennumbers of the relaxation matrix R_{nm}, respectively:

$$\sum_{m=1}^{N} R_{nm} e_m^{(\alpha)} = \mu_\alpha e_n^{(\alpha)}, \qquad R_{nn} = -2(a+g), \quad R_{n,n-1} = R_{n,n+1} = g. \quad (8)$$

We will show that $\mu_\alpha < 0$, so that solution (7) tends to zero with time. Let e_n be normed to 1 (the index α will henceforth be omitted). Then (8) in view of (2) yields

$$\mu = \sum_{n=1}^{N} (R_{nn} e_n^2 + R_{n,n-1} e_n e_{n-1} + R_{n,n+1} e_n e_{n+1}) = -2a - g\sum_{n=1}^{N} (e_n - e_{n+1})^2.$$

Therefore, μ_α is larger than or close to $2a$ in magnitude. The quantity $(2a)^{-1}$ determines the characteristic time of dynamic relaxation from an unstable to a stable state of the chain.

Physical considerations clearly suggest that the order parameters behave in the same fashion for each of the chain elements under the steady-state action of the external field. Consequently, a particular solution to (6) is independent of n. It can easily be seen that

$$y_n^{(H)} = \frac{g}{2a}\Delta\sigma_n + \frac{h}{\sqrt{4a^2 + \omega^2}}\cos(\omega t - \varphi) \quad (9)$$

is a particular solution to (6), provided that $\tan(\varphi) = \omega/(2a)$ and $\Delta\sigma_n$ is determined by (5).

Formulas (7) and (9) describe the chain response to a time-dependent external field without taking account of noise action. A steady-state response is

$$x_n = \sigma_n + y_n^{(H)} = \left[z_n + \frac{h}{\sqrt{4a^2+\omega^2}}\cos(\omega t - \varphi)\right]_{\omega \ll 2a} = z_n + \frac{h}{2a}\cos(\omega t) \quad (10)$$

for $t \gg (2a)^{-1}$.

NOISE-DRIVEN RESPONSE

Now consider the response of the chain if both an external field and noise are applied. The latter is modeled by adding a random force $\xi(t)$ to the right-hand side of (3). This force may represent, for example, the action of a thermostat. Specifically, the moments are

$$\langle \xi_n(t) \rangle = 0, \quad \langle \xi_n(t)\xi_m(t') \rangle = 2d\delta_{nm}\delta(t - t'),$$

where d is the noise intensity.

The thus-obtained system of the Langevin equations is equivalent to the kinetic equation

$$\frac{\partial G}{\partial t} = \sum_{n=1}^{N} \frac{\partial}{\partial x_n}\left\{[W'_n - h\cos(\omega t)]G + d\frac{\partial G}{\partial x_n}\right\} \quad (11)$$

for the distribution function $G(x_1, x_2, \ldots, x_N, t)$ subject to the boundary conditions

$$\left(W'_n G + d\frac{\partial G}{\partial x_n}\right)_{x_n \to \pm\infty} = 0. \quad (12)$$

Let us find the average value of the order parameter for the *n*th element:

$$\langle x_n \rangle = \int x_n G dx_1 dx_2 \dots dx_N.$$

As in the noiseless case, the field amplitude is assumed to be small ($h \ll d$), which allows us to seek the distribution function G as a first-order sum in terms of h:

$$G = G^{(0)} + hG^{(1)}. \tag{13}$$

Insert (13) into (11) and equate the terms having the same powers of h. Then,

$$\begin{aligned}\frac{\partial G^{(0)}}{\partial t} &= \sum_{n=1}^{N} \frac{\partial}{\partial x_n}\left(W'_n G^{(0)} + d\frac{\partial G^{(0)}}{\partial x_n}\right),\\ \frac{\partial G^{(1)}}{\partial t} &= \sum_{n=1}^{N} \frac{\partial}{\partial x_n}\left(W'_n G^{(1)} + d\frac{\partial G^{(1)}}{\partial x_n}\right)\\ &\quad - \cos(\omega t)\sum_{n=1}^{N}\frac{G^{(0)}}{\partial x_n}.\end{aligned}$$

The boundary conditions for $G^{(0)}$ and $G^{(1)}$ are similar to (12).

Consider a steady state of the chain under the action of the field. If t is larger than the characteristic relaxation time $t > \tau$, $G^{(0)}$ is virtually an equilibrium function and has the form

$$\begin{aligned}G^{(0)} &= C\exp\left(-\frac{W}{d}\right),\\ C^{-1} &= \int \exp\left(-\frac{W}{d}\right) dx_1 dx_2 \dots dx_N.\end{aligned} \tag{14}$$

The response can be found by solving a steady-state equation for $G^{(1)}$. Due to the boundary conditions, this equation is

$$W'_n G^{(1)} + d\frac{\partial G^{(1)}}{\partial x_n} = \cos(\omega t) G^{(0)}.$$

Let $G^{(1)}$ be expressed as

$$G^{(1)} = \varphi^{(1)}\exp\left(-\frac{W}{d}\right).$$

Then,

$$\varphi^{(1)} = \varphi_0^{(0)} + \frac{C}{d}\cos(\omega t)\sum_{i=1}^{N} x_i.$$

Since (14) is an even function, it makes no contribution to the average value of the order parameter. Consequently,

$$\begin{aligned}\langle x_n \rangle &= \frac{Ch}{d}\cos(\omega t) I_n,\\ I_n &= \sum_{i=1}^{N}\int x_i x_n \exp\left(-\frac{W}{d}\right) dx_1 dx_2 \dots dx_N.\end{aligned} \tag{15}$$

Formula (15) describes a steady-state response to a signal if $\omega \ll \tau^{-1} \ll a$.

The statistical integrals involved in (15) can be calculated by the saddle-point method if ($d \ll a$). First, let us calculate the normalization constant C, appearing in (14). Separate integrations over each x_n yield

$$\begin{aligned}C^{-1} &= C_0^N Z,\\ Z &= \sum_{\sigma_1}\sum_{\sigma_2}\dots\sum_{\sigma_N}\exp[k(\sigma_1\sigma_2 + \sigma_2\sigma_3 + \dots + \sigma_N\sigma_1)],\end{aligned} \tag{16}$$

where

$$C_0 = \left(\frac{\pi}{\lambda}\right)^{1/2}\exp\left(\frac{\lambda}{4}\right),$$

$\lambda = \frac{a}{d}$, $k = \frac{g}{d}$, $\sigma_n = \pm 1$.

The expression for Z is identical to that for the statistical sum in the one-dimensional Ising model for a ferromagnet; therefore, Z can be calculated according to well-known rules (see, e.g., [12]). Specifically,

$$Z = \mathrm{Sp}(P^N), \quad P = \begin{pmatrix} e^k & e^{-k} \\ e^{-k} & e^k \end{pmatrix}.$$

Since the trace of a matrix is invariant under unitary transformations, it is easy to find a transformation S that diagonalizes P:

$$S = \begin{pmatrix} 1 & -1 \\ 1 & 1 \end{pmatrix}, \quad S^{-1} = \frac{1}{2}\begin{pmatrix} 1 & 1 \\ -1 & 1 \end{pmatrix},$$

$$\tilde{P} = S^{-1}PS = \begin{pmatrix} e^k + e^{-k} & 0 \\ 0 & e^k - e^{-k} \end{pmatrix}.$$

Hence

$$Z = \mathrm{Sp}(\tilde{P}^N) = (e^k + e^{-k})^N + (e^k - e^{-k})^N. \tag{17}$$

Now, let us calculate the statistical integral I_n. Separate integrations over each x_n yield

$$I = C_0^N\left(\frac{Z}{2\lambda} + S\right),$$

$$S = \sum_{i=1}^{N}\sum_{\sigma_1}\sum_{\sigma_2}\dots\sum_{\sigma_N}\sigma_i\sigma_N \tag{18}$$

$$\times \exp[k(\sigma_1\sigma_2 + \sigma_2\sigma_3 + \dots + \sigma_N\sigma_1)].$$

The cyclic conditions imply that all of the chain elements are equivalent; therefore, I_n and S_n are independent of n. That is why the subscript n is omitted in (18). Also notice that the first term in the right-hand side of (18) results from the integration over x_n:

$$\int_{-\infty}^{\infty} x_n^2 \exp[-\lambda(x_n - \sigma_n)^2]dx_n = \sigma_n^2 + \frac{1}{2\lambda}.$$

In order to calculate the sum S, consider separately its terms with $i = n$, $i = n \pm 1$, $i = n \pm 2$, etc. The term with $i = n$ is identical to already found Z. The neighboring chain elements are tackled with the obvious equality

$$\sum_{\sigma_1}\sum_{\sigma_2}\dots\sum_{\sigma_N}\sigma_n\sigma_{n\pm 1}\exp[k(\sigma_1\sigma_2 + \dots + \sigma_N\sigma_1)]$$

$$= \frac{1}{N}\frac{\partial Z}{\partial k} = (e^k + e^{-k})^{N-1}(e^k - e^{-k})$$

$$+ (e^k - e^{-k})^{N-1}(e^k + e^{-k}).$$

Straightforward calculation proves the generalization

$$\sum_{\sigma_1}\sum_{\sigma_2}\dots\sum_{\sigma_N}\sigma_n\sigma_{n\pm m}\exp[k(\sigma_1\sigma_2 + \dots + \sigma_N\sigma_1)] \tag{19}$$

$$= (e^k + e^{-k})^{N-m}(e^k - e^{-k})^m + (e^k - e^{-k})^{N-m}(e^k + e^{-k})^m.$$

Notice that (19) coincides with Z in the limiting case $m = N$. This is obvious, since N is the chain period, $\sigma_{n\pm N} = \sigma_n$, and $\sigma_n^2 = 1$. Finally, from (19),

$$S = \sum_{m=0}^{N}\sum_{\sigma_1}\sum_{\sigma_2}\dots\sum_{\sigma_N}\sigma_n\sigma_{n+m}$$

$$\times \exp[k(\sigma_1\sigma_2 + \dots + \sigma_N\sigma_1)] = S_1 + S_2,$$

$$S_1 = \sum_{m=0}^{N-1}(e^k + e^{-k})^{N-m}(e^k - e^{-k})^m = (e^k + e^{-k})^N\frac{1-\alpha^N}{1-\alpha},$$

$$S_2 = \sum_{m=0}^{N-1}(e^k - e^{-k})^{N-m}(e^k + e^{-k})^m = \alpha S_1,$$

where $\alpha = \tanh(k)$.

DISCUSSION

Let the number N of chain elements be very large. Since $\alpha < 1$, the value of α^N is negligible as compared with 1. We thus arrive at the formula for the average noise-driven response to a periodic signal if $\omega \ll \tau^{-1}$:

$$\langle x_n \rangle = \left[\frac{h}{2a} + \frac{h}{d}\exp(2k)\right]\cos(\omega t). \tag{20}$$

At higher frequencies, a non-steady-state equation for $G^{(1)}$ has to be dealt with.

Now, contrast noise-driven response (20) with noiseless response (10). First, it should be pointed out that (20) does not include the time-independent term, which gives the minimum of the potential W. This stems from the fact that noise induces transitions over the potential barriers of the elements, the probability of the transition to the left-hand potential well being exactly equal to that for the right-hand well. With zero noise, the motion is confined to a potential well, as indicated by the time-independent term z_n in (10). Second, it is hardly surprising that both (20) and (10) include the same time-varying (dynamic) term with the coefficient $h/2a$. Third, (20) contains yet another time-varying term: it results from noise–signal interaction. Note that this noise-response term includes an exponential function of the coupling constant g. Although g and d are assumed to be small as against a, the ratio $k = g/d$ may be considerably higher than 1, so that the noise-response term may exceed the noiseless-response term in (20) by an order of magnitude or more. If the elements are uncoupled ($g = 0$), they are statistically independent of each other and formula (20) gives the response of a single bistable element [9].

To sum up, this study has revealed that, under certain conditions, the interaction of bistable elements materially amplifies (due to noise) the response of the chain to a signal. It is therefore reasonable to expect that SR will be more pronounced in an ensemble than in a single element. The additional energy for the response is supplied by the thermostat, which is simulated by the random force $\xi(t)$ in the right-hand side of (3).

Also note that the chain studied is a continuous analog of a one-dimensional Ising model for ferromagnets [12]. This fact explains why the expression for the classical statistical integral turned out to be identical with the quantum statistical sum with an accuracy to the factor. Consequently, it seems very likely that SR will also be observed in ferromagnets.

The augmentation of SR by the interaction of bistable elements occurs, e.g., in radiophysical devices. Consider an element comprising a tunnel diode connected in parallel to a capacitance C and in series to a resistance R. The element has also a voltage source generating a harmonic signal, a dc component, and noise. Such element is known to be bistable [4]. Its order parameter is $U - U_0$, where U is the voltage across C and U_0 is the middle point in the negative-resistance portion of the diode characteristic. The magnitude $|R_T|$ of the negative resistance is ~1 kΩ. For the potential U of the element, it has been found that $a = 10^6$ s^{-1} and $b = 3 \times 10^6$ s^{-1} V^{-2} if $C \sim 1$ nF. Interaction between the elements is implemented by connecting them in series. Then, the coupling constant $g = (RC)^{-1}$. It can be shown that a and b tend to certain limits as R increases. Therefore, the necessary (theoretical) condition $g \ll a$ is met if $R \gg |R_T|$. Also, the frequency ω of the harmonic signal must be much smaller than a.

ACKNOWLEDGMENTS

This work was supported by the Russian Foundation for Basic Research, project no. 96-02-18692.

REFERENCES

1. R. Benzi, S. Sutera, and A. Vulpiani, J. Phys. A **14**, L453 (1981).
2. B. McNamara, K. Wiesenfeld, and R. Roy, Phys. Rev. Lett. **60**, 2626 (1988).
3. M. I. Dykman, A. L. Velikovich, G. P. Golubev, *et al.*, Pis'ma Zh. Éksp. Teor. Fiz. **53** (4), 182 (1991).
4. R. N. Mantegna and B. Spagnolo, Phys. Rev. E **49**, R1792 (1994).
5. M. E. Inchiosa, A. R. Bulsara, A. D. Hibbs, *et al.*, Phys. Rev. Lett. **80**, 1381 (1998).
6. M. I. Dykman, T. Horita, and J. Ross, J. Chem. Phys. **103**, 966 (1995).
7. D. R. Chialvo, A. Longtin, and J. Müller-Gerking, Phys. Rev. E **55**, 1798 (1997).
8. L. Gammaitoni, P. Hänggi, P. Jung, *et al.*, Rev. Mod. Phys. **70**, 223 (1998).
9. S. A. Reshetnyak and L. A. Shelepin, *Quasi-stationary Distributions in Kinetics* (IPO Avtor, Moscow, 1996).
10. S. A. Reshetnyak, J. Russ. Laser Research **19**, 175 (1998).
11. M. E. Inchiosa and A. R. Bulsara, Phys. Lett. A **200**, 283 (1995).
12. Yu. B. Rumer and M. Sh. Ryvkin, *Thermodynamics, Statistical Physics, and Kinetics* (Nauka, Moscow, 1997).

Translated by A. A. Sharshakov

Technical Physics, Vol. 45, No. 3, 2000, pp. 290–293. Translated from Zhurnal Tekhnicheskoĭ Fiziki, Vol. 70, No. 3, 2000, pp. 6–8.
Original Russian Text Copyright © 2000 by Libenson, Shiryaev.

THEORETICAL AND MATHEMATICAL PHYSICS

Allowance for Effects Due to Thermoelectrically Induced Vortex Motion in an Analysis of Structure Formation on Melt Surfaces

M. N. Libenson and V. A. Shiryaev
Vavilov State Optical Institute, Birzhevaya liniya 12, St. Petersburg, 199034 Russia

Received November 24, 1998

Abstract—A model of thermoelectrically induced formation of surface periodic structures allowing for vortex motion of the melt is proposed. An analytical solution for surface profile dynamics involving two-dimensional transport is obtained. It is shown that structure formation can occur only when the melt viscosity is sufficiently low. © *2000 MAIK "Nauka/Interperiodica".*

Laser light incident on condensed media frequently induces the formation of coherent surface profiles, which are generally preserved after the exposure to laser action. According to [1, 2], the formation of a surface periodic structure (SPS) includes the following stages.

The incident plane wave is diffracted by the nonuniformities of a real surface. When the wave vectors of the diffracted light and the surface electromagnetic wave (SEW) are equal, the latter is amplified through a resonance mechanism. The interference of the incident light with the SEW gives rise to a spatially periodic heat source in the surface layer. The spatially nonuniform heating of the material leads to surface profile formation involving various phenomena (oxidation, melting, evaporation, etc.), closing up a feedback loop.

Despite two decades of intensive studies of the conditions that lead to SPS formation, current understanding of profile formation scenarios is far from complete. We continue the systematic analysis of the effect of electric-field pressure on a melt started in [3, 4]. This effect is associated, in particular, with the thermal emf induced by nonuniform laser heating of a surface. The action of a laser pulse on a material surface generally changes the state of the surface layer. In this paper, we analyze the formation of structure on the surface of a thin film of a semiconductor melt that has transformed into metal. Here, a key factor is the small thickness of the conducting film. In the case of bulk metal, one should take into account the shunting effect of deep-lying layers, which substantially reduces the contribution of thermal emf to SPS formation.

Thermoelectrically induced structure formation was previously analyzed only in the one-dimensional case [4]. However, since the thermoelectrical pressure field is essentially solenoidal, a self-consistent model must include the Navier–Stokes equations supplemented with appropriate boundary conditions.

Consider a semiconductor that occupies the half-space

$$z > \xi(x, t)$$

and is exposed to laser light (see Fig. 1).

The metal melt layer formed by heating is bounded by the surfaces

$$z = \xi(x, t) \quad \text{and} \quad z = H_0.$$

Assuming that the surface disturbance height ξ is much smaller than the spatial period of the incident light, we restrict our analysis to the surface harmonic that is resonant with the surface electromagnetic wave [1, 2]. Then,

$$\xi(x, t) = h_c(t)\cos gx + h_s(t)\sin gx,$$

$$\xi(x, 0) = h_0 \cos gx.$$

The mathematical model is constructed so as to allow for slower variation of the average temperature T_1 as compared to the harmonic component T_2, where

$$T_1 \gg T_2. \tag{1}$$

The total temperature is expressed as

$$T(x, z, t) = T_0 + T_1(z, t) + T_2(x, z, t), \tag{2}$$

$$T_2(x, z, t) = \theta_c(z, t)\cos gx + \theta_s(z, t)\sin gx, \tag{3}$$

where T_0 is the ambient temperature (see Fig. 2).

The heat equations for T_1 and T_2 are written as follows:

$$\frac{\partial T_1}{\partial t} = a\frac{\partial^2 T_1}{\partial z^2} + \frac{g\alpha}{c\rho}e^{-\alpha z}, \tag{4}$$

$$\frac{\partial T_2}{\partial t} = a\frac{\partial^2 T_2}{\partial z^2} - ag^2 T_2$$

$$+ 2\mu\frac{g\alpha}{c\rho}e^{-\alpha z}\{h_c\cos(gx+\varphi) + h_s\sin(gx+\varphi)\} \quad (5)$$

$$- v_z\frac{\partial T_1}{\partial z}[\mathcal{H}(z) - \mathcal{H}(z-H_0)].$$

They should be supplemented by the initial and boundary conditions

$$\left.\frac{\partial T_1}{\partial z}\right|_{z=0} = \left.\frac{\partial T_2}{\partial z}\right|_{z=0} = 0, \quad (6)$$

$$T_1(x, z, t=0) = T_2(x, z, t=0) = 0, \quad (7)$$

$$T_1(x, z=\infty, t) = T_2(x, z=\infty, t) = 0. \quad (8)$$

The thermoelectrically induced electric field $\mathbf{E}$ is related to temperature as follows:

$$\mathbf{E} = \gamma(T)\,\mathrm{grad}\,T, \quad (9)$$

$$\gamma(T) = \Omega T. \quad (10)$$

Here, Ω is a constant factor. Fluid dynamics are described by the Navier–Stokes and continuity equations (for incompressible flows):

$$\frac{\partial \mathbf{v}}{\partial t} = \nu\nabla\mathbf{v} - \frac{\nabla p}{\rho} + \frac{\mathbf{E}\,\widetilde{\mathrm{div}}\,\mathbf{E}}{4\pi\rho}, \quad (11)$$

$$\mathrm{div}\,\mathbf{v} = 0. \quad (12)$$

The Navier–Stokes equations are used in linearized form in (11) because the amplitude of hydrodynamic waves is small. The velocity $\mathbf{v}$ is expressed in terms of scalar and vector potentials as

$$\mathbf{v} = \mathrm{grad}\,\Psi + \mathrm{rot}\,\mathbf{A}, \quad (13)$$

$$v_x = \frac{\partial\Psi}{\partial x} - \frac{\partial A}{\partial z}, \quad v_z = \frac{\partial\Psi}{\partial z} - \frac{\partial A}{\partial x}. \quad (14)$$

The boundary conditions on the free surface $z = 0$ are written as

$$\frac{\partial\xi}{\partial t} = v_z, \quad (15)$$

$$\frac{\partial\Psi}{\partial t} = \frac{\sigma}{\rho}\frac{\partial^2\xi}{\partial x^2} - 2\nu\frac{\partial v_z}{\partial z}, \quad (16)$$

$$\frac{\partial v_x}{\partial z} + \frac{\partial v_z}{\partial x} = 0. \quad (17)$$

On the solid-state phase boundary, we have

$$v_x = 0, \quad (18)$$

$$v_z = 0. \quad (19)$$

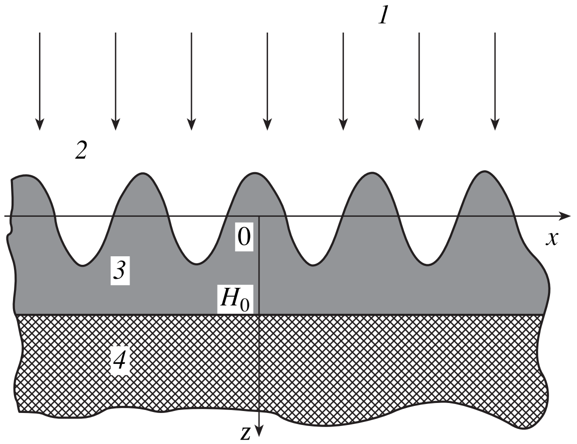

Fig. 1. Schematic of the problem: (*1*) laser light; (*2*) air; (*3*) metal (semiconductor melt); and (*4*) semiconductor.

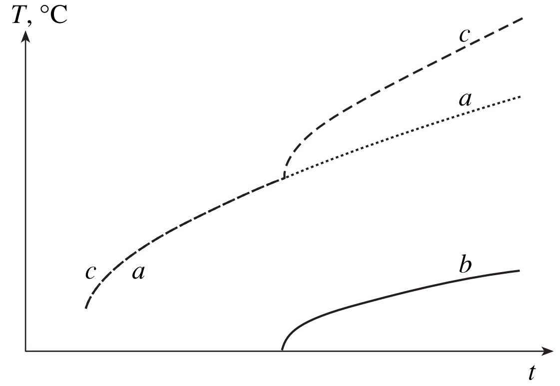

Fig. 2. Typical curves of temperature and its components as functions of heating time *t*: (*a*) average temperature T_1, (*b*) amplitude of the cosine component θ_c, and (*c*) total surface temperature $T_1 + \theta_c$.

Since we seek harmonic components, we can write

$$\Psi = \Psi_c(z, t)\cos gx + \Psi_s(z, t)\sin gx, \quad (20)$$

$$A = A_c(z, t)\cos gx + A_s(z, t)\sin gx. \quad (21)$$

In equations (1)–(21), g is the spatial frequency, a is the thermal diffusivity of the melt, q is the absorbed radiant flux, α is the absorption coefficient, c is heat capacity, ρ is density, μ is the efficiency of light conversion into a SEW, φ is the phase shift of the heat source with respect to the surface harmonic, $\mathcal{H}$ is the Heaviside step function, ~ denotes a harmonic component, γ is the coefficient of thermal emf, $\mathbf{E}$ is the strength of the thermally induced electric field, Ψ is the scalar velocity potential, $\mathbf{A}$ is the vector velocity potential, ν is viscosity, p is pressure, and σ is surface tension. Equations (1)–(21) are solved as follows. First, the average temperature $T_1(z, t)$ is found. The result is substituted into the heat equation for $T_2(x, z, t)$ and the Navier–Stokes equations (11) in the limit $T_1 \longrightarrow \infty$. In particular, the following expression is used:

$$\frac{\partial T_1}{\partial z}(z, \infty) = \frac{q}{\lambda}(e^{-\alpha z} - 1), \tag{22}$$

where λ is the heat conductivity.

The harmonic component of the product $\mathbf{E}\,\mathrm{div}\mathbf{E}$ in the Navier–Stokes equations is then determined. The convective term in the heat equation is assumed to be much smaller than the light-to-SEW conversion term and is dropped. This assumption is validated in the analysis below.

Next, the Laplace transform with respect to the time variable ($t \longrightarrow w$) is performed in all equations. Then, $\theta_c(z, w)$ and $\theta_s(z, w)$ are calculated as functions of $h_c(w)$ and $h_s(w)$, and the results are substituted into the Navier–Stokes equations. Let us consider the cases of low and high viscosity.

Since we seek a solution describing an exponentially growing surface disturbance, velocity must also be an exponentially growing function. Therefore, we can neglect the effect of friction on fluid dynamics and consider the time-dependent problem, i.e.,

$$\left|\frac{\partial \mathbf{v}}{\partial t}\right| \gg \nu|\Delta\mathbf{v}|. \tag{23}$$

Applying the operator rot to both sides of the Navier–Stokes equation, we eliminate the term

$$\left(\boldsymbol{\nabla} \times \frac{\boldsymbol{\nabla} p}{\rho}\right).$$

The resulting equation can be solved. Since we seek $h_c(w)$ and $h_s(w)$ only, we use boundary conditions (15) and (17). The desired result is

$$h_c(t) = \Re h(t), \quad h_s(t) = \Im h(t), \tag{24}$$

$$\beta = \frac{\gamma}{4\pi\rho}\frac{q^2}{\lambda}\frac{\alpha^2}{c\rho}\frac{2\mu}{g}, \tag{25}$$

$$h(t) = h_0\exp(-ag^2t)\sum_{k=1}^{7} f_1(w_k)/f_2(w_k), \tag{26}$$

$$f_1(w_k) = w_k^2(w_k^2 - \alpha^2)\exp(w_k^2 t)\operatorname{erfc}(-w_k\sqrt{t}), \tag{27}$$

$$f_2(w_k) = \frac{\partial}{\partial w}\Bigg(2w(w^2 - a\alpha^2)(w - ag^2)^2 - \beta\left[\sqrt{a}\gamma\left(\frac{w}{\sqrt{a}} + \gamma\right)^2 - 4\frac{\partial\gamma}{\partial T}\frac{q}{\lambda}w + \gamma\sqrt{a}\alpha\right] \times \exp(-i\varphi)\Bigg)\Bigg|_{w = w_k}, \tag{28}$$

$$w_{1-5} = \left(\frac{\beta\gamma}{2\sqrt{a}}\right)^{1/5} e^{-i\frac{\varphi + 2\pi n}{5}}, \quad n = 0, 1, 2, 3, 4, \tag{29}$$

$$w_{6,7} = \sqrt{a}\left(\frac{2}{\gamma}\frac{\partial\gamma}{\partial T}\frac{q}{\lambda} - \alpha\right) \pm \sqrt{4\frac{a}{\gamma^2}\left(\frac{\partial\gamma}{\partial T}\right)^2\frac{q^2}{\lambda^2} - a\alpha^2 - 2\frac{a\alpha}{\gamma}\frac{\partial\gamma}{\partial T}\frac{q}{\lambda}}. \tag{30}$$

Here, the numerous increments and decrements reflect the chosen form of the heat source and the fact that the solution for surface profile dynamics in the low-viscosity approximation is determined by a thermoelectrically induced solenoidal pressure source. It is understood that the velocity field, which is not sought here, would depend on the entire set of boundary conditions.

An analysis of the expressions obtained shows that at least one of the roots w_{1-7} ensures exponential growth of a surface disturbance irrespective of the electrodynamic delay φ, because the solution describes the case of a strong inducing field.

To check the validity of the assumptions made above, we set $\alpha = 10^5$ cm^{-1}, $g = 10^4$ cm^{-1}, $q = 10^{12}$ erg cm^{-2} s^{-1}, $\lambda = 10^7$ erg(s cm^2 K)$^{-1}$, $\rho = 5$ g cm^{-3}, $\mu = 10^7$ cm^{-1}, $H_0 = 10^{-5}$ cm, $a = 10^{-2}$ cm^2 s^{-1}, $\gamma = 10^{-4}$ V K^{-1}, $\partial\gamma/\partial t = 10^{-8}$ V K^{-2}, and $\nu = 5 \times 10^{-4}$ cm^2 s^{-1}. In addition, we can assume that

$$|\Delta\mathbf{v}| \sim g^2|\mathbf{v}|, \tag{31}$$

$$|\mathbf{v}| \sim \left|\frac{\partial\xi}{\partial t}\right|, \tag{32}$$

$$\left|\frac{\partial\xi}{\partial t}\right| \sim \left|w_k^2\xi\right|. \tag{33}$$

Using these realistic numerical values of the parameters and estimates (31)–(33), one can show that the low-viscosity approximation is valid and the convective terms can be neglected. In the quasi-steady case of high viscosity,

$$\nu|\Delta\mathbf{v}| \gg \left|\frac{\partial\mathbf{v}}{\partial t}\right|, \tag{34}$$

the solution is not expected to contain any exponentially growing surface disturbance or velocity. This conjecture is confirmed by straightforward calculations.

The solution obtained suggests that surface profile dynamics are completely determined by the solenoidal electric field in the bulk of the melt. Indeed, when an additional electric field (say, generated by thermal electron emission) is considered on the melt surface, it is taken into account only in boundary condition (16), which is not used in calculating h_c and h_s. However, the velocity field depends on surface charge as well.

ACKNOWLEDGMENTS

This work was supported by the Russian Foundation for Basic Research, project no. 96-02-18783. We thank E. D. Éĭdel'man for helpful discussions of the hydrodynamic facets of the problem analyzed here.

REFERENCES

1. A. M. Bonch-Bruevich and M. N. Libenson, in *Nonlinear Electromagnetic Surface Phenomena*, Ed. by H.-E. Ponath and G. I. Stegeman (Elsevier, Amsterdam, 1991), Chap. 10, pp. 561–609.
2. S. A. Akhmanov, V. I. Emel'yanov, N. I. Koroteyev, and V. N. Seminogov, Usp. Fiz. Nauk **147**, 675 (1985).
3. I. A. Dorofeev and M. N. Libenson, Zh. Tekh. Fiz. **65**, 111 (1995).
4. I. A. Dorofeev, M. N. Libenson, and V. A. Shiryaev, Izv. Ross. Akad. Nauk, Ser. Fiz. **61**, 1269 (1997).

Translated by A. S. Betev

Technical Physics, Vol. 45, No. 3, 2000, pp. 294–297. Translated from Zhurnal Tekhnicheskoĭ Fiziki, Vol. 70, No. 3, 2000, pp. 9–12.
Original Russian Text Copyright © 2000 by Voĭtkiv, Voĭtsekhovskiĭ, Grün, Scheĭde.

ATOMS, SPECTRA, AND RADIATION

Ionization of Hydrogen Atom Induced by Relativistic Particles Collisions Accompanied by Low Momentum Transfer

A. V. Voĭtkiv*, I. A. Voĭtsekhovskiĭ*, N. Grün, and V. Scheĭde****
** Arikhov Institute of Electronics, Tashkent, 700143 Uzbekistan*
*** Institut für Theoretische Physik, Hessen Universität, Germany*

Received April 13, 1998; in final form, April 15, 1999

Abstract—Ionization of a hydrogen atom in soft collisions with a relativistic charged particle is considered for the cases (a) $Z \sim v$, $v_0 \ll v < c$ and (b) $Z \ll v$, $v_0 \ll v < c$. Here, Z and v are, respectively, the charge and velocity of the incident particle, v_0 is the typical electron velocity in the ground state of the hydrogen atom, and c is the velocity of light. Analytical expressions for the differential cross sections for the ionization of hydrogen atom are analyzed. The asymmetry in the angular distribution of the emitted electrons is shown to result from the following two effects: the atomic absorption of virtual quanta of the field related to relativistic particle and the final-state interaction. © *2000 MAIK "Nauka/Interperiodica".*

Ionization of atoms in collisions with fast charged particles ($v \gg v_0$, where v is the velocity of the incident particle and v_0 is the typical electron velocity in the atom) is a fundamental physical problem. It is well known that collisions accompanied by low momentum transfer to atomic electrons (soft collisions) make dominant contribution to the cross section for the single ionization of an atom by a fast charged particle. In such collisions, the electron velocity v_e (in the rest frame of the target atom) in the final state of the continuous spectrum only slightly exceeds the typical velocity v_0 of electrons in the initial bound state, i.e., $v_e \lesssim v_0$. Simple estimations demonstrate (see also below) that the relative contribution of soft collisions to the cross section must increase considerably as an atom is being ionized by relativistic and, especially, by ultrarelativistic charged particles.

The ionization of hydrogen atoms in collision with nonrelativistic highly charged ions (HCIs) was studied in [1], where analytical formulas for the cross section for the ionization accompanied by the emission of slow electrons were derived in the *S*-matrix formalism. In this study, we extend the results obtained in [1] to the case of relativistic collision velocities. Omitting the details of calculation in this brief paper (the calculation for nonrelativistic collisions was described in detail in [1]), we represent the final expression for the double differential (with respect to the emission angle and to the electron energy $E = k^2/2$) cross section for ionization in the form[1]

$$\frac{d^2\sigma}{dE\,d\Omega} = 2^8\frac{Z^2}{v^2}\frac{1}{(1+2E)^5}\frac{\exp\left(-\frac{4\arctan\sqrt{2E}}{\sqrt{2E}}\right)}{\left[1-\exp\left(-\frac{2\pi}{\sqrt{2E}}\right)\right]}$$

$$\times\left\{\sin^2\Theta\ln\eta - 0.5\sin^2\Theta + \gamma^{-2}\cos^2\Theta + \frac{8\sqrt{2E}}{v}\cos\Theta\left[\left(1-\frac{v^2}{2c^2}\right)\sin^2\Theta(\ln\eta - 0.5) + 0.25\gamma^{-2}(3\cos^2\Theta - 1)\right] + \frac{2Z}{v^2\gamma^2}\cos\Theta \times\left\{\ln^2\eta + 2^{1.5}\pi E^{1/2}\left[\sin^2\Theta\ln\eta + \cos 2\Theta - 0.5\sin^2\Theta + \frac{v^2}{c^2}\left(\frac{1}{4} - \cos^2\Theta\right)\right]\right\}\right\}. \tag{1}$$

Here, $\gamma = 1/\sqrt{1-(v/c)^2}$, Θ $(0 \le \Theta \le \pi)$ is the angle between the electron momentum $\mathbf{k}$ and the particle velocity $\mathbf{v}$, $d\Omega = 2\pi\sin\Theta d\Theta$, and

$$\eta = \frac{1.123\,v\gamma}{b_{\min}(E+0.5)} = 1.123\frac{v^2\gamma}{Z}\frac{1}{E+0.5},$$

where $b_{\min}$ is the lower limit of the region of impact parameters under consideration.

Expression (1) has a clear physical meaning. The term proportional to Z^2/v^2 reflects the atom ionization owing to electric dipole transitions in the first order of the perturbation theory. This term of the cross section can be obtained by using the Weizäcker–Williams method, which treats the interaction of a relativistic particle with an atom as the absorption of a virtual quantum, which has some energy but does not transfer any momentum, by an atomic electron (see, for exam-

---

[1] We use atomic units.

1063-7842/00/4503-0294$20.00 © 2000 MAIK "Nauka/Interperiodica"

ple, [2]). The second term proportional to Z^2/v^3 appears in the case when the momentum of the virtual photon is taken into account. The third term proportional to $Z^3/(v^4\gamma^2)$ corresponds to the final-state interaction. Under the replacement $\Theta \longrightarrow \pi \longrightarrow \Theta$, the dipole part does not change, whereas the second and the third terms reverse their signs and, therefore, describe the asymmetry in the angular distribution of slow electrons. As follows from expression (1), ultrarelativistic collisions lead to weak asymmetry that is primarily related to the absorption of the momentum of a virtual photon. In the approximation under consideration, both terms in (1) providing the angular asymmetry do not make a contribution to the energy differential cross section and to the total cross section for the ionization.

Energy distribution of slow electrons is proportional to the differential cross section for ionization as

$$\frac{d\sigma}{dE} = \int d\Omega \frac{d^2\sigma}{dE\,d\Omega}$$

$$= \frac{2^{11}\pi Z^2}{3}\frac{1}{v^2(1+2E)^5}\frac{\exp\left(-\frac{4\arctan\sqrt{2E}}{\sqrt{2E}}\right)}{\left[1-\exp\left(-\frac{2\pi}{\sqrt{2E}}\right)\right]} \tag{2}$$

$$\times\left\{\ln\left[\frac{2.25v^2\gamma}{Z(1+2E)}\right]-\frac{v^2}{2c^2}\right\}.$$

As follows from expression (2), the probability of ionization decreases rapidly with the energy of the emitted electron and the majority of electrons have energy that only slightly exceeds the value of $E_0 = 0.5$.

To derive the angular distribution of slow electrons, it is necessary to integrate cross section (1) over the electron energies. Since the probability of electron emission decreases rapidly with the energy E, the upper integration limit can be taken to be infinity. We then find

$$\frac{d\sigma}{d\Omega} = \int_0^\infty dE\frac{d^2\sigma}{dE\,d\Omega} = 3\times 0.283\times\frac{Z^2}{v^2}$$

$$\times\left\{\sin^2\Theta\ln\eta_1 - 0.5\sin^2\Theta + \gamma^{-2}\cos^2\Theta\right.$$

$$+\frac{8\times 0.61}{v}\cos\Theta\left[\left(1-\frac{v^2}{2c^2}\right)\sin^2\Theta(\ln\eta_2 - 0.5)\right.$$

$$\left.+0.25\gamma^{-2}(3\cos^2\Theta - 1)\right] + \frac{2Z}{v^2\gamma^2}\cos\Theta \tag{3}$$

$$\times\left[\ln^2\eta_1 + 2\pi 0.61\left(\sin^2\Theta\ln\eta_2 + \cos 2\Theta\right.\right.$$

$$\left.\left.\left.-0.5\sin^2\Theta + \frac{v^2}{c^2}\left(\frac{1}{4}-\cos^2\Theta\right)\right)\right)\right]\right\},$$

where

$$\eta_{1,2} = \frac{1.12v^2\gamma}{Z\omega_{1,2}},\quad \omega_1 = \exp\left(\frac{\int_0^\infty dk k^2\alpha(k)\ln\omega}{\int_0^\infty dk k^2\alpha(k)}\right) = 0.71,$$

$$\omega_2 = \exp\left(\frac{\int_0^\infty dk k^3\alpha(k)\ln\omega}{\int_0^\infty dk k^3\alpha(k)}\right) = 0.88,\quad \omega = \frac{1+k^2}{2}. \tag{4}$$

As far as we know, there are no experimental data on the ionization of hydrogen atoms in soft collisions with fast high-charged ions. Figures 1 and 2 show, respectively, the double differential and differential, with respect to the angle of electron emission, cross sections calculated in our approach as compared to those calculated in the first Born approximation. As seen from these figures, there are two basic differences between the results of calculations in these approximations. First, the cross section values calculated in the first Born approximation are, in general, considerably larger than the results calculated by formulas (1) and (3). Second, calculation by expressions (1) and (3) predicts more pronounced angular asymmetry in the spectra of slow electrons than follows from the calculation in the first Born approximation. Both these differences tend to increase with increasing charge of HCIs under fixed collision velocity. These differences are caused by the following reasons. First, it is well known that the probability of the ionization calculated in the first Born approximation becomes large at small impact parameters and can even exceed unity at large charge values of the incident particle because this approximation is not unitary. In our approach, this problem is solved by properly choosing the parameter $b_{\min}$ [3]. Second, our approach, in contrast to the first Born approximation, takes into account the final-state interaction, which results in an additional assymetry in the angular distribution of emited electrons. With an increase of the incident particle energy per amu, the contribution from that region of impact parameter increases, where the probability of the ionization is small and, therefore, the first Born approximation is applicable [4]. In addition, the contribution of the final-state interaction decreases in this case. For this reason, the difference between results calculated in our approach and in the first Born approximation decreases with increasing energy of the incident particle under a fixed value of their charge.

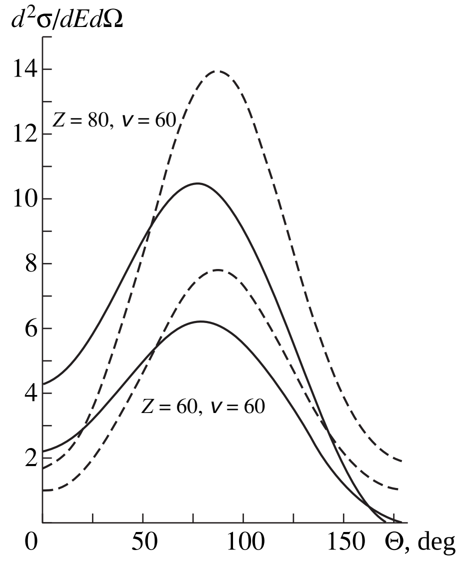

Fig. 1. Doubly differential cross section for the ionization calculated by formula (1) (solid lines) and in the first Born approximation (dashed lines) as functions of the angle of electron emission at the energy $E = 0.18$ (5 eV).

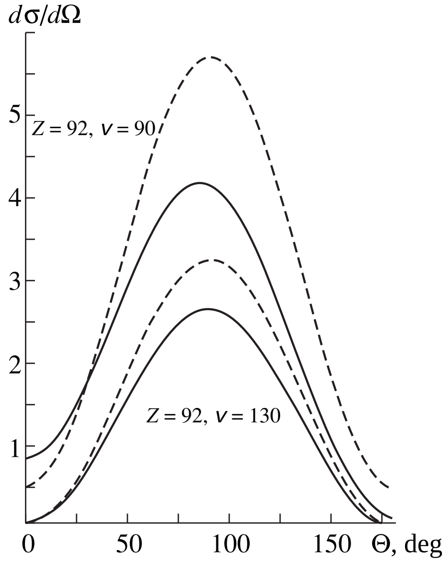

Fig. 2. Angular differential cross section for ionization calculated by formula (3) (solid lines) and in the first Born approximation (dashed lines).

The angular asymmetry in the electron emission can be specified by the asymmetry parameter

$$\Gamma = \frac{\left(\int\limits_0^{\pi/2} d\Theta \sin\Theta \frac{d\sigma}{d\Omega} - \int\limits_{\pi/2}^{\pi} d\Theta \sin\Theta \frac{d\sigma}{d\Omega}\right)}{\int\limits_0^{\pi} d\Theta \sin\Theta \frac{d\sigma}{d\Omega}}. \qquad (5)$$

It follows from expressions (3)–(5) that

$$\Gamma \simeq \frac{1.83}{v} + \frac{1.5Z}{v^2\gamma^2}\ln\left(\frac{1.6v^2\gamma}{Z}\right). \qquad (6)$$

The angular asymmetry in the spectra of electrons emitted in the collisions with fast charged particles was discussed recently in depth (see, for example, [5, 6]). This asymmetry is treated, as a rule, only as a result of the final-state interaction when electrons emitted from the atom are attracted by a fast charged particle. If the final-state interaction were always the main reason for angular asymmetry in the fast collisions, it would be expected that the "sign" of this asymmetry must be reversed in the case when the incident particle charge is negative. Actually, according to the classical-trajectory Monte Carlo calculations [5], it would be expected that electrons must predominantly be emitted in directions opposite to the velocity of the incident fast negative HCIs. Unfortunately, these predictions cannot be verified experimentally. However, we note that such predictions are in contradiction to experimental data on the helium ionization by fast antiprotons, where weak "positive" angular asymmetry is observed—that is, the majority of electrons were emitted in the direction of the fast particle motion [7].

Expression (4) yields the contribution $\Delta\sigma_i$ of soft collisions to the total cross section for the ionization of hydrogen atom in the form

$$\Delta\sigma_i = 8\pi 0.283\frac{Z^2}{v^2}\left[\ln\left(\frac{1.6v^2\gamma}{Z}\right) - \frac{v^2}{2c^2}\right]. \qquad (7)$$

Only the numerical factor in the logarithm argument distinguishes this expression from the following expression for the total cross section σ_i obtained in [4] for collision parameters satisfying the conditions $v \sim Z \ll v^2\gamma$, $1 \ll v < c$:

$$\sigma_i = 8\pi 0.283\frac{Z^2}{v^2}\left[\ln\left(\frac{5v^2\gamma}{Z}\right) - \frac{v^2}{2c^2}\right]. \qquad (8)$$

The relation $\Delta\sigma_i \sim \sigma_i$ takes place for nonrelativistic collisions, i.e., the collisions accompanied by the emission of slow electrons almost completely determine the value of the total cross section for ionization.

It should be noted that the obtained energy distribution and total cross section coincide, under neglect of nondipole corrections and the final-state interaction, with the respective results obtained in the well-known Weizäcker–Williams approximation of equivalent photons.

Expressions (1)–(3) and (7) describe three basic relativistic effects in an explicit form. In the limit $\gamma \gg 1$, with increasing γ, the number of emitted slow electrons increases as $\ln\gamma$, the effect of the final-state interaction decreases as γ^{-2}, and the emission of electrons increases along the direction $\Theta \simeq \pi/2$ transverse to the beam velocity and decreases along the directions $\Theta = 0$ and $\Theta = \pi$.

Expressions for the cross sections obtained above can be employed also to the hypothetical case of collisions with fast anti-HCIs, when the charge Z is negative but large in magnitude, and to the case of collisions with ions having comparatively small charge values when $|Z| \ll v$. To describe the collisions with fast anti-HCIs, only the replacement $Z \longrightarrow |Z|$ is needed in the logarithm argument in expressions (1)–(3), (6)–(8). To estimate the cross sections in the collisions at $|Z| \ll v$, it is necessary to put $b_{\min} = 1$ in these expressions.

The qualitative effects discussed above for the ionization of hydrogen atoms must obviously occur also for the ionization in the soft collisions with other light atomic targets, enabling us to predict some general properties of the angular asymmetry in the single ionization. According to the above analysis, the angular asymmetry is described by two terms proportional to Z^2/v^3 and $Z^2/(v^4\gamma^2)$ in the expressions for the cross sections. Therefore, in the relativistic (ultrarelativistic) collisions when $|Z|/v\gamma^2 \ll 1$ and also in fast collisions with particles having a relatively small charge value ($|Z| \ll v$), slow electrons must be predominantly emitted in the direction of the motion of the fast particle independently of its charge sign because the asymmetry, in this case, is primarily related to the effect of the absorption of a virtual photon whose value and direction are independent of the value and sign of the fast particle charge. This fundamental conclusion agrees with experimental data [7] on the ionization of helium by fast antiprotons ($Z = -1$, $v = 6.35$) for which $|Z|/v \ll 1$.

In conclusion, we note that the approach applied here to the analysis of the ionization of hydrogen atoms in soft collisions with relativistic charged particles is actually asymptotic and provides logarithmic accuracy. This accuracy increases with increasing dimensions of the region of impact parameters $|Z|/v < b < \gamma v$ (for $|Z| \sim v$) and $1 < b < \gamma v$ (for $|Z| \ll v$). The approach proposed allows one to obtain analytical expressions for the ionization cross sections of hydrogen atoms and provides qualitative interpretation of basic physical effects in the single ionization of light atomic targets in soft collisions with fast charged particles.

REFERENCES

1. A. B. Voĭtkiv, Zh. Tekh. Fiz. **67** (7), 13 (1997) [Tech. Phys. **42**, 728 (1997)].
2. J. D. Jackson, *Classical Electrodynamics* (Wiley, New York, 1975).
3. A. B. Voĭtkiv and A. V. Koval’, J. Phys. B: At. Mol. Opt. Phys. **31**, 499 (1998).
4. A. B. Voĭtkiv, J. Phys. B: At. Mol. Opt. Phys. **29**, 5433 (1996).
5. R. Moshammer, J. Ullrich, M. Unverzagt, *et al.*, Phys. Rev. Lett. **73**, 3371 (1994).
6. R. Moshammer, J. Ullrich, H. Kollmus, *et al.*, Phys. Rev. A: Gen. Phys. **56**, 1351 (1997).
7. Kh. Khayyat, M. Ashler, T. Weber, *et al.*, in *Book of Abstracts of ICPEAC 97, 1997*, Vol. 1, p. L73.

Translated by R. Tyapaev

Technical Physics, Vol. 45, No. 3, 2000, pp. 298–303. Translated from Zhurnal Tekhnicheskoĭ Fiziki, Vol. 70, No. 3, 2000, pp. 13–18.
Original Russian Text Copyright © 2000 by Vol'pyas, Gol'man.

GASES AND FLUIDS

Quasihard-Sphere Model in Simulation of the Processes of Particle Scattering

V. A. Vol'pyas and E. K. Gol'man
St. Petersburg State University of Electrical Engineering, St. Petersburg, 197376 Russia

Received October 12, 1998

Abstract—A model of interatomic potentials of interaction is suggested for static simulation of the processes of elastic scattering of atomic particles by atoms of gas, plasma, and solid. In the developed model, the atomic particle radii, whose magnitude depends on the energy of their relative motion, are internal parameters. The suggested quasihard-sphere model enables one to simulate elastic processes of scattering of atomic particles, using different interatomic potentials of interaction with relatively high rates of statistical simulation characteristic of simulation within the hard-sphere model. The Born–Mayer potential is selected as the interatomic potential of interaction and modified for a wide class of partners in atomic collisions. It is demonstrated that the suggested mathematical model of quasihard spheres describes fairly correctly the processes of elastic scattering of atoms in a gas medium and of displaced atoms in a solid with an almost constant rate of static simulation. © *2000 MAIK "Nauka/Interperiodica".*

INTRODUCTION

In order to perform numerical simulation of the processes of interaction of atomic particles in a gas and in a solid by the Monte Carlo method, one must determine a number of basic stochastic variables which describe adequately the processes of particle scattering. In describing the processes of elastic interaction of atomic particles, the main characteristic is provided by the scattering angle which defines the energy loss and the subsequent behavior of their motion. The scattering angle relates to each other the impact parameter b, the interatomic potential of interaction $U(r)$, and the energy of relative motion of particles E_c. Given a spherically symmetric potential of interaction, the scattering angle Θ in a center-of-mass-system is described by the expression [1]

$$\Theta = \pi - 2b\int\limits_{r_{\min}}^{\infty}\frac{dr/r^2}{[1 - U(r)/E_c - b^2/r^2]^{1/2}}, \qquad (1)$$

where r is the interatomic distance; E_c is the kinetic energy of relative motion of atomic particles in the center-of-mass system for $r \longrightarrow \infty$; and $r_{\min}$ is the shortest distance within which the particles come closer together, which is the root of the radicand in the denominator.

Expression (1) in the analytical form may be integrated only for the hard-sphere potential and for a number of power potentials and their linear combinations. In describing the processes of elastic scattering of atomic particles for more real interatomic potentials of interaction, one restricts oneself to the use of various approximate methods within both classical and quantum-mechanical description [2, 3].

The complexity of the computational procedure during numerical simulation of the processes of particle scattering by the Monte Carlo method is largely defined by the choice of the interatomic potential of interaction. In so doing, one must make a sound compromise between the real physical description of the interaction processes and relative simplicity of the computational procedure during their mathematical simulation. The use of the interatomic potential of hard spheres results in a significant simplification of the calculation procedure, first of all, during statistical simulation of the process of elastic scattering of atomic particles in a gas and in a solid. However, an important disadvantage of this interaction potential is the absence of correlation between the interaction cross section and the energy of relative motion of colliding particles.

In the case of particle interaction in a gas medium in the range of low energy values which do not exceed the respective ionization potentials, the elastic-scattering cross section is of the order of gas-kinetic and little depends on the energy of colliding particles. In this case, the classical hard-sphere scattering is a good approximation; in this energy range, the particle scattering (except for the case of small values of scattering angles) is assumed to be spherically symmetric, and the interaction between colliding particles is defined by their outer electron shells and must be determined for each pair of colliding particles. When the energy of relative motion of colliding particles increases, significant scattering occurs under conditions of considerable overlapping of their electron shells, and the interaction potential is largely defined by the inner electrons whose velocities are much higher than the collision rates of atomic particles. The excitation of outer electrons occurring in the process causes little variation in the scattering potential the effective range of whose action corresponds to smaller interatomic distances.

In describing the interaction of atomic particles in a solid, an empirical rule exists according to which the collisions leading to an appreciable scatter occur at distances of the order of half the equilibrium distance between neighboring atoms. In the case of such small distances, one can ignore the long-range attractive forces which define the bonding forces in solids. By the order of magnitude, this range of distances corresponds to the sizes of colliding atomic particles. Based on the same principle is the method of determining, to a first approximation, ionic and atomic radii [4]. Therefore, in a fairly wide range of energies of colliding atomic particles, the classical hard-sphere scattering is a good approximation from the practical standpoint.

In the hard-sphere model, the shortest distance within which two colliding particles come closer together, $r_{\min}$, for any values of the impact parameter b is always equal to the sum of radii of atomic particles and does not depend on the energy of their relative motion. This results in a considerable limitation, within the hard-sphere model, of the possibility of static simulation in a wide range of energy of colliding particles. Attempts were made previously [5–7] at describing the process of elastic scattering of atomic particles using the procedure of fitting the approximate potential of interaction to the real one for some distance between the atomic particles which makes the most contribution to the particle scattering. However, almost all of the derived approximate potentials of interaction are little valid for high impact parameters which lead to overestimated values of transmitted energy under conditions of elastic collision of atomic particles. The procedure of simulation of the processes of elastic scattering of atomic particles, suggested by us, restricts the range of high impact parameters at thermal energies of atomic particles by their gas-kinetic sizes. For high values of the energy of collision of atomic particles, the range of high impact parameters corresponds only to very small values of scattering angles and transmitted energy and plays no important part.

APPROXIMATION OF INTERATOMIC INTERACTION POTENTIAL

A combination of the simplicity of computational procedure in using the hard-sphere potential with the correctness of physical description of the processes of interaction of atomic particles may be accomplished by using the interatomic potential of quasihard spheres (QHS). We will treat in more detail the form and procedure of using the interatomic potential of interaction of QHS. A number of test potentials applicable to atoms of various elements and containing fitting parameters may be used as real interatomic potentials of interaction. Most convenient from the standpoint of mathematical application is the Born–Mayer interatomic potential [8]

$$U_{B-M}(r) = A_{B-M}(Z_1Z_2)^{3/4}\exp[-r/b_{B-M}], \qquad (2)$$

where Z_1 and Z_2 are ordinal (atomic) numbers of colliding atomic particles, and A_{B-M} and b_{B-M} are constants determined for each pair of colliding atomic particles.

This purely exponential interatomic potential of interaction enables one to analytically express the shortest distance $r_{\min}$ within which two colliding atomic particles come closer together from the equation

$$U_{B-M}(r_{\min}) = E_c, \qquad (3)$$

where E_c is the energy of relative motion in the center-of-mass system of two colliding atomic particles; the solution of this latter equation has the form

$$r_{\min}(E_c) = -b_{B-M}\ln\frac{E_c}{A_{B-M}(Z_1Z_2)^{3/4}} \qquad (4)$$

and, in the case of central collision ($b = 0$), defines the minimum distance between two atomic particles at the point of stopping during infinite motion of the incident particle. The use of other, more complex real interatomic potentials, whose solution relative to $r_{\min}$ does not permit an analytical solution for different values of the collision energy, is possible; however, it complicates the computational procedure of simulation and renders it less flexible as regards the adaptation to variations of conditions of real physical experiment.

If the value of the shortest distance $r_{\min}$ within which the atomic particles come closer together is identified with the sum of the radii of hard spheres at the point of contact (Fig. 1), one can use the hard-sphere model to determine the microscopic cross section for elastic scattering and the free path. In so doing, the sum of the hard-sphere radii is a variable quantity and varies as a function of the energy of relative motion of colliding atomic particles; from this standpoint, colliding atomic particles may be regarded as quasihard spheres.

The interatomic potential of quasihard spheres may be determined in the form

$$U_{\text{qhs}}(r) = \begin{cases} \infty \ \text{ for } \ r < r_{\text{hs}} = r_{\min}(E_c) \\ 0 \ \text{ for } \ r > r_{\text{hs}} = r_{\min}(E_c), \end{cases} \qquad (5)$$

where $r_{\min}(E_c)$ is the solution of equation (3) and, for the Born–Mayer interatomic potential (2), is defined by expression (4).

The criterion of validity of interatomic potential of interaction of quasihard spheres $U_{\text{qhs}}(r)$ may be formulated as follows:

$$\Delta r = r'_{\text{hs}} - r_{\text{hs}} < r_{\text{hs}} = r_{\min}(E_c), \qquad (6)$$

where r'_{hs} is the coordinate of intersection of the tangent (derivative of the real interatomic potential of

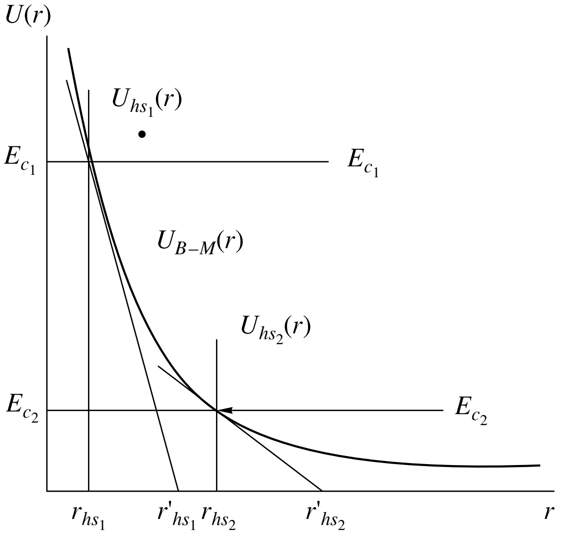

Fig. 1. Quasihard-sphere approximation for the potential $U_{B-M}(r)$ (central collision, $b = 0$).

interaction) drawn from the point $U_{\rm qhs}(r) = E_c$ with the axis of interatomic distance r (Fig. 1).

The use of the interatomic potential of interaction of quasihard spheres $U_{\rm qhs}(r)$ will be correct in case conditions (6) is valid or the equivalent relation depending on the collision energy E_c,

$$\frac{r}{\Delta r} = r\frac{|dU(r)/dr|}{U(r)} = r\frac{d\ln U(r)}{dr}\bigg|_{r = r_{\rm hs}} > 1. \quad (7)$$

If this criterion is generalized to the region of off-center ($b \neq 0$) collisions, it will take the form

$$\frac{r}{\Delta r} = r\frac{|dU(r)/dr|}{U(r)} > 1 - b^2/r^2. \quad (8)$$

If this criterion of interatomic potential of interaction of quasihard spheres (7) is applied to the real Born–Mayer interaction potential (2), we will derive the range of validity of the respective of quasihard-sphere interaction potential,

$$r(E_c) > b_{B-M} \approx 0.219 \text{ E}. \quad (9)$$

One can see from condition (9) that the potential of interaction of quasihard spheres with the Born–Mayer interatomic potential is well valid in the range of great interatomic distances to which correspond both low values of the collision energy and high values of the impact parameter in a wide range of the collision energy of atomic particles. For the exponential Born–Mayer interaction potential (2), this is associated with the fact that, as the interatomic distance r increases (Fig. 1), the quantity $\Delta r = r'_{\rm hs} - r_{\rm hs}$ increases slower than the quantity $r_{\rm hs} = r_{\rm min}(E_c)$, and their correlation ever better satisfies the criterion of validity (6) of the quasihard-sphere interaction potential.

In order to use the Born–Mayer interatomic potential in the quasihard-sphere model, we modified it using the results of Abrahamson [9] for a wide class of collision partners with the ordinal numbers $Z_{1,2} = 2\ldots80$. In so doing, the constants A_{B-M} and b_{B-M} in the Born–Mayer interatomic potential (2) were represented as the functions $A_{B-M}(Z_1, Z_2)$ and $b_{B-M}(Z_1, Z_2)$ and approximated using the results of [9, 10] with the power functions by the method of least squares. The approximation results are given in Fig. 2. The obtained coefficients of the modified Born–Mayer interatomic potential (2) have the form

$$\begin{aligned} A^{ap}_{B-M}(Z_1, Z_2) &= 95.863(Z_1Z_2)^{0.7383}, \text{ eV}, \\ b^{ap}_{B-M}(Z_1, Z_2) &= 0.122(Z_1^{0.0387} + Z_2^{0.0387}), \text{ Å}. \end{aligned} \quad (10)$$

The maximum relative error of approximation of the coefficients $A^{ap}_{B-M}(Z_1, Z_2)$ and $b^{ap}_{B-M}(Z_1, Z_2)$, corresponding to the collision of the lightest atomic particles, does not exceed 8% and, in the case of heavy atomic particles, decreases to 3%. In so doing, the modified Born–Mayer interatomic potential of interaction of atomic particles with the ordinal numbers Z_1 and Z_2 assumes the form

$$\begin{aligned} \tilde{U}_{B-M} &= 95.863(Z_1Z_2)^{0.7383} \\ &\times \exp\left[-\frac{r}{0.122(Z_1^{0.0387} + Z_2^{0.0387})}\right], \end{aligned} \quad (11)$$

where $\tilde{U}_{B-M}$ and r are in eV and Å, respectively.

The solution of equation (3) for this modified Born–Mayer interatomic potential (11) has the form

$$\begin{aligned} r_{\rm min}(E_C) &= -0.122(Z_1^{0.0387} + Z_2^{0.0387}) \\ &\times \ln\frac{E_C}{95.863(Z_1Z_2)^{0.7383}}E. \end{aligned} \quad (12)$$

The criterion of validity (7) of the potential of interaction of quasihard spheres with the derived modified Born–Mayer potential (11) takes the form

$$r(E_c) > 0.122(Z_1^{0.0387} + Z_2^{0.0387})E. \quad (13)$$

Within the obtained quasihard-sphere model, the microscopic cross section for elastic interaction of atomic particles depends on the energy E_C of their relative motion,

$$\sigma_{\rm qhs} = \pi r^2_{\rm min}(E_C) \quad (14)$$

and, accordingly, the free path $\lambda_{\rm qhs}$ of atomic particles in a gas medium or in a solid is

$$\lambda_{\rm qhs} = \frac{1}{N\pi r^2_{\rm min}(E_C)}, \quad (15)$$

where N is the concentration of atomic particles in a scattering medium.

If, in statistical simulation, the ratio between b^2 and the quantity $r^2_{\min}(E_c)$ is equated to a random number ξ, the expression for the scattering angle ϑ in the laboratory coordinate system assumes the form

$$\vartheta = \arctan\frac{2[\xi(1-\xi)]^{1/2}}{2\xi - 1 + M_1/M_2}. \qquad (16)$$

In determining the impact parameter b in the form

$$b = r_{\min}(E_c)\xi^{1/2}, \qquad (17)$$

we take into account the increase in the probability of high (in absolute magnitude) values of the impact parameter b, which is due to the fact that an incident atomic particle arrives by chance at different points of the area of the microscopic cross section for scattering.

Given in Fig. 3 by way of example are the results of calculations of free path (15) of Cu atoms under conditions of elastic scattering from Ar atoms, obtained within the quasihard-sphere model with the modified Born–Mayer interatomic potential (11) and normalized to the respective value of free path in the hard-sphere model, as a function of the energy of their relative motion.

The calculation results indicate that the microscopic cross section of elastic scattering of atomic particles $\sigma_{\text{qhs}} \sim 1/\lambda_{\text{qhs}}$ increases, as the energy of their relative motion decreases, to reach the value of gas-kinetic cross section at thermal collision energies. As the collision energy increases, the elastic scattering cross section decreases to a value restricted by the criterion of validity (7) of the quasihard-sphere model. The maximum collision energy corresponding to the limit of the criterion of validity of the quasihard-sphere model (13) using the modified Born–Mayer interatomic potential (11), under conditions of elastic scattering of Cu atoms from Ar atoms is restricted to ~5 keV. This energy range of interaction of atomic particles is of interest from the standpoint of numerous applied problems of the physics of plasma, gas discharge, and solid.

DISCUSSION

Previous attempts have been made [11–14] to introduce into the hard-sphere model the dependence of the interaction cross section on the energy of colliding particles. However, as is seen in Fig. 3 (curve *3*), the most rigorous energy dependence of the elastic-scattering cross section, proposed in [13], which includes the Maxwellian velocity distribution of gas atoms, is little valid in the entire range of energy of colliding particles and reaches the value of gas-kinetic interaction cross section at high energies of colliding particles, which is incorrect.

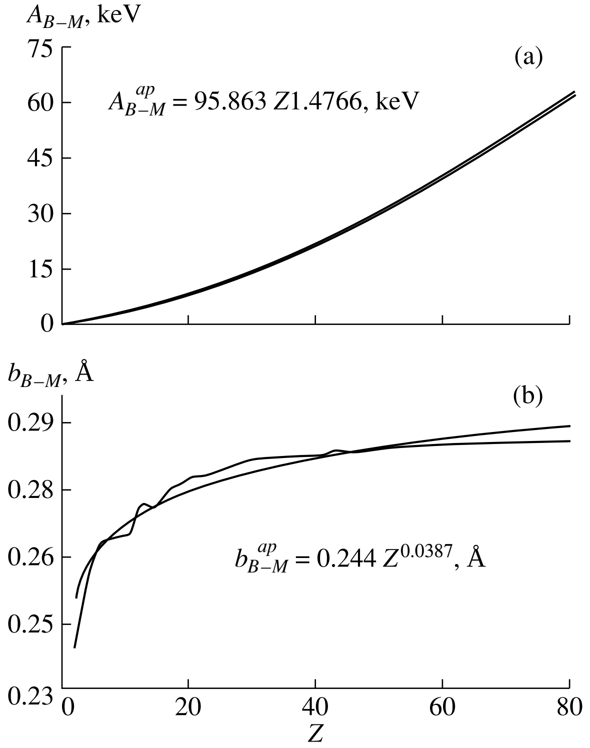

Fig. 2. Approximation of coefficients in the modified Born–Mayer interatomic potential (11): (a) $A^{ap}_{B-M}(Z_1, Z_2)$, (b) $b^{ap}_{B-M}(Z_1, Z_2)$.

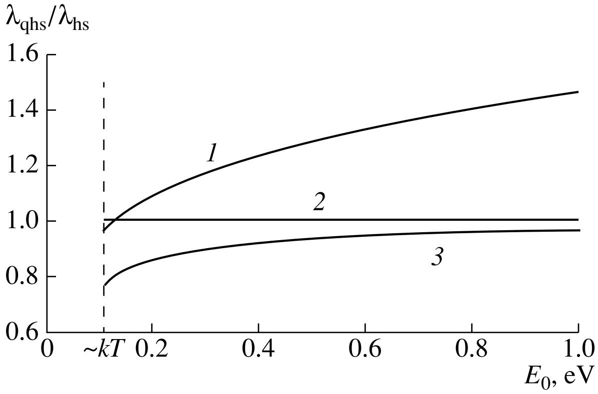

Fig. 3. The free path of Cu atoms upon elastic scattering from Ar atoms as a function of the energy of their relative motion: (*1*) qhs, (*2*) hs, (*3*) [13].

The application of more real interatomic potentials of interaction results in the necessity of using mathematical procedures which introduce some determinism into the random process of scattering. For example, the use in [14] of the scattering "6–12" Lennard–Jones potential by the procedure of linearization of the scattering angle Θ in the center-of-mass from the impact parameter b enabled one to estimate the maximum interaction cross section from the condition $\Theta = 0$ at $b = b_{\max}$. However, the linear approximation in this case implies that the scattering angle Θ is estimated with inadequate accuracy with the value of the impact parameter b close to maximum. This results in a considerable underestimation of the contribution of scattering in the case of glancing collision and, accordingly, the value of the interaction cross section.

In order to check the degree of the fit of the quasihard-sphere model to the description of processes of elastic scattering of atomic particles involving the use of real interatomic potentials, the results of simulation of processes of transport of atomic particles in a gas were compared to those in a solid. The real interatomic potential of interaction was provided by the modified Firsov potential [15],

$$U(r) = \frac{z_1 z_2 e^2}{r}\psi\left(-\frac{r}{a_f}\right), \tag{18}$$

where $a_f = 0.8853a_0/(Z_1^{1/2} + Z_2^{1/2})^{2/3}$ is Firsov's screening parameter (a_0 is the Bohr radius) with Nikulin's screening function [16] obtained by approximate solution of the Thomas–Fermi equation using the variation principle,

$$\psi_c(r) = [a\exp(-\alpha/a_f r) + b\exp(\beta/a_f r)]^2, \tag{19}$$

where $a = 0.7111$, $b = 0.2889$, $\alpha = 0.175$, and $\beta = 1.6625$.

In order to perform numerical integration in expression (1) when determining the scattering angle Θ with interaction potential (18), we developed a mathematical procedure according to which the integration interval $[r_{\min}, \infty]$ in expression (1) is divided into three regions.

In the first region $r_{\min} < r < (r_{\min} + \delta)$, the integrand in the denominator of expression (1) $f(r) = 1 - U(r)/E_c - b^2/r^2$ is expanded by its Taylor series expansion,

$$\begin{aligned} f(r) &= f(r_{\min}) + f'(r_{\min})(r - r_{\min}) \\ &\quad + f''(r_{\min})(r - r_{\min})^2/2 + \dots \\ &\approx (r - r_{\min})(f'(r_{\min}) + f''(r_{\min})(r - r_{\min})/2). \end{aligned} \tag{20}$$

The relative error of these transformations is estimated at

$$\Delta = \frac{f'''(r_{\min})}{f'(r_{\min})} - \frac{(r - r_{\min})^2}{6}.$$

At $\delta = 0.01$ ($r = r_{\min} + 0.01$), the value of Δ does not exceed $\sim 10^{-4}$.

The upper limit Q of the second region $(r_{\min} + \delta) \le r \le Q$. This is the value of r at which the second term $U(r)/E_c$ of the function $f(r)$ becomes small and, in what follows, may be ignored. We took $U(r)/E_c < 10^{-6}$ as the smallness criterion.

In the third region $Q < r < \infty$, the integral in expression (1) has an analytical solution in the form

$$\int_Q^{\infty} \frac{dr/r^2}{[1 - U(r)/E_c - b^2/r^2]^{1/2}} = \frac{1}{b}\arcsin\left(\frac{b}{Q}\right). \tag{21}$$

It is almost impossible to perform numerical integration in expression (1) directly in the process of simulation, because this extends considerably the time of static simulation. Therefore, the values of scattering angles $\Theta(b, E_c)$ were first calculated for a wide range of values of the energy E_c of relative motion of colliding atomic particles, with the range of values of the impact parameter b from 0 to $b_{\max}$ corresponding to each one of those energy values. The value of the maximum impact parameter $b_{\max}$ for each value of the collision energy E_c was determined from the condition $\Theta(b = b_{\max}) \approx 0$. The calculation results were used to compile a two-dimensional array of values of the scattering angles $\Theta(b, E_c)$, between the elements of which a spline approximation was performed. This two-dimensional array $\Theta(b, E_c)$, calculated for concrete collision partners, was used in static simulation to determine the value of the scattering angle Θ in each collision event.

In order to compare the results of statistical simulations involving the interatomic quasihard-sphere potential (5), the modified Born–Mayer interaction potential (11), and the real potential of interaction (18), the processes of transport of Cu, Y, and Ba atoms in a medium of Ar and O_2 were calculated.

An analysis of results of statistical simulation reveals that both models agree in the low-energy region and differ slightly when the collision energy increases. This may be due to the fact that modified Firsov's potential (18) with Nikulin's screening function (19) in the case of in the case of large internuclear distances decreases slower than the true interaction potential. Moreover, the modified Born–Mayer interaction potential (11), employed by us in the quasihard-sphere model, is more valid in the case of large internuclear distances which are characterized by interactions between the outer electron shells of colliding atomic particles. The quasihard-sphere model with modified Born–Mayer interaction potential adapts itself better to various combinations of collision partners, because it contains parameters characteristic of concrete pairs of colliding atomic particles.

It is almost impossible to derive the universal interatomic potential of interaction in an analytical form, which could be used in application to a wide class of problems in statistical simulation: even in describing the processes of scattering of particles in a gas medium due to the differences in the electron structure of colliding atoms the real interatomic potential of interaction is not monotonic, and oscillations due to the shell structure of colliding atoms must show up in elastic-scattering cross sections. In addition, the assumptions made in deriving almost all of the known interatomic potentials of interaction used to describe the processes of scattering of particles in a solid were obtained within the statistical theory of scattering and based on the principles of binarity and independence of collisions characteristic of a gas medium, which is incorrect.

Within the obtained quasihard-sphere model (5) using the modified Born–Mayer interatomic potential (11), calculations were performed of the transport coefficients of atoms in a gas medium at different values of gas pressure up to pressures at which the diffusion motion of atoms being scattered is predominating. Also calculated were the values of ion sputtering in describing the processes of displacement of atoms in a solid and their motion toward the surface. The calculation results obtained for a wide class of collision partners have demonstrated that the suggested model of quasihard-sphere model using the modified Born–Mayer interatomic potential enables one to fairly correctly simulate the processes of elastic scattering of atomic particles at high rates of statistical simulation.

REFERENCES

1. L. D. Landau and E. M. Lifshits, *Mechanics* (Nauka, Moscow, 1973; Pergamon, Oxford, 1976).
2. V. A. Vol’pyas, E. K. Gol’man, and M. A. Tsukerman, Zh. Tekh. Fiz. **66** (4), 16 (1996).
3. W. D. Wilson, L. G. Haggmark, and J. P. Biersack, Phys. Rev. B **15**, 2458 (1977).
4. L. Pauling, *The Nature of the Chemical Bond*, 3rd ed. (New York, 1960).
5. G. Leibfried and O. S. Oen, J. Appl. Phys. **33**, 2257 (1962).
6. C. Lechmann and M. T. Robinson, Phys. Rev. **134** (1A), A37 (1964).
7. W. M. MacDonald, Am. J. Phys. **41**, 1337 (1973).
8. M. Born and J. E. Mayer, Z. Phys. **75**, 1 (1932).
9. A. A. Abrahamson, Phys. Rev. **178**, 76 (1969).
10. V. I. Gaydaenko and V. K. Nikulin, Chem. Phys. Lett. **7**, 360 (1970).
11. D. K. Holmes, in *Radiation Damage in Solids* (IAEA, Vienna, 1962), Vol. 1, p. 3.
12. R. E. Somekn, Vacuum **34**, 987 (1984).
13. A. G. Zhiglinskiĭ, V. V. Kuchinskiĭ, and E. G. Sheĭkin, Zh. Tekh. Fiz. **56**, 1718 (1986) [Sov. Phys. Tech. Phys. **31**, 1022 (1986)].
14. G. M. Turner, I. S. Falconer, B. W. James, and D. R. McKenzie, J. Appl. Phys. **65**, 3671 (1989).
15. O. B. Firsov, Zh. Éksp. Teor. Fiz. **33**, 696 (1957) [Sov. Phys. JETP **6**, 534 (1957)].
16. V. K. Nikulin, Zh. Tekh. Fiz. **41**, 567 (1971) [Sov. Phys. Tech. Phys. **16**, 439 (1971)].

Translated by Henri A. Bronstein

Technical Physics, Vol. 45, No. 3, 2000, pp. 304–308. Translated from Zhurnal Tekhnicheskoĭ Fiziki, Vol. 70, No. 3, 2000, pp. 19–23.
Original Russian Text Copyright © 2000 by Udovichenko.

GAS DISCHARGES, PLASMA

Electric Strength of an Accelerating Gap in a Plasma Source of Charged Particles

S. Yu. Udovichenko

Efremov Research Institute of Electrophysical Equipment, St. Petersburg, 189631 Russia

Received March 18, 1998; in final form, October 6, 1999

Abstract—An investigation is performed on the electric strength of accelerating gaps of plasma sources of electrons and ions in the presence of beam plasma behind the accelerating electrode. For the bipolar mode, when the gas ionization in the accelerating gas may be ignored, the conditions of bridging the gap of plasma discharge of a source with beam plasma and of disruption of emission current are found. *© 2000 MAIK “Nauka/Interperiodica”.*

INTRODUCTION

Electron and ion beams generated from plasma sources are transported in a residual gas medium. The leakage of gas into the accelerating gap and drift space of the beam occurs from the source proper. In the case of formation of high-current beams of charged particles in focusing devices with magnetooptics and of transport through long distances, use is made of forced bleeding-in of gas for the purpose of reducing the effect of space charge on the dynamics of fast particles. Under these conditions, a plasma is formed behind the accelerating electrode as a result of ionization by a beam of gas atoms, this plasma compensating for the space charge of accelerated particles. The plasma density may exceed considerably that of the beam particles. Charged particles of the sign opposite to that of the beam from the plasma source are extracted from the beam plasma into the accelerating gap.

The electric breakdown of accelerating gap restricts the extreme conditions of operation of plasma sources. The breakdown conditions are defined by the properties of plasma in the source and behind the accelerating electrode, as well as by the characteristics of the gap proper. In its turn, the gap length depends on the properties of the beam plasma and plasma of the source.

The ignition of a semi-self-maintained discharge in the accelerating gap of an electron source with a glowing cathode is treated in [1–3]. The conditions of breakdown of the gap have been found which take into account the gas ionization by electron beam and partial compensation of a space charge of the beam by ions from the plasma behind the accelerating electrode.

The major difference in plasma emitters from thermionic guns consists in that no restriction of current by the space charge is possible during extraction of electrons or ions from the plasma. The current flowing in the accelerating gap is a saturation current and is defined by the density and temperature of the source plasma. A variation of these parameters under conditions of constant accelerating voltage leads to a displacement of the emitting plasma surface resulting in the recovery of zero intensity of electric field on this surface. Kreĭndel’ and Nikitinskiĭ [4] investigated the condition of electric breakdown of the accelerating gap during extraction of electrons from the plasma surface, when their space charge was partly compensated as a result of gas ionization in the gap. However, the derived equation describing the condition of discharge ignition has no solution for the case of the emissivity of the source plasma exceeding the transmissivity of the gap. Note that no references to the results of this latter study are made in the later monograph [5].

The inverse electron current coming from a beam plasma exceeds considerably the current from an ion source and causes an increases release of power on the plasma electrode. Therefore, first the accelerating and then the decelerating electrodes are used to shape an ion beam; in so doing, the electrons from the beam plasma cannot get into the source. The inverse electron current from the beam plasma to the source may be reduced with the aid of transverse magnetic field in the accelerating gap. In an ion source [6] with closed electron drift, when the Larmor electron radius is equal to the gap length, the compensation of space charge and a considerable increase of the ion beam current are provided. However, the transverse magnetic field distorts the trajectories of accelerated ions. In shaping precision ion beams, the need arises for compensating their space charge with the aid of inverse electron current in the absence of external magnetic field. This helps reduce the effect of space charge on the dynamics of the ion beam and minimize the nonlinear distortions of its phase characteristics.

This paper deals with the investigation of the electric strength of the accelerating gap of plasma sources of electrons and ions with a high emissivity in the presence of beam plasma behind the accelerating electrode and at a low gas pressure, when the motion of charged

1063-7842/00/4503-0304$20.00 © 2000 MAIK “Nauka/Interperiodica”

particles in the gap occurs under conditions of free flight. We will demonstrate that, with this formulation of the problem, it is the extent of the space charge layer between the source plasma and beam plasma, which is the determining criterion of strength rather than the ionization process.

PLASMA SOURCE OF ELECTRONS

We will treat a junction-type plasma diode consisting of an electron-emitting plasma surface, an accelerating gap of length x_A between the emitting surface and electrode at potential φ_A, and a beam plasma surface coinciding or not coinciding with the electrode surface. An electron current of density j_e and an inverse electron current of density j_i flow in the space charge layer between two plasma surfaces.

We will assume that the electrons and ions in the layer move in the free flight mode, and the gas ionization is performed by primary electrons alone. In this case, Poisson's equation has the form [3]

$$\frac{d^2y}{dz^2} = \frac{4}{9}\frac{j_e}{j_{e0}}\left[\frac{1}{y^{1/2}} - \frac{\alpha_e}{(1-y)^{1/2}} - \eta_{e1}\int\limits_{\xi(z)}^{1}\frac{\sigma_i^e(y')/\sigma_0}{[y'(z')-y(z)]^{1/2}}dz'\right], \tag{1}$$

where $y = \varphi/\varphi_A$, φ is the electric field potential, $z = x/x_A$, x is the coordinate along the direction of electron emission, $\alpha_e = (j_i/j_e)(m_i/m_e)^{1/2}$, $\eta_{e1} = n_{gC}x_A\sigma_0(m_i/m_e)^{1/2}$; $\sigma_i^e = \sigma_0(I/\varphi_A y)(1 - I/\varphi_A y)$, σ_0 is the maximum cross section of electronic ionization of gas, I is the ionization potential, n_{gC} is the gas density in the layer, $\xi(z) = z$ at $z \subset [z(I/\varphi), 1]$ and $\xi(z) = z(I/\varphi)$ at $z \subset [0, z(I/\varphi)]$, $j_{e0} = en_{e0}(kT_{eS}/2\pi m_e)^{1/2}$ is the density of thermal current from the plasma source, and n_{e0} and T_{eS} respectively denote the electron density and temperature.

The electron current flowing in the accelerating gap is a saturation current, $j_{e0} = (2e/m_e)^{1/2}(\varphi_A^{3/2}/9\pi x_A^2)$, and the parameter x_A defines the extent of the layer of space charge between the steady-state plasma boundary of the source with coordinate $x = 0$ and the accelerating electrode in the absence of gas ionization and ion current from the beam plasma.

We will find the distribution of the electric field in the layer by integrating (1) in view of nonzero boundary condition on the plasma emitter, $(dy/dz)_{z=0} = 0$,

$$\frac{dy}{dz} = \frac{4}{3}\left(\frac{j_e}{j_{e0}}\right)^{1/2}\{y^{1/2} + \alpha_e[(1-y)^{1/2} - 1]\}^{1/2}. \tag{2}$$

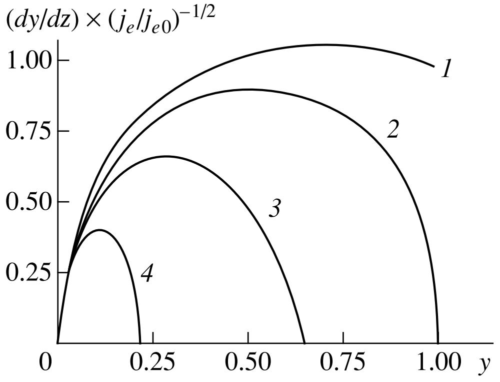

The distribution of the electric field as a function of the parameter y: (*1*) $\alpha_e = 0.5$, (*2*) 1, (*3*) 2, (*4*) 4.

Equation (2) is derived ignoring the electron-beam ionization of gas,

$$n_{gC} \ll \frac{4\alpha_e}{3x_A\sigma_0}\left(\frac{m_e}{m_i}\right)^{1/2}\left(\frac{\varphi_A}{I}\right)^{1/4}\left(\frac{j_e}{j_{e0}}\right)^{1/2}. \tag{3}$$

Here, use is made of the estimation of integrals in equation (1), made in [1], $\max\Phi(y = \varphi/I) \le 1$, and the replacement of variable by $y = \varphi/\varphi_A$, as well as of the first approximation for the field $dy/dz \approx (4/3)(j_e/j_{e0})^{1/2}y^{1/4}$ in the region of the main contribution to the integral ($y \ll 1$) at $\alpha_e \ll (\varphi_A/I)^{1/2}$.

The coefficient α_e is defined by the conditions of the generation of plasma by a beam behind the accelerating electrode. In view of the fact that a thermal ion current is delivered from this plasma into the layer, we have the following expression for α_e:

$$\alpha_e = 0.4\frac{n_{iA}}{n_{eA}}\left(\frac{kT_{eA}}{e\varphi_A}\right)^{1/2}, \tag{4}$$

where n_{eA} is the density of beam electrons behind the accelerating electrode, T_{eA} is the electron temperature, and n_{iA} is the density of beam plasma ions.

We assume that all ions of beam plasma moving towards the boundary go into the layer, i.e., the current is always a saturation current. In order to determine the degree of excess of the density of plasma over that of electron beam, we use the results of [7],

$$\frac{n_{iA}}{n_{eA}} = \left(\frac{2e\varphi_A}{m_e}\right)^{1/2}\frac{\sigma_i^e(\varphi_A)n_{gA}r_b^2\nu_{i0}}{4v_s^2}\ln\frac{R_A}{r_b}, \tag{5}$$

where $\sigma_i^e(\varphi_A)$ is the absolute value of the cross section of electronic ionization of gas at $\varphi = \varphi_A$, n_{gA} is the density of gas behind the electrode, r_b is the beam radius, R_A is the casing radius, $v_s = (kT_{eA}/m_i)^{1/2}$ is the ion sound velocity with which the ions move from the plasma to the chamber wall, T_{iA} is the ion temperature, $\nu_{i0} = (32\sigma_{ex}/3^{1/2})n_{gA}(kT_{iA}/m_i)^{1/2}$ is the collision frequency of plasma ions with gas atoms during resonance exchange of charge [8], and σ_{ex} is the cross section of resonance exchange of charge.

In deriving expression (5), it was assumed that the plasma formed by the beam moved in a radial direction in the mode of ambipolar diffusion and was lost on the casing walls. If the beam drift length $L \gg R_A$, the ambipolar electric field and the inhomogeneity of plasma along the beam may be ignored.

An analysis of the electric field distribution (2) as a function of the variable y reveals (see figure) that, at a low gas pressure ($\alpha_e < 1$), the field at the boundary of accelerating electrode is other than zero, and the beam plasma boundary shifts behind the electrode. As the gas pressure increases, at $\alpha_e = 1$, the plasma boundary coincides with the electrode surface and, at $\alpha_e > 1$, the field goes to zero inside the accelerating gap at the point $y_{1e} = 4\alpha_e^2/(1 + \alpha_e^2)$. In the latter case, a potential well emerges for ions leaving the beam plasma. This well is filled until it goes to zero accurate within the field in the plasma. As a result, the region between y_{1e} and $y = 1$ is filled with plasma. The motion of the beam plasma boundary deep into the accelerating gap with an increase of the gas pressure was observed experimentally [9].

The potential distribution over the charged layer length is determined by integrating (2),

$$z = \frac{3}{4}\left(\frac{j_{e0}}{j_e}\right)^{1/2}\int_0^y \{y^{1/2} + \alpha_e[(1-y)^{1/2} - 1]\}^{-1/2} dy + z_0, \quad (6)$$

where z_0 is the coordinate of the source plasma boundary.

The integral $F(y)$ appearing on (6) is reduced to an elliptic integral [5] by change of variables, i.e., it is a tabulated function, or is calculated numerically.

The position of the emitting surface in the source is related to the emissivity of plasma proper. An increase in the emissivity of the source plasma occurs owing to the ion current coming to the plasma from the accelerating gap. The ions entering the plasma cause a local increase in the positive charge density; this leads, on conditions of continued quasineutrality of the plasma, to a respective increase in the electron density and, consequently, to an increase of the electron emission current. In the absence of inverse ion current, the source plasma boundary takes the initial position ($z_0 = 0$ at $y = 0$). Under conditions of a high emission current, the source plasma boundary shifts deeper into the accelerating gap. This inference was verified experimentally in [5, 10]. The charged layer length in this case, according to (6), is defined by the expression

$$z_1 - z_0 = \frac{3}{4}F(y_{1e})\left(\frac{j_{e0}}{j_e}\right)^{1/2}, \quad (7)$$

where z_1 is the coordinate of the beam plasma boundary, y_{1e} is the potential at this boundary, and the integral $F(y_{1e})$ is defined in (6).

We will determine the emissivity of the source plasma analogously [5]. The charge exchange is the main process of interaction between ions and the source plasma at a high gas pressure. A significant part of ions are subjected to resonance exchange of charge on neutral gas atoms in the vicinity of the boundary of current takeoff of electrons and, due to diffusion, leave this region. The ion beam introduces substantial longitudinal nonuniformity compared with radial nonuniformity in the case of ambipolar diffusion of plasma across the beam. The equation of one-dimensional diffusion of ions after charge exchange in view of the balance equation for ion beam particles has the form

$$D_A\frac{d^2 n_i(z)}{dz^2} = \frac{j_i}{e}\sigma_{ex}n_{gS}\exp(\sigma_{ex}n_{gS}z),$$

where $z \le 0$, $D_A(dn_i/dz) = 0$ at $z = 0$, $n_i = n_{i0}$ at $j_i = 0$, $D_A = 2T_{eS}/m_i\nu_{i0}$, the frequency of resonance exchange of charge ν_{i0} is defined in (5), and the cross section of resonance exchange of charge σ_{ex} may be assumed constant and the same for primary and secondary ions until the energy of 30 keV. Double integration of equation (8) gives the increment of the electron density on the plasma boundary ($z = 0$) at $n_i(z) = n_e(z)$ and $n_{i0} = n_{e0}$.

The electron density of emission current from the source plasma may be represented as

$$j^*_{e0} = j'_{e0} + \gamma_e j_i, \quad (9)$$

where $\gamma_e = (kT_{eS}/2\pi m_e)^{1/2}(D_A n_{gS}\sigma_{ex})^{-1} = (16k/\sqrt{3\pi})(T_{iS}m_i/2T_{eS}m_e)^{1/2}$ is the coefficient of ion-electron emission of plasma; T_{iS} is the ion temperature in the source, $T_{eS} \gg T_{iS}$; $j_i = \alpha_e j_e(m_e/m_i)^{1/2}$; j'_{e0} is the vacuum component of the current density in the accelerating gap of length z_1 prior to variation of the position of the source plasma boundary. The total current in the charged layer is made up of the vacuum component and the current associated with the compensation of the space charge of the electron beam. Assuming that the behavior of potential distribution in the layer in the presence of inverse ion current does not vary [4], the vacuum component of the current density may be represented as

$$j'_{e0} = j_{e0}/z_1^2, \quad j^*_{e0} = j_{e0}/(z_1 - z_0)^2, \quad (10)$$

where j_{e0} is the vacuum density in a gap of length $z = 1$.

A simultaneous solution of equations (7), (9), and (10) gives the condition

$$1 - \alpha_e\gamma_e\left(\frac{m_e}{m_i}\right)^{1/2}F^2(y_{1e}) = \left(1 - \frac{z_0}{z_1}\right)^2, \quad (11)$$

at which the bridging of the gap of plasma discharge of a source with beam plasma occurs ($z_1 = z_0$), as well as the disruption of electron current in the accelerating gap. Note that the condition of breakdown of the gap (11) is associated both with the critical density of gas in the gap and with the density of gas in the source and in the channel of free drift of the electron beam behind the accelerating gap. The gas pressure in the source may differ from that in the accelerating gap by two or more orders of magnitudes.

PLASMA SOURCE OF IONS

When the potential φ_A across the accelerating gap is replaced by $-\varphi_A$, a plasma source of electrons becomes an ion source. We will treat ion sources in which no provision is made for the restriction of the inverse electron current of high density $j_e/j_i > (m_i/m_e)^{1/2}$ delivered from the beam plasma behind the accelerating electrode.

Poisson's equation for space charge in the accelerating gap of an ion source in view of electron emission from the surface of beam plasma has a form analogous to that of (1),

$$\frac{d^2y}{dz^2} = -\frac{4}{9}\frac{j_i}{j_{i0}}\left[\frac{1}{y^{1/2}} - \frac{\alpha_i}{(1-y)^{1/2}} - \eta_{e2}\int\limits_{\xi(z)}^{1}\frac{\sigma_i^e(y')/\sigma_0}{[y(z)-y'(z')]^{1/2}}dz'\right], \tag{12}$$

where $\alpha_i = (j_e/j_i)(m_e/m_i)^{1/2}$; $\eta_{e2} = n_{gC}x_A\sigma_0(m_e/m_i)^{1/2}$; $j_{i0} = 0.4en_{i0}(2kT_{eS}/m_i)^{1/2} = (2e/m_i)^{1/2}(\varphi_A^{3/2}/9\pi x_A^2)$; $\sigma_i^e = \sigma_0(I/\varphi_A)(y_{1i}-y)^{-1}[1-I/\varphi_A(y_{1i}-y)^{-1}]$, and $y_{1i} = 4\alpha_i^2/(1+\alpha_i^2)^2$.

The electric field distribution in the layer is defined by an expression analogous to (2). The condition of ignoring the electron-beam ionization of gas in this case assumes the form

$$n_{gC} \ll \frac{\alpha_i^{3/2}}{4x_A\sigma_0}\left(\frac{m_i}{m_e}\right)^{1/2}\left(\frac{\varphi_A}{I}\right)^{1/2}\frac{F(y_{1i})}{z_1-z_0}. \tag{13}$$

Here, use is made of the same approximation as in deriving inequality (3); in so doing, in the region of maximum ionization of gas at $y = y_{1i} - I/\varphi_A$, the electric field is of the order of $dy/dz \approx (2/3)\alpha^{1/2}(j_i/j_{i0})^{1/2}(y_{1i} - y)^{1/2}$.

The main contribution to the integral entering (12) is made by the region $\rho = I/\varphi_A$, where $\rho = y_{1i} - y$ is a new variable. In inequality (3), expression (7) is used for the gain of electron current density. A similar expression for the gain of ion current density enters (13).

For transporting an accelerated ion beam without substantial loss of particles, one must select the optimum drift length and gas density behind the accelerating electrode $L\sigma_{ex}n_{gA} \ll 1$, where L is the transporting length. Under conditions of reduced gas pressure, the plasma behind the accelerating electrode is generated only as a result of fast-ion ionization of neutral atoms. The coefficient α_i is determined analogously to (4): $\alpha_i = (kT_{eA}/4\pi e\varphi_A)^{1/2}\beta_i$, where β_i is the ratio of the ion beam density at the outlet from the accelerating gap to the electron density in the beam plasma. The quantity β_i is defined by an expression similar to (5), in which the electron ionization cross section $\sigma_i^e(\varphi_A)$ must be replaced by the respective cross section for ions $\sigma_i^i(\varphi_A)$, and m_e must be replaced by m_i. The cross section of ionization by singly charged ions in a first approximation is the same as in the case of electrons with the same velocity of particles. In electron and ion plasma sources with the same accelerating potential, $a_e \approx a_i$, because $\sigma_i^e/\sigma_i^i = (m_e/m_i)^{1/2}$.

A local increase of the plasma density in the vicinity of the emitting surface of an ion source is due to the ionization of gas in the source chamber by inverse electron current. The ion density of current from the plasma source will be defined by the expression $j_{i0}^* = j_{i0} + \gamma_i j_e$, where γ_i is the coefficient of electron-ion emission of plasma. We use the derivation of expression (5) to derive $\gamma_i = [\sigma_i^e(\varphi_A)n_{gS}r_b^2\nu_{i0}/4v_s^2]\ln(R_S/r_b)$, where R_S is the radius of the source chamber.

The conditions of bridging the gap of plasma discharge in an ion source with beam plasma ($z_1 = z_0$) may be written analogously to (11),

$$1 - \alpha_i\gamma_i\left(\frac{m_i}{m_e}\right)^{1/2}F^2(y_{1i}) = \left(1 - \frac{z_0}{z_1}\right)^2. \tag{14}$$

CONCLUSION

The ignition of a discharge as a result of ionization of gas in the accelerating gap of a diode occurs if the gas density exceeds the critical value [1, 3],

$$n_{gC} \geq \frac{2}{x_A\sigma_0}\left(\frac{m_e}{m_i}\right)^{1/2}\left(\frac{\varphi_A}{I}\right)^{3/4}F(y = 1).$$

In case conditions (3) and (13) are valid, as well as the condition of the mode of passing ions and of the absence of their charge exchange in gas $n_{gC} \ll (x_A\sigma_{ex})^{-1}$, the processes of formation of secondary particles in the accelerating gap may be ignored. A comparison of (3) and (13) demonstrates that the condition of ignoring ionization in the gap in the case of a plasma source of ions is less rigid than in the case of an electron source.

As the gas pressure decreases, the electric strength of the gap must increase. However, in the bipolar mode as well, when the gas ionization may be ignored, the electric strength of the accelerating gap remains low because of the possibility of bridging the gap of plasma discharge of a source with beam plasma behind the accelerating gap. A comparison of formulas (11) and (14) reveals that, as the pressure in the gas-discharge chamber increases (at $\gamma_i > \gamma_e m_e/m_i$), such a breakdown in the case of an ion source occurs at a lower pressure of gas in the accelerating gap than in the case of an electron source.

Note an important fact distinguishing the operation of a plasma emitter from that of a thermal emitter. In plasma sources of charged particles with an increased emissivity, when the gas pressure in the accelerating gap increases, the bridging of the gap of plasma discharge of a source with beam plasma may occur before the discharge ignition as a result of ionization of gas.

REFERENCES

1. N. S. Ivanova and K. N. Ul’yanov, Radio Élektron., No. 9, 1920 (1972).
2. V. I. Babanin and A. Ya. Énder, Zh. Tekh. Fiz. **49**, 2606 (1979) [Sov. Phys. Tech. Phys. **24**, 1471 (1979)].
3. Ya. I. Londer and K. N. Ul’yanov, Teplofiz. Vys. Temp. **17**, 949 (1979).
4. Yu. E. Kreĭndel’ and V. A. Nikitinskiĭ, Zh. Tekh. Fiz. **41**, 2378 (1971) [Sov. Phys. Tech. Phys. **16**, 1888 (1971)].
5. M. A. Zav’yalov, Yu. E. Kreĭndel’, A. A. Novikov, and L. P. Shanturin, *Plasma Processes in Technical-Grade Electron Guns* (Énergoatomizdat, Moscow, 1989).
6. Yu. P. Maishev, Prib. Tekh. Éksp., No. 1, 183 (1980).
7. S. Yu. Udovichenko, Fiz. Plazmy **22**, 149 (1996) [Plasma Phys. Rep. **22**, 137 (1996)].
8. V. A. Rozhanskiĭ and L. D. Tsendin, *Collision Process in Partly Ionized Plasma* (Énergoatomizdat, Moscow, 1988), p. 31.
9. G. I. Guseva, M. A. Zav’yalov, L. A. Neganova, *et al.*, Radio Élektron., No. 8, 1634 (1984).
10. V. A. Gruzdev, Yu. E. Kreĭndel’, and Yu. M. Larin, Zh. Tekh. Fiz. **43**, 2318 (1973) [Sov. Phys. Tech. Phys. **18**, 1465 (1973)].

Translated by Henri A. Bronstein

Technical Physics, Vol. 45, No. 3, 2000, pp. 309–311. Translated from Zhurnal Tekhnicheskoĭ Fiziki, Vol. 70, No. 3, 2000, pp. 24–26.

Healing Fatigue Damage in Steel with Electric Current Pulses

L. B. Zuev, O. V. Sosnin, S. F. Podboronnikov, V. E. Gromov, and S. N. Gorlova
Siberian State Industrial University, Novokuznetsk, Kemerov oblast, 654007 Russia
Received November 16, 1998

Abstract—A 15–30% enhancement of steel resource upon low-cycle fatigue tests is achieved by steel treatment with power electric current pulses at the instant when a sharp decrease in the ultrasound velocity occurs. Possible mechanisms of the effect are discussed. *© 2000 MAIK "Nauka/Interperiodica".*

The most common type of loading structures, mechanisms, and machines during their exploitation is cyclic (alternating or more complex) loading in which fatigue phenomena are developed. This type of loading is characteristic of aviation and rocket engineering, various types of engines, transport, and other engineering branches. A sudden (in most cases) occurrence of the final stage of fatigue failure may lead to hardly predicted severe (catastrophic) consequences.

The problem of the fatigue failure of metals and alloys, in spite of its long history, remains topical. A vast body of experimental material accumulated to date emphasizes its complex nature rather than indicates ways to solve it. Numerous unclarities exist in both the explanation of the nature of damage upon fatigue loading and the diagnostics of fatigue. Recent works indicate the complex nature of the fatigue phenomenon related to self-organization, accumulation, and interaction of lattice defects during fatigue loading [1, 2].

In this work, the following purposes were set: based on a simple and reliable method (applicable for individual articles) of determining the stage at which low-cycle fatigue fracture is developed [3, 4], to suggest a technique of restoring article's resource with the help of a special-type treatment and apply it to a wide class of important structural materials; for enhancing understanding of the results obtained, to perform a metallographic examination of the problem of fatigue loading and reveal factors that ensure restoration of article's resource upon such treatment.

Low-cycle tests were performed by zero-to-bend-stress cycling on samples made of structural steels 40 and 40Kh, rail steel M76 (70KhGSA), stainless steel Kh18N10T, and a weld-joined composite consisting of high-speed steel R6M5 and steel 40Kh. In parallel with fatigue tests, the ultrasound velocity (USV) was measured using an ISP-12 structural transformation meter to an accuracy of 10^{-4}. The device works on a carrier frequency of 2.5 MHz and generates surface (Raleigh) elastic waves propagating at a velocity of V_R.

Experiments performed showed that the USV continuously decreases during fatigue tests and the dependence of the USV on the number of loading cycles has a three-stage nature.

Metallographic investigations of the material structure at various stages of the $\Delta V/V_R(N)$ curve revealed the following: (1) at the first and second stages of the decrease in the USV upon fatigue tests, no marked changes discernible in an optical microscope are revealed in the material structure; (2) at the beginning of the final stage, fatigue cracks are formed, which reach 0.015 mm in length and later serve as fracture sites; and (3) a one-to-one link exists between the crack initiation and the beginning of the falloff of the USV.

Thus, we may think that the sharp falloff of the USV during fatigue tests is related to the appearance of fatigue cracks and indicates the approach of the final stage of the process, i.e., the transition to brittle rupture and the failure of the sample or the article. This sign is informative for an individual sample and cautions against the beginning of failure to a certain degree of accuracy. The results obtained may be considered as the suggestion and substantiation of a new informative sign of fatigue failure of steels [5, 6].

Since measurements of the USV permit us to rather accurately predict the approach of a critical stage of failure, it is possible to prevent failure by timely using some restoring action on the material loaded. As a suitable action of this kind, treatment with electric current unipolar pulses of amplitude to 250 MA/m^2 and duration 100 ms can be used. It is known from numerous previous investigations (see, e.g., [7]) that such treatment leads to a marked plasticization of steels and alloys.

The experimental scheme was as follows. Samples after the transition to the final stage of a fatigue test were subjected to a series of electric pulses, after which the fatigue testing and USV measurements were continued. As a result of such treatment, the USV increased to the initial value and the number of cycles to failure increased as the tests were continued.

Table 1. Enhancement of steel resource by electrostimulation

Steel grade	Resource enhancement, %
40	35.7
40Kh (heat-treated)	20.1–20.9
M76 (70KhGSA)	26.3–29.3
Kh18N10T	22.9–24.3
Weld-joined 40Kh + R6M5 composite	13.4–15.2

Table 2. Variation of characteristics of the structural state of grade 40 steel after electrical treatment

	State prior to treatment	State after treatment
Cycles to failure *N*	2800 (2000 + 800)	3800 (2000 + 1800)
σ_1, MPa (body stresses)	296	235
σ_{11}, MPa (body stresses)	506	253
D, nm	333	196

Note: *D* is the size of coherent domains.

After reaching the critical state, the untreated samples withstood, as a rule, no more than 1000 cycles before they failed; after treating with electric pulses, they were able to withstand 2500–3000 cycles. Thus, an essential increase in the resource of the samples is observed (Table 1).

Microscopic investigations show that after treatment with current pulses dramatic changes occur in the structure of metal. Greatest changes are observed in the state of fatigue microcracks that had arisen at the beginning of the final stage of the process. A new structural component appears in these cracks, whose microstructure cannot be resolved by optical or scanning electron microscopy. As a rule, this component is located on that side of the crack that faces the plus sign of the pulse generator. However, cases were observed where the entire volume of the crack was filled by this structural component. This component represents a “white layer,” whose appearance was repeatedly noted previously in cases where the concentrated supply of external energy was used, e.g., upon friction or laser or plasma treatment. The development of the “white layer” was traced on specially “labeled” (using microindentation) fatigue cracks. In addition, a series of model experiments were performed using surface quenching cracks that arose upon water quenching of M76 rail steel samples. In this case, the microcracks of the length to 0.15 mm also were filled with “white layer” after treatment with electric current pulses [5]. Microhardness data (3000 MPa for the grade 40 steel and 10000 MPa for the M76 steel) suggest that the white layer consists of finely dispersed products of martensite decomposition. Electron microprobe analysis of grade 40 steel samples performed on a scanning electron microscope with a JSM-T200 microanalyzer (JEOL) indicates an enhanced content of some alloying elements (Mn, Si) in the white layer as compared to the matrix. The development of the white layer is thought to occur as follows. It is known that electric field lines are concentrated near the crack tips; this increases heat liberation, which can result in local melting in those sites during each current pulse. After the current is stopped, cooling of these regions occurs because of the rapid heat exchange with the solid material that surrounds the molten zone. The solidification front moving toward the microcrack rejects impurities that lower the melting temperature of iron toward the crack; as a result, the volumes to be solidified last, which lead to the formation of the white layer, prove to be enriched in these impurities. Upon further cooling, disperse products of austenite transformation with the above hardness appear. This effect leads to the lowering of the level of stress concentration near crack tips and, thus, retards the development of failure. In general, there occurs a lowering in the level of internal stresses of the first and second kinds (body and textural stresses) in the steel matrix deformed in fatigue tests, as well as in a decrease in the size of coherent domain revealed by X-ray diffraction scattering (Table 2).

Note a very large decrease in the textural stresses and the coherent domain size. Both these characteristics are related to the properties of the dislocation structure, and their behavior after current pulse treatment indicates the leveling off of the dislocation density over the bulk of metal, which, naturally, decreases the probability for cracks to nucleate. All these data indicate the facilitation of the course of relaxation processes during treatment with electric pulses [5–7].

The above regularities permitted us to suggest a method for restoring the fatigue resource applicable to critical steel details of machines and mechanisms. Such treatment can be performed, e.g., during technical servicing or repairing of equipment. To this end, data on the initial USV should be introduced preliminarily into the article certificate.

We traced the relation between the three-stage curve of the dependence of the USV on the number of loading cycles and the U-shaped curve of the intensity of breakdowns well-known in the theory of reliability [8]. We revealed that the three stages of the falloff of the USV correspond to the occurrence of three types of failure: premature failure due to bedding-in (first stage), random breakdowns (second stage), and wear-out failure (third stage). This explains the fundamental difference between the traditional methods of determining steel resource, based on a statistical analysis of testing data obtained on many samples, and the method suggested above, which permits one to determine the approach of a critical stage on individual samples or articles. This is important for the case of costly details of critical facilities, for which the accumulation of statistical data obtained in special tests is difficult. The transition to measuring and analyzing fatigue characteristics of individual items can result in an essential cheapening of control procedures and the enhancement of the reliability of engineering and technology [8].

REFERENCES

1. V. S. Ivanova and V. F. Terent'ev, *The Nature of Metal Fatigue* [in Russian] (Metallurgiya, Moscow, 1995).
2. V. S. Ivanova, *Synergetics, Strength, and Fracture of Metallic Materials* [in Russian] (Nauka, Moscow, 1992).
3. L. B. Zuev, V. Ya. Tsellermaer, and V. E. Gromov, Zh. Tekh. Fiz. **67** (9), 123 (1997) [Tech. Phys. **42**, 1094 (1997)].
4. V. M. Finkel', and Yu. I. Golovin, Dokl. Ross. Akad. Nauk **237** (2), 325 (1977).
5. L. B. Zuev, D. Z. Chirakadze, and O. V. Sosnin, Metallofiz. Noveĭshie Tekhnol. **19** (8), 80 (1997).
6. L. B. Zuev, O. V. Sosnin, and D. Z. Chirakadze, Zh. Prikl. Math. Theor. Fiz., No. 4, 32 (1998).
7. V. E. Gromov, L. B. Zuev, and É. V. Kozlov, *Electrically Stimulated Plasticity of Metals and Alloys* [in Russian] (Nedra, Moscow, 1997).
8. V. E. Gromov, D. Z. Chirakadze, and E. V. Semakin, Izv. Ross. Akad. Nauk, Ser. Fiz., No. 5, 1019 (1997).

Translated by S.N. Gorin

Technical Physics, Vol. 45, No. 3, 2000, pp. 312–315. Translated from Zhurnal Tekhnicheskoĭ Fiziki, Vol. 70, No. 3, 2000, pp. 27–30.
Original Russian Text Copyright © 2000 by Klenin, Sushko, Dumpis, Poznyakova, Piotrovskiĭ.

OPTICS, QUANTUM ELECTRONICS

Light Scattering in Aqueous Solutions of Fullerene-Containing Polymers

S. I. Klenin*, M. L. Sushko*, M. A. Dumpis, L. I. Poznyakova**, and L. B. Piotrovskiĭ****
* *Institute of Macromolecular Compounds, Russian Academy of Sciences, St. Petersburg, 199004 Russia*
** *Institute of Experimental Medicine, Russian Academy of Sciences, St. Petersburg, 197376 Russia*

Received October 15, 1998; in final form, April 7, 1999

Abstract—Some properties of the aqueous solutions of polymer–fullerene complexes were studied. The experimental data suggest that fullerenes are capable of strong intermolecular interactions. *© 2000 MAIK “Nauka/Interperiodica”.*

INTRODUCTION

The properties and functionality of fullerenes have been studied in sufficient detail, and now there is increasing interest in the biological activity of fullerene (C_{60}) and its derivatives [1–5]. Unfortunately, the biological applications of fullerene are hindered by the fact that this compound is insoluble in water. A possible way to solving this problem is related to the formation of complexes between hydrophilic polymers and fullerene, which allows aqueous solutions of C_{60} to be obtained where the structure of fullerene molecules remains intact. However, C_{60} covalently bonded to a water-soluble polymer (starlike configuration) exhibits a significant decrease in biological activity [6–8]. Another necessary prerequisite for biological applications of fullerene–polymer complexes is the establishing of criteria for monitoring the composition and stability of these complexes. This task is inseparable from the general fundamental problem of determining the structure of fullerene-containing polymers in aqueous solutions. No clear notions of this structure has been yet formulated.

Below we report on the results of investigation into the properties of dilute aqueous solutions of poly(vinyl pyrrolidone)-fullerene (PVP–C_{60}) complexes and the base polymer (PVP) by methods of Rayleigh light scattering, translational diffusion, viscometry, and UV spectroscopy.

EXPERIMENTAL

The PVP–C_{60} complexes were prepared from PVP with $M = 35000 \pm 10\%$ using a modification of the method described in [9]. In particular, we used a benzene solution of C_{60} (instead of the toluene solution) which allowed the complex to be purified under comparatively mild conditions. We have synthesized the PVP–C_{60} complexes with various relative contents of fullerene (0.31–0.81%). The content of C_{60} in a complex was determined spectrophotometrically: the optical densities of fullerene- containing solutions with a C_{60} concentration from 0.31 to 0.81% obey the Lambert–Beer law. We failed to obtain the PVP–C_{60} complexes with a C_{60} content exceeding 0.81%.

In order to elucidate the structure of the fullerene-containing polymer in aqueous solution, we have compared solutions of the base polymer (PVP with $M = 10^4 \pm 10\%$) and a PVP–C_{60} complex with the component ratio 99.2:0.8. When the initial concentration of this complex in solution is $\sim 3 \times 10^{-3}$ g/cm^2, the content of C_{60} in the same solution does not exceed $\sim 3 \times 10^{-5}$ g/cm^3.

RESULTS AND DISCUSSION

Figure 1 (curve *1*) shows the plot of $(cH/I)_{90}$ versus PVP concentration c (H is the optical constant and I is the light scattering intensity increment). As seen, the cH/I ratio monotonically increases with the PVP concentration. Extrapolated value of the molecular mass $M_w = 1.1 \times 10^4$ agrees with the value obtained from analysis of the sedimentation-diffusion data ($M_{sd} = 1.0 \times 10^4$).

The concentration dependence of the inverse intensity of scattering for solutions of the PVP–C_{60} complex (Fig. 1, curve *2*) exhibits an anomalous character comprising two different parts. In the region of $c > c^* = 1.4 \times 10^{-3}$ g/cm^3, the I value does not virtually change with dilution. We may suggest that the light is scattered from certain continuum (the extrapolation to $c \longrightarrow 0$ yields $M \longrightarrow \infty$). The second region corresponds to $c < c^*$, where the extrapolation to $c \longrightarrow 0$ yields a finite value of $M_w = 5 \times 10^6$ (nevertheless exceeding the M_w of PVP by 2.5 orders of magnitude).

We may suggest that the complex concentrations exceeding c^* give rise to anomalously strong intermolecular interactions hindering the fluctuational motions

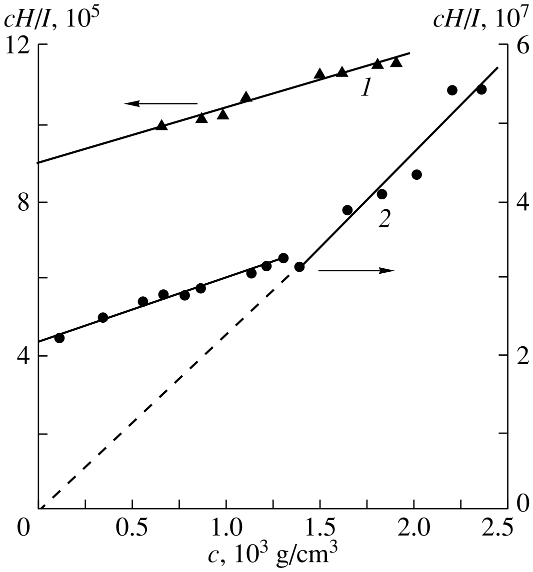

Fig. 1. The plots of $(cH/I)_{90}$ versus concentration *c* for aqueous solutions of (*1*) PVP and (*2*) a PVP–C_{60} complex.

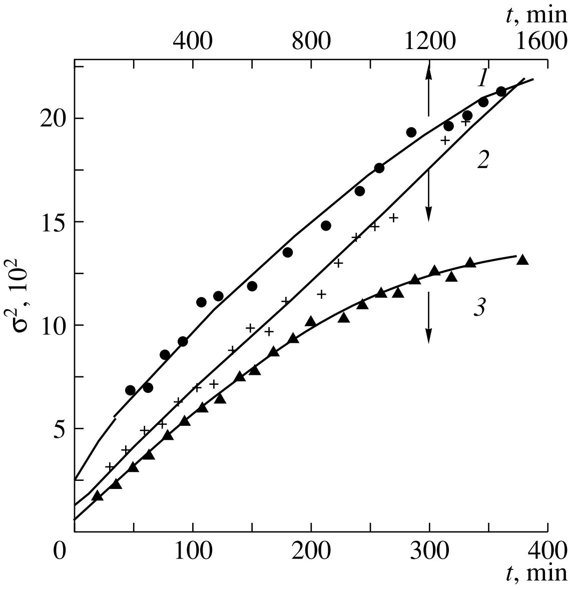

Fig. 2. The plots of $\sigma^2 = 2Dt$ versus time for (*1*) the self-diffusion in a PVP–C_{60} solution and for (*2*, *3*) the diffusion of PEO ($M = 1000$) in (*2*) PVP and (*3*) PVP–C_{60} complex solutions.

of molecules in solution. Apparently, the regions with retarded fluctuational mobility may form already at a concentration of the order of 10^{-4} g/cm^3. The value of $M_w = 5 \times 10^6$ probably corresponds to these very fragments of continuum, whereas the molecular mass determined by an alternative absolute method, the sedimentation-diffusion data analysis, coincides, to within the experimental error, with the molecular mass of PVP.

It should be noted that a change in the degree of solution structurization with dilution is thermodynamically unfavorable: the second virial coefficient of the solution in this range of $A_2 = 0.4 \times 10^{-4}$ mol cm^3/g^2. We believe that the probability of association in dilute solutions of the PVP–C_{60} complexes is extremely small, which is confirmed by the asymmetry of scattering characterizing the size (radius of gyration) of the associates coincides with the asymmetry of scattering observed in pure PVP solutions.

The appearance of a long-range order in dilute polymer solutions was reported [10] for the solutions of polyamic acids and polyimides in amide solvents. However, the ordering in these systems was fully destroyed at a solution concentration of 4.0–5.0 × 10^{-3} g/cm^3, which corresponds to a distance of about 300 Å (i.e., a monolayer of solvent molecules) between the centers of interacting macromolecules. In the solutions of PVP–C_{60} complexes studied, the continuum already appears at a concentration of 1.4×10^{-3} g/cm^3. This corresponds to a fullerene concentration of 1.4×10^{-5} g/cm^3 and a distance of about 2000 Å between the C_{60} molecules. Moreover, the continuum is not fully destroyed with decreasing concentration. We suggest that the interaction of fullerene molecules is mediated by structurized solvent.

The presence of the regions of hindered fluctuational mobility in PVP–C_{60} complex solutions was confirmed by data on the temperature variation of the light scattering intensity. The measurements were performed at a complex concentration of 2.5×10^{-4} g/cm^3. It was found that the plot of scattering intensity I_{90} versus tem-

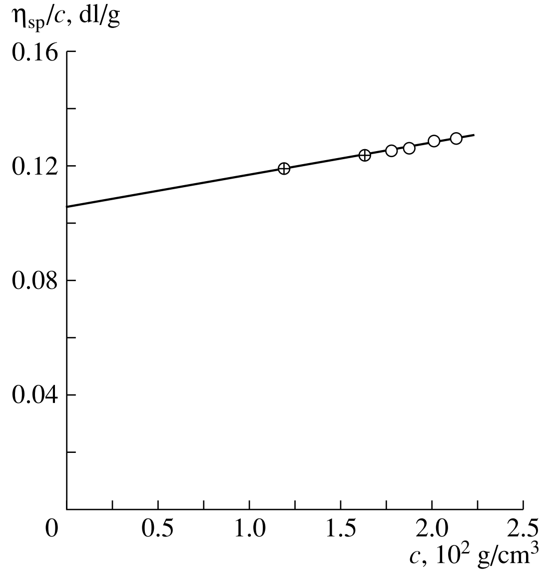

Fig. 3. The plot of reduced viscosity η_{sp}/c versus concentration for (o) PVP and (+) PVP–C_{60} complex solutions.

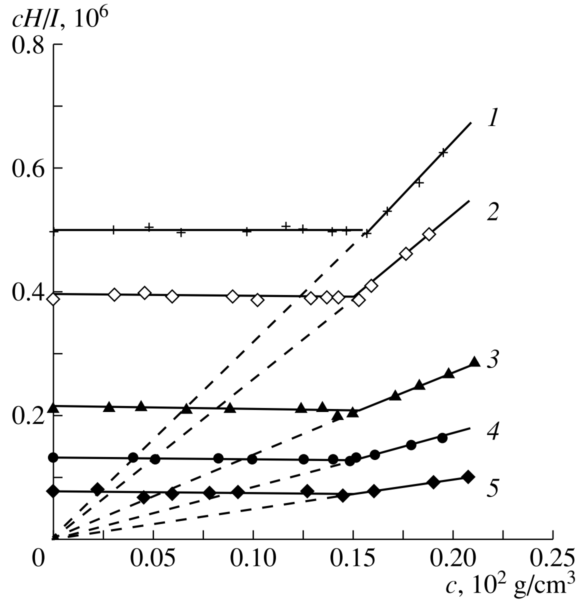

Fig. 4. The plots of $(cH/I)_{90}$ versus concentration *c* for aqueous solutions of PVP–C_{60} complexes with various fullerene content (%): (*1*) 0.31; (*2*) 0.48; (*3*) 0.64; (*4*) 0.67; and (*5*) 0.81.

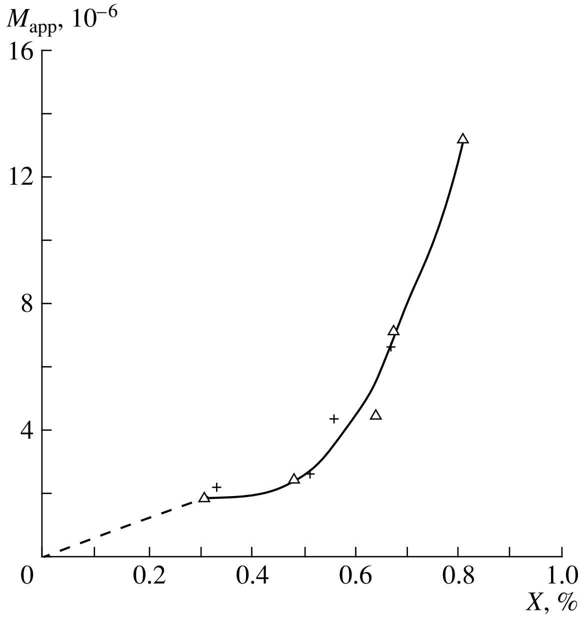

Fig. 5. The plot of M_{app} for the continuum fragments in aqueous solutions versus fullerene content *X* of PVP–C_{60} complexes.

perature is linear in the interval from 19 to 45°C, where the I_{90} value drops from 25.0×10^{-3} to 20.4×10^{-3}. This change may be related to a partial disturbance of structurization in the PVP–C_{60} complex solution as a result of increasing kinetic energy of the Brownian motion of both solvent and solute molecules. Note that the asymmetry of scattering in the complex solutions is independent of the temperature. This fact indicates that the decrease in I_{90} on heating cannot be related to the decay of molecular associates.

Strong intermolecular interactions in the system studied were also revealed by experiments on the translational diffusion of PVP– C_{60} complexes at very small values of the chemical potential gradient. The plot of the diffusion curve dispersion versus time (Fig. 2, curve *1*) is linear in the initial stage and deviates from linearity when the chemical potential gradient decreases. A decrease in the diffusion coefficient with decreasing chemical potential gradient can be related to the appearance of domains with hindered fluctuational mobility of molecules in solution, which diffuse as a whole. The assumption concerning the presence of solution domains featuring an ordered, rather than polydisperse, structure of complexes, is confirmed by data on the diffusion of poly(ethylene oxide) (PEO) molecules with $M = 1000$ in the solutions of PVP–C_{60} complexes and pure PVP (Fig. 2, curves *2, 3*). As seen from these data, the diffusion of PEO molecules in the complex solution (curve *3*) is strongly retarded as compared to the process in a PVP solution of the same concentration (curve *2*). Indeed, the diffusion coefficient of PEO in the former solution initially amounts to 1.85×10^{-6} cm^2/s and drops with decreasing driving force of the process, whereas the diffusion coefficient in the PVP solution is retained on a constant level of 2.1×10^{-6} cm^2/s.

Application of an additional gradient of the order of 700 s^{-1} led to complete breakage of the order in PVP–C_{60} complex solutions. This is illustrated by comparative viscometric data for the PVP–C_{60} complex and pure PVP solutions presented in Fig. 3. As seen from this plot, the complex and base polymer solutions with equal concentrations exhibit exactly the same values of reduced viscosity. The value of $M_\eta = 1.0 \times 10^4$ calculated from the corresponding value of the intrinsic viscosity using the Mark–Kuhn–Houwink formula [11] coincides with M_{sd}.

Study of the aqueous solutions of PVP–C_{60} complexes with the polymer mass $M = 3.5 \times 10^4$ and various C_{60} contents by the method of Rayleigh light scattering showed that the plots of inverse scattering intensity versus concentration are similar to that presented in Fig. 1 (curve *2*). The molecular mass of continuum fragments exhibited a monotonic increase with the content of fullerene in the complex (Figs. 4, 5). The critical concentration c^* somewhat decreased with increasing fullerene content in the complex (Fig. 4). This implies that the continuum is not fully destroyed even at rather small complex concentrations and breaks into separate coarse fragments with further dilution. Note that the values of the apparent molecular mass M_{app} coincide (to within an experimental error of ~10%) for all pairs of solutions of the same complex prepared by two different methods (Fig. 5).

CONCLUSION

The solutions of fullerene-containing polymers possess an ordered concentration-dependent structure. This is probably related to the ability of fullerene to form strong intermolecular contacts due to the presence of a large number of conjugated bonds in the C_{60} molecules. The values of molecular mass obtained from the light scattering data or the ordered domains in highly dilute solutions of fullerene-containing polymers may serve as a parameter for monitoring the content of fullerene in various compositions.

ACKNOWLEDGMENTS

This work was supported by the Russian Scientific and Technical Program “Orgent Issues in Physics of Condensed Matter. Fullerenes and Atomic Clusters.”

REFERENCES

1. V. P. Belousov, I. M. Belousova, V. P. Budtov, *et al.*, Opt. Zh. **64** (12), 3 (1997).
2. A. V. Eletskiĭ, Teplofiz. Vys. Temp. **34**, 308 (1996).
3. S. H. Friedman, D. L. DeCamp, R. P. Sijbesma, *et al.*, J. Am. Chem. Soc. **115**, 6506 (1993).
4. T. Tsuchiya, I. Oguri, Y.N. Yamakoshi, and N. Miyata, Fullerene Sci. Technol. **4**, 989 (1996).
5. L. L. Dugan, D. M. Turetsky, G. C. Du, *et al.*, Proc. Natl. Acad. Sci. USA **94**, 9434 (1997).
6. V. N. Zgonnik, L. V. Vinogradova, E. Yu. Melenevskaya, *et al.*, Zh. Prikl. Khim. **70**, 1159 (1997).
7. V. N. Zgonnik, L. V. Vinogradova, E. Yu. Melenevskaya, *et al.*, Zh. Prikl. Khim. **70**, 1538 (1997).
8. E. Yu. Melenevskaya, L. V. Vinogradova, L. S. Litvinova, *et al.*, Vysokomol. Soedin., Ser. A **40**, 1 (1998).
9. Y. N. Yamakoshi, T. Yagami, K. Fukuhara, *et al.*, J. Chem. Soc., Chem. Commun. p. 517 (1994).
10. N. V. D’yakonova, N. V. Mikhaĭlova, V. P. Sklizkova, *et al.,* Vysokomol. Soedin., Ser. A **28**, 2382 (1986).
11. G. D. Levy and H. P. Frank, J. Polym. Sci. **17**, 247 (1955).

Translated by Pavel P. Pozdeev

Technical Physics, Vol. 45, No. 3, 2000, pp. 316–317. Translated from Zhurnal Tekhnicheskoĭ Fiziki, Vol. 70, No. 3, 2000, pp. 31–33.
Original Russian Text Copyright © 2000 by Petrakov.

OPTICS, QUANTUM ELECTRONICS

Structural Studies of Disperse Crude-Oil Systems by Small-Angle X-ray Scattering Subjected to Millisecond Laser Pulses

A. P. Petrakov
Syktyvkar State University, Syktyvkar, 167001 Komi Republic, Russia

Received October 30, 1998

Abstract—The core size of complex structural units (CSUs) in paraffin crude oil was found by small-angle X-ray scattering. A variation of the core size with the energy and the number of millisecond pulses from a ruby laser was investigated. © *2000 MAIK “Nauka/Interperiodica”.*

INTRODUCTION

Investigations into the effects of physical actions on the structure and properties of crude oil are vital for developing technologies of fine oil refining and viscosity breaking, which makes easier oil production and transportation. As of now, ultrasonic methods are applied to prevent the deposition of salts and paraffins in boreholes and pipelines [1]. Also, oil properties are expected to change when oil is exposed to laser pulses, widely used for the modifying the structure of different materials [2–4]. Laser radiation stimulates chemical reactions [5, 6] and, in view of severe conditions, inherent in pulse irradiation, may result in a change in the CSU size in disperse oil systems.

Oil represents a disperse colloidal system consisting of CSUs. Each involves a core surrounded by a solvation shell. The core is formed of high-molecular alkanes, polyarene carbons, and resin asphaltens, while the solvation shell includes compounds less susceptible to intermolecular interaction [7].

Physical actions may change the CSU size [7], which is estimated with small-angle X-ray scattering by disperse systems [8]. The knowledge of the CSU size is necessary for oil fractionation upon refining, vitrification, and so on.

To improve the accuracy of the small-angle measurements, a triple-crystal X-ray diffractometer can be used [9–12]. This setup provides highly monochromatic radiation (after three-fold reflection, $K\alpha_1$ radiation alone comes out of a slit monochromator). The radiation is collimated in the horizontal plane (after three-fold reflection, the angular divergence of the output beam is below 9 seconds of arc).

The aim of this paper is to investigate a change in the size of oil CSUs exposed to millisecond pulses of a ruby laser. Measurements were performed by small-angle X-ray scattering with the use of a triple-crystal X-ray diffractometer.

EXPERIMENTAL

High-paraffin crude oil (the paraffin content was 32.1 wt %) was studied. A 1-mm-thick oil film was placed on a metal ring of inner diameter 3 cm. The film was exposed to the radiation of a free-running ruby laser. The pulse width was 0.5 ms; the energy density W = 11, 14, and 18 J/cm^2; the number of irradiations was 1–3; and the diameter of the laser beam on the film plane was 1 cm. The laser beam was incident on the film surface at a right angle.

The CSU size was measured with a triple-crystal X-ray diffractometer using Cu$K\alpha_1$ radiation. An oil film was placed behind the monochromator normally to the X-ray beam. The angular distribution of scattered intensity was recorded with a crystal analyzer, followed by a wide-slit detector. A silicon single crystal with three-fold (111) reflections was used as a slit monochromator. Silicon served also as a crystal analyzer, but here only one (111) reflection was used.

RESULTS AND DISCUSSION

The intensity of X-rays scattered from a disperse system is given by the Guinier formula

$$I(s) = I_0\exp(-s^2r_g^2/3),$$

where I_0 is the scattered intensity at $\Theta = 0$, $s = (4\pi/\lambda)\sin(\Theta/2)$, λ is the wavelength, Θ is a scattering angle, and r_g is the radius of gyration of a particle about the center of mass of the disperse system.

The radius of gyration is related to the characteristic size r of particles. For scattering by spherical particles, this relation has the form $r_g^2 = 3r^2/5$ [9].

The dependence of $\ln I(s)$ on s^2 (Guinier's plot) is presented in the figure. For nonirradiated oil, data points fall on two straight lines with slopes of 176.24 and 13.51. After exposure to a radiation with an energy density of 11 J/cm^2, the logarithm of the intensity drops to the background and level is represented by a straight

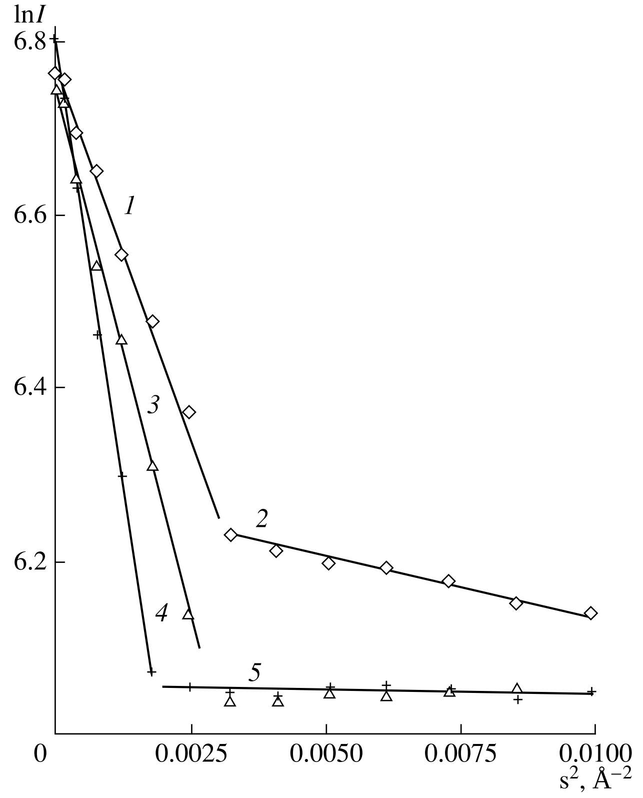

Guinier plots for small-angle scattering of X-rays by the disperse oil system: (*1*), (*2*) nonirradiated; (*3*) after a single irradiation at $W = 11$ J/cm^2; (*4*) after two-fold irradiation; and (*5*) background level.

line with a slope of 246.38. The second irradiation with the same energy results in a faster decline in the intensity (with a slope of 416.77). After the third irradiation, data points practically agree with those after the second one.

In the case of the sample irradiated with the specific energy of 14 J/cm^2, the scattered intensity shows the same behavior. When the energy density rises to 18 J/cm^2, data points even after the first irradiation coincide with those after the second irradiation at $W = 11$ J/cm^2.

The size of scattering particles can be found from the slopes of the curves with an accuracy of 5%. From the formulas above, $r = (5\tan\alpha)^{1/2}$ for spherical particles. Small-angle X-ray scattering makes it possible to determine the size of the ordered CSU region that is, its core [7]. Hence, the CSU cores in as-produced oil are 30 and 8 Å across. The presence of the cores greatly differing in sizes means that crude oil represents a polydisperse system consisting of primary CSUs of two sizes. Polydispersity is characteristic of produced oils [7].

During laser irradiation at $W = 11$ J/cm^2, oil passes to the monodisperse state, and secondary CSUs with the cores 35 Å across are formed. The cores grow through coalescing primary CSUs. This conclusion is supported by the investigation of thermal, mechanical, electromagnetic, and other effects on the structure of disperse oil systems [8].

Repeat irradiation with the same energy results in further growth of the specific core size to 46 Å, suggesting that secondary CSUs have merged together. Subsequent irradiations leave the size CSU cores unchanged.

A similar change in the core size was observed at $W = 14$ J/cm^2. After the first irradiation at $W = 18$ J/cm^2, the core size becomes equal to the one after two-fold irradiation at $W = 11$ or 14 J/cm^2. After the second irradiation at $W = 18$ J/cm^2, the core size remains the same. This means that this parameter is limited from above.

To conclude, small-angle X-ray scattering with the use of a triple-crystal X-ray diffractometer makes it possible to determine the size of CSU cores in disperse oil systems. Millisecond pulses from a ruby laser convert polydisperse high-paraffin systems into monodisperse, and the size of CSU cores grows. As the number of irradiations and pulse energy increase, so does the core size but to a certain limit.

REFERENCES

1. O. A. Kuznetsov and S. A. Efimov, *Ultrasonics in the Oil Industry* (Nedra, Moscow, 1983).
2. J. F. Ready, *Effects of High-Power Laser Radiation* (Academic, New York, 1971; Mir, Moscow, 1974).
3. V. A. Bushuev and A. P. Petrakov, Fiz. Tverd. Tela (St. Petersburg) **35**, 355 (1993) [Phys. Solid State **35**, 181 (1993)].
4. A. P. Petrakov and E. A. Golubev, Fiz. Tverd. Tela (St. Petersburg) **40**, 156 (1998) [Phys. Solid State **40**, 140 (1998)].
5. F. V. Bunkin, N. A. Kirichenko, and B. S. Luk'yanchuk, Izv. Akad. Nauk SSSR, Ser. Fiz. **45**, 1018 (1981).
6. M. A. Liberman and M. I. Tribel'skiĭ, Zh. Éksp. Teor. Fiz. **74**, 194 (1978) [Sov. Phys. JETP **47**, 99 (1978)].
7. Z. I. Syunyaev, R. Z. Syunyaev, and R. Z. Safieva, *Disperse Oil Systems* (Khimiya, Moscow, 1990).
8. D. I. Svergun and L. A. Feĭgin, *Small-Angle Scattering of X-rays and Neutrons* (Nauka, Moscow, 1986).
9. A. M. Afanas'eva, P. A. Aleksandrov, and R. M. Imamov, *X-ray Diffraction Analysis of Submicron Layers* (Nauka, Moscow, 1989).
10. A. Iida and K. Dohra, Phys. Status Solidi A **51**, 533 (1979).
11. V. V. Ratnikov and R. N. Kyutt, Zh. Tekh. Fiz. **55**, 391 (1985) [Sov. Phys. Tech. Phys. **30**, 229 (1985)].
12. V. A. Bushuev and A. P. Petrakov, Kristallografiya **40**, 1043 (1995) [Crystallography Reports **40**, 968 (1995)].

Translated by B. Malyukov

Technical Physics, Vol. 45, No. 3, 2000, pp. 318–321. Translated from Zhurnal Tekhnicheskoĭ Fiziki, Vol. 70, No. 3, 2000, pp. 34–36.
Original Russian Text Copyright © 2000 by Gudkov.

OPTICS, QUANTUM ELECTRONICS

On Frequency and Temperature Dependence of Limiting Efficiency in Direct Utilization of Quasi-Monochromatic Radiation

N. D. Gudkov

Institute of Fundamental Problems of Biology, Russian Academy of Sciences, Pushchino,
Moscow oblast, 142292 Russia

Received December 31, 1998

Abstract—The solution to the problem on limiting (thermodynamically permissible) efficiency η_m of direct conversion of energy of quasi-monochromatic radiation into work known from the literature leads to physically unacceptable results ($\eta_m < 0$) in the range of small frequencies ν and temperatures T_ν of converted radiation. It is shown that the noted feature is a consequence of the approximate character of the mentioned solution obtained without taking into account background heat radiation: the exact solution obtained for η_m is valid for all ν and $T_\nu \geq 0$ and turns into the solution known earlier for $T_\nu \gg T$ and $h\nu \gtrsim kT$ (where T is the temperature of the surroundings). *© 2000 MAIK “Nauka/Interperiodica”.*

In [1], the following result for the limiting efficiency of “direct” conversion of energy of quasi-monochromatic radiation into work in the case of total absorption of incident radiation by a “working medium” was obtained:

$$\eta_m \overset{\text{def}}{=} \frac{N_m}{\Pi_{rs}^{\text{in}}} = 1-\alpha\frac{T}{T_\nu}+(\alpha-1)\ln(\alpha-1)\frac{kT}{h\nu}, \qquad \alpha = e^{h\nu/kT_\nu}. \tag{1}$$

Here, N_m is the maximum (thermodynamically permissible) value of the converter output power, Π_{rs}^{in} is the flux, ν is the frequency, T_ν is the temperature of radiation incident to a converter, T is the temperature of both the surroundings and converter, and k and h are Boltzmann’s and Planck’s constants, respectively.[1]

In limiting cases of small and large frequencies, formula (1) gives [1]

$$\eta_m = \begin{cases} 1-\dfrac{T}{T_\nu}-\dfrac{kT}{h\nu}, & h\nu \gg kT_\nu \\[2ex] 1-\dfrac{T}{T_\nu}\left(1+\ln\dfrac{kT_\nu}{h\nu}\right), & h\nu \ll kT_\nu. \end{cases} \tag{2}$$

Obviously, the smaller the ratio $h\nu/kT_\nu$, the more accurate the latter formula of (2) (in comparison with the initial formula (1)). However, the paradox lies in the fact that this formula implies physically unacceptable result $\eta_m < 0$ at sufficiently small values of the mentioned ratio, with $\eta_m \longrightarrow -\infty$ as $\nu \longrightarrow 0$. If the temperature of converted radiation is decreasing at a given value of ν, the “high-frequency” (upper) formula of (2) leads to the same result.

As a rule, a “paradox” similar to the noted ones occurs when an approximate formula considered to be exact is used beyond its validity region. In this paper, it is shown that the example under consideration is not an exception; consequently, expression (1) obtained without taking account of background heat radiation is of approximate character and valid when the two following conditions are met simultaneously: $T_\nu \gg T$ and $h\nu \gtrsim kT$. It is easy to see that formula (1) leads to physically meaningless values of η_m when just these conditions are violated.[2]

1. Thermodynamics requirements imply the following upper bound on the output power N of an arbitrary device performing work on external bodies under conditions of stationary energy exchange with both thermostat (“the surroundings”) and radiation field [2]:

$$N \leq \Pi_r - T\Sigma_r = N_m. \tag{3}$$

Here Π_r and Σ_r are the net fluxes of energy and entropy

---

[1] The factor α in the second addend of the given expression is missing in cited formula (12) in [1] due to an obvious misprint.

[2] It is appropriate to mention here that the appearance of this paper was provoked to a certain extent by papers [3], whose author, using formula (1) beyond its validity region, obtains a number of interesting results, among which are “one more thermodynamic method for deriving the law of thermal radiation” or, e.g., a conclusion (of fundamental importance) on the existence of “principal thermodynamic restriction on endoergic reactions” (radiation energy with such a frequency and radiance that $\eta_m < 0$ “can in no way be converted into the free energy of matter.”

of radiation absorbed by the device ("converter") through its surface:

$$\Pi_r = -\int d\nu \int d\sigma \int\limits_{\mathbf{n}\boldsymbol{\omega} \gtrless 0} d\Omega_{\boldsymbol{\omega}} \mathbf{n}\boldsymbol{\omega} K_\nu, \qquad (4)$$

$$\Sigma_r = -\int d\nu \int d\sigma \int\limits_{\mathbf{n}\boldsymbol{\omega} \gtrless 0} d\Omega_{\boldsymbol{\omega}} \mathbf{n}\boldsymbol{\omega} L_\nu, \qquad (5)$$

where $K_\nu = (K_\nu(\mathbf{r}, \boldsymbol{\omega}))$ is the spectral energy radiance of radiation with frequency ν propagating in an element of solid angle $d\Omega_{\boldsymbol{\omega}}$ in the direction of a unit vector $\boldsymbol{\omega}$ and crossing an element $d\sigma$ of the converter surface (with an external normal $\mathbf{n}$) at a point $\mathbf{r}$; L_ν is the spectral entropy radiance of radiation, which (if radiation is not polarized) is uniquely defined by the quantities ν and K_ν [4]

$$L_\nu = L_\nu(K_\nu) = \frac{2k\nu^2}{c^2}[(1+n_\nu)\ln(1+n_\nu) - n_\nu \ln n_\nu], \qquad (6)$$

where c is the speed of light, n_ν is the average number of quanta at a field oscillator,

$$n_\nu = c^2 K_\nu / 2h\nu^3. \qquad (7)$$

2. The spectral radiance of radiation on the converter surface, which solely determines the limiting converter power N_m, as is seen from the formulas cited above, is represented as the sum

$$K_\nu = \begin{cases} K_\nu^{\text{in}} + K_\nu^T, & \mathbf{n}\boldsymbol{\omega} \le 0 \\ K_\nu^{\text{out}} + K_\nu^T, & \mathbf{n}\boldsymbol{\omega} > 0. \end{cases} \qquad (8)$$

The radiance of incident radiation from an external source is denoted here by K_ν^{in}; K_ν^{out} refers to nonequilibrium radiation emitted from the converter surface; and K_ν^T denotes the radiance of background heat radiation in which the considered system (together with the surroundings) is necessarily immersed and which should apparently be considered as the black light of temperature T

$$K_\nu^T = \frac{2h\nu^3}{c^2}\frac{1}{[\exp(h\nu/kT) - 1]}. \qquad (9)$$

Assume that the converter absorbs the incident radiation completely and does not luminesce; i.e., we take $K_\nu^{\text{out}} = 0$. In this case, taking into account (6)–(9), expressions (4) and (5) take the form

$$\Pi_r = -\int d\nu \int d\sigma \int\limits_{\mathbf{n}\boldsymbol{\omega} \le 0} d\Omega_{\boldsymbol{\omega}} \mathbf{n}\boldsymbol{\omega} K_\nu^{\text{in}} = \Pi_{rs}^{\text{in}}, \qquad (4')$$

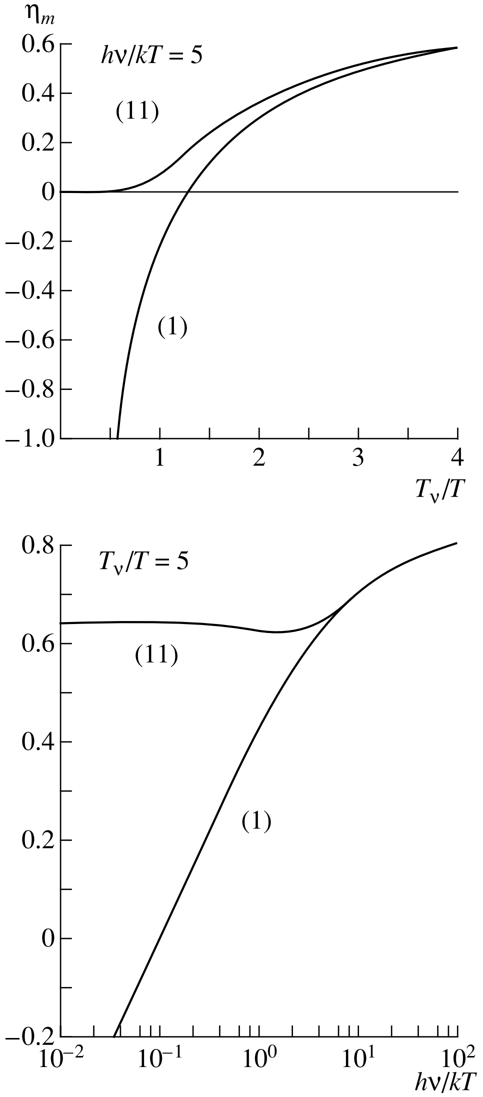

Dependences of the limiting efficiency on the temperature and frequency of converted radiation determined by formulas (1) and (11), respectively.

$$\Sigma_r = -\int d\nu \int d\sigma \int\limits_{\mathbf{n}\boldsymbol{\omega} \le 0} d\Omega_{\boldsymbol{\omega}} \mathbf{n}\boldsymbol{\omega} [L_\nu(K_\nu^{\text{in}} + K_\nu^T) - L_\nu(K_\nu^T)]. \qquad (5')$$

Furthermore, we assume that the incident radiation is isotropic within the solid angle of its propagation (as it generally occurs in practice).[3] It is easy to verify that integration with respect to $d\sigma$ and $d\Omega_{\boldsymbol{\omega}}$ in formulas (4'), (5') is performed independently of integration with

---

[3] Formally, this assumption means that $K_\nu^{\text{in}}(\mathbf{r}, \boldsymbol{\omega})$ can be presented in the form $K_\nu^{\text{in}} = a(\mathbf{r}, \boldsymbol{\omega})K(\nu)$, where $a(\mathbf{r}, \boldsymbol{\omega}) = 1$ if $(\mathbf{r}, \boldsymbol{\omega}) \in G$ and $a = 0$ if $\mathbf{r}$ and $\boldsymbol{\omega}$ do not belong to a certain region G of a five-dimensional space.

respect to $d\nu$, and, consequently,

$$\Pi_{rs}^{\text{in}} = \Gamma\int d\nu K_{\nu}^{\text{in}}, \tag{4''}$$

$$\Sigma_r = \Gamma\int d\nu[L_{\nu}(K_{\nu}^{\text{in}} + K_{\nu}^{T}) - L_{\nu}(K_{\nu}^{T})], \tag{5''}$$

where the factor Γ signifies the "geometric quotient."

After substituting (4") and (5") into (3) and dividing the obtained expression for N_m by the power Π_{rs}^{in} of the incident radiation (formula (4")), we find that the limiting efficiency in the case of quasi-monochromatic radiation is determined by the equation

$$\eta_m = 1 - T[L_{\nu}(K_{\nu}^{\text{in}} + K_{\nu}^{T}) - L_{\nu}(K_{\nu}^{T})]/K_{\nu}^{\text{in}}, \tag{10}$$

or, taking into account (6), (7), and (9),

$$\eta_m = 1 - \frac{1}{n_{\nu}^{\text{in}}}\frac{kT}{h\nu}[f(n_{\nu}^{\text{in}} + n_{\nu}^{T}) - f(n_{\nu}^{T})], \tag{11}$$

where

$$f(\xi) = (1+\xi)\ln(1+\xi) - \xi\ln\xi, \tag{12}$$

$$n_{\nu}^{T} = 1/[\exp(h\nu/kT) - 1], \tag{13}$$

and the temperature T_{ν} of converted radiation is introduced in the ordinary way,

$$n_{\nu}^{\text{in}} = c^2 K_{\nu}^{\text{in}}/2h\nu^3 = 1/[\exp(h\nu/kT_{\nu}) - 1]. \tag{14}$$

Expression (11) is the aim of preceding calculations and the paper as a whole. A simple, but cumbersome, analysis shows that formula (11), in contrast to (1), does not contain any singularity and leads to values $\eta_m \geq 0$ (note that $\eta_m \leq 1$) at arbitrary T, T_{ν}, and $\nu \geq 0$.[4]

The figure serves as an illustration of this statement. Besides that, it is seen from the figure that, at sufficiently large values of T_{ν} and ν, results (1) and (11) coincide. The validity conditions of approximation (1) are discussed in more detail in the Appendix.

APPENDIX

Suppose $T_{\nu} \ll T$. Then, as is seen from (13) and (14),

$$n_{\nu}^{\text{in}} \gg n_{\nu}^{T} \tag{15}$$

for any given frequency value (in particular, $n_{\nu}^{\text{in}}/n_{\nu}^{T} \longrightarrow T_{\nu}/T$ for $\nu \longrightarrow 0$). Note that the quantity n_{ν}^{T} itself is not necessarily small in comparison with unity. On the contrary, depending on frequency, n_{ν}^{T} may essentially exceed unity attaining arbitrary large values for $\nu \longrightarrow 0$. Nevertheless, we will show that, due to the monotonically increasing and "smooth" type of the function $f(\xi)$ at arbitrary value n_{ν}^{T}, the following approximation is valid:

$$f(n_{\nu}^{\text{in}} + n_{\nu}^{T}) = f(n_{\nu}^{\text{in}}). \tag{16}$$

The accuracy δ of the formula is of the order of $n_{\nu}^{T}/n_{\nu}^{\text{in}}$; i.e., $\delta \ll 1$ if assumption (15) is valid. Indeed, according to the Lagrange theorem on finite increment, for arbitrary n_{ν}^{in} and n_{ν}^{T}, we have

$$f(n_{\nu}^{\text{in}} + n_{\nu}^{T}) = f(n_{\nu}^{\text{in}}) + n_{\nu}^{T}\frac{df}{d\xi}\bigg|_{\xi = n_{\nu}^{\text{in}} + \theta n_{\nu}^{T}},$$

where $0 \leq \theta \leq 1$.

This implies the following estimate for the accuracy of substitution (16):

$$\delta \leq \delta_m = \frac{n_{\nu}^{T}}{f(n_{\nu}^{\text{in}})}\max_{\theta}\frac{df}{d\xi}.$$

Since $df/d\xi = \ln(1 + 1/\xi)$, the estimation peaks at the minimum possible value of ξ, i.e., at $\theta = 0$ if $\xi = n_{\nu}^{\text{in}} + \theta n_{\nu}^{T}$. Thus,

$$\delta_m = \frac{n_{\nu}^{T}}{f(n_{\nu}^{\text{in}})}\ln\left(1 + \frac{1}{n_{\nu}^{\text{in}}}\right)$$

or

$$\delta_m = \frac{n_{\nu}^{T}}{f(n_{\nu}^{T}/\beta)}\ln(1 + \beta/n_{\nu}^{T}), \tag{17}$$

where $\beta = n_{\nu}^{T}/n_{\nu}^{\text{in}}$.

Elementary analysis of function (17) shows that

$$\delta_m \leq \beta$$

at any $n_{\nu}^{T} \geq 0$, which was to be proved.

Thus,

$$\eta_m = 1 - \frac{1}{n_{h\nu}^{\text{in}}}\frac{kT}{h\nu}[f(n_{\nu}^{\text{in}}) - f(n_{\nu}^{T})] \tag{18}$$

for $T_{\nu} \gg T$.

Further simplification of formula (18) is reduced to substitution:

$$f(n_{\nu}^{\text{in}}) - f(n_{\nu}^{T}) = f(n_{\nu}^{\text{in}}). \tag{19}$$

On the face of it, validity of this substitution under condition (15) is obvious if one takes into account the monotonically increasing type of the function $f(\xi)$. However, for sufficiently large n_{ν}^{T} (and, hence, for n_{ν}^{in} also essentially exceeding unity according to (15)), the

---

[4] In particular, $\eta_m \longrightarrow 1 - (T/T_{\nu})\ln(1 + T_{\nu}/T)$ for $\nu \longrightarrow 0$, and $\eta_m \longrightarrow 0$ when $T_{\nu} \longrightarrow 0$, as it should be.

rate of increase of the function $f(\xi)$ is small and, hence, the error δ_1 arising from substitution (19) may become large for $n_\nu^T \gg 1$.

Indeed, dependence δ_1 on n_ν^T is given by the expression

$$\delta_1 = \frac{f(n_\nu^T)}{f(n_\nu^{\mathrm{in}})} = \frac{f(n_\nu^T)}{f(n_\nu^T/\beta)}.$$

Taking into account the explicit form of $f(\xi)$, it can be easily shown that, at $n_\nu^T \lesssim 1$ (i.e., at $h\nu \gtrsim kT$),

$$\delta_1\big|_{h\nu \gtrsim kT} \le \beta\big|_{T_\nu \gg T} \ll 1, \tag{20}$$

whereas, in the case of $n_\nu^T \gg 1$, the error $\delta_1 \sim 1$ and, hence, the substitution (19) is incorrect.

Equations (18)–(20) imply that, at $T_\nu \gg T$ and $h\nu \gtrsim kT$, the following approximation is valid:

$$\eta_m = 1 - \frac{1}{h_\nu^{\mathrm{in}}}\frac{kT}{h\nu}f(n_\nu^{\mathrm{in}}),$$

which agrees with formula (1) if evident algebraic transformations are made.

REFERENCES

1. M. A. Leontovich, Usp. Fiz. Nauk **114**, 555 (1974).
2. N. D. Gudkov, Zh. Tekh. Fiz. **51**, 1306 (1981).
3. Yu. P. Chukova, Dokl. Akad. Nauk SSSR **300**, 504 (1989); Biofizika **34**, 898 (1989); Zh. Fiz. Khim. **64**, 28 (1990); Dokl. Akad. Nauk SSSR **311**, 506 (1990).
4. M. Plank, *The Theory of Heat Radiation* (Dover Publications, New York, 1959).

Translated by M. S. Fofanov

Technical Physics, Vol. 45, No. 3, 2000, pp. 322–329. Translated from Zhurnal Tekhnicheskoĭ Fiziki, Vol. 70, No. 3, 2000, pp. 37–43.
Original Russian Text Copyright © 2000 by Sudakov.

ELECTRON AND ION BEAMS, ACCELERATORS

Spectrum of Charged Particle Oscillations in an RF Quadrupole Field

M. Yu. Sudakov

Ryazan State Pedagogical University, Ryazan, 390000 Russia

Received December 1, 1998

Abstract—Variations in the spectral composition of ion oscillations within several stability regions of a quadrupole mass filter were studied. The frequency spectrum was shown to consist of two line systems. Side lines $\omega_n = n\omega_0 \pm \beta\omega_0/2$ were observed in the oscillation spectrum near harmonics $n\omega_0$ ($n = 0, 1, 2, \ldots$), where ω_0 is the circular frequency of an RF field and β is the stability parameter. Near the boundaries of the stability regions, the oscillations took the form of beatings. For even values of the stability parameter, $\beta = 2k$ ($k = 1, 2, \ldots$), the beat frequency coincides with the fundamental frequency ω_0 and, for $\beta = 2k - 1$, the main beat frequencies are $\omega_0/2$ and $3\omega_0/2$. *© 2000 MAIK "Nauka/Interperiodica".*

INTRODUCTION

An ion trap and a quadrupole mass filter are based on dynamic trapping and confinement of charged particles in an alternating quadrupole electric field [1, 2]. These processes are described by the theory of parametric resonance. The theory is based on Mathieu and Hill equations, which describe the motion of charged particles in an alternating quadrupole field. The general features of the ion oscillation spectrum and its frequency composition are well known [3]. However, to analyze nonlinear oscillations of ions in multipole fields [4], investigate the process of resonance extraction of ions from the confinement region using a small external harmonic signal [5], and compare the ion motion characteristics in a number of stability regions of the Mathieu equation [6], the oscillation spectrum should be studied in more detail.

The goal of this work was to develop effective methods for calculating spectral characteristics of ion motion in alternating quadrupole fields with allowance for viscous friction, study the composition and structure of oscillations, and perform a comparative analysis of oscillations in a number of stability regions.

GENERAL SOLUTION TO MOTION EQUATIONS

A quadrupole electric field is defined as an electric field in which potential is a quadratic function of coordinates. In a mass filter, this condition is satisfied only for two coordinates, and, in an ion trap, for the three coordinates. The law of motion of a charged particle in an RF quadrupole field is described by the Hill equation [1]

$$\frac{d^2x}{dt^2} + 2\gamma\frac{dx}{dt} + \varepsilon\frac{eU(t)}{mr_0^2}x = 0, \tag{1}$$

where x is the particle coordinate, e/m is the specific charge, r_0 is the field radius, $U(t)$ is the periodic source voltage with the period T, and ε is the parameter depending on coordinates and the type of a device (for a mass filter, $\varepsilon_x = 1$ and $\varepsilon_y = -1$; for a three-dimensional ion trap, $\varepsilon_x - \varepsilon_y = 1$ and $\varepsilon_z = -2$). The damping term with the coefficient γ allows for the viscosity of a medium. In some cases, oscillation damping is of fundamental importance for the device operation. For example, the use of a light buffer gas in the Finigan MAT ion trap significantly improves the device characteristics [4]. Frequent collisions of massive charged particles with light molecules of the buffer gas can be interpreted as oscillation damping. Therefore, the motion of trapped particles can be described by equation (1).

Since the coefficients of equation (1) are periodic with the period T, it is sufficient to consider the solutions to equation (1) over one period. Let us suppose that two characteristic solutions, $y_1(t)$ and $y_2(t)$, satisfying the initial conditions $y_1(0) = 1$, $y_2(0) = 0$, $\dot{y}_1(0) = 1$, and $\dot{y}_2(0) = 0$ are determined (usually, by numerical integration) within the interval $0 < t < T$. We introduce the vector of generalized coordinates $X(t)$ and the matrix of characteristic solutions $Y(t)$,

$$X(t) = \begin{bmatrix} x(t) \\ \dot{x}(t) \end{bmatrix}, \quad Y(t) = \begin{bmatrix} y_1(t) & y_2(t) \\ \dot{y}_1(t) & \dot{y}_2(t) \end{bmatrix}. \tag{2}$$

Since equation (1) is linear, its solution can be expressed through the initial condition $X(0)$ as $X(t) =$

$Y(t)X(0)$. The periodicity of the coefficients of equation (1) yields $X(nT) = Y(T)X[(n-1)T] = Y^n(T)X(0)$. Hence, for $t = nT + \tau$ (where $0 < \tau < T$), the general solution can be written in the form

$$X(nT+\tau) = Y(\tau)L^n X(0), \tag{3}$$

where $L = Y(T)$ is the one-period transformation matrix.

Therefore, to find the coordinates, it is necessary to calculate the powers of the matrix L. This can be easily done if the eigenvectors and eigenvalues λ_k of the matrix L are known:

$$L^n X(0) = \sum_k c_k \lambda_k^n l_k, \tag{4}$$

where c_k are the coefficients of the expansion of the vector $X(0)$ in terms of the eigenvectors of the one-period transformation matrix. Equations (3) and (4) allow us to determine the time dependences of the solutions to an arbitrary equation with periodic coefficients. Here, we use them to solve the Hill equation with the damping term. In this case, the one-period transformation matrix is a 2 × 2 matrix. Its eigenvalues are determined from the quadratic characteristic equation

$$\lambda^2 - \lambda\,\mathrm{Spur}(L) + \mathrm{Det}(L) = 0, \tag{5}$$

where $\mathrm{Spur}(L)$ is the trace of matrix L and $\mathrm{Det}(L)$ is the matrix determinant. If the eigenvalues are complex conjugate and do not exceed unity in magnitude, the particle motion is limited and its trajectory is referred to as stable. One or both eigenvalues exceed unity in magnitude; therefore, the particle enters the region of parametric resonance and the coordinate and velocity of the particle increase without bound; such a trajectory is referred to as unstable.

Further analysis of the solutions to equation (1) can be carried out based on expressions (3) and (4). In order to determine the motion of a charged particle in a periodic quadrupole field, we should find the eigenvalues and eigenvectors of the one-period transformation matrix. By direct substitution, one can ascertain that, if $y_1(t)$ and $y_2(t)$ are solutions to equation (1), then $\mathrm{Det}(Y)$ satisfies the equation

$$\begin{gathered}\frac{d}{dt}\mathrm{Det}(Y) + 2\gamma\,\mathrm{Det}(Y) = 0 \\ \text{or } \mathrm{Det}Y(t) = \mathrm{Det}Y(0)\exp(-2\gamma t).\end{gathered} \tag{6}$$

Therefore, $\mathrm{Det}(L) = \mathrm{Det}(Y(T)) = \exp(-2\gamma T)$. For convenience, we introduce the matrix M defined by the equation

$$L = \exp(-\gamma T)\begin{bmatrix} m_{11} & m_{12} \\ m_{21} & m_{22} \end{bmatrix} = M\exp(-\gamma T) \tag{7}$$

so that $\mathrm{Det}(M) = 1$. The eigenvalues of the matrix L are $\lambda = \mu\exp(-\gamma T)$, where μ are the eigenvalues of the matrix M, which can be found from the equation

$$\mu^2 - \mathrm{Spur}(M)\mu + 1 = 0. \tag{8}$$

An analysis of the solutions to equation (8) shows that, if $|\mathrm{Spur}(M)| < 2$, the eigenvalues are complex conjugate, $\mu_1 = \mu_2^* = \exp(i\pi\beta)$. In this case, the ion motion, described by (4), has the form of finite nonperiodic oscillations that are characterized by number β, which is the fundamental parameter of the Hill equation. In the opposite case, when $|\mathrm{Spur}(M)| > 2$, we have $\mu_1 = 1/\mu_2 = \exp(\kappa)$; i.e., in the absence of damping, the motion is unstable. In the presence of damping, the motion remains unstable if $|\lambda| < 1$ or $\ln(\mu_1) < \gamma T$. Thus, the damping broadens the stability regions [7].

For stable oscillatory trajectories, the eigenvalues are $\lambda_1 = \lambda_2^* = \exp(-\gamma T + i\pi\beta)$ and the eigenvectors of the one-period transformation matrix are

$$m_1 = m_2^* = \begin{pmatrix} 1 \\ \dfrac{i-A}{B} \end{pmatrix}, \tag{9}$$

where A and B are the parameters of the trapping ellipses [1]

$$\begin{gathered} A = \frac{m_{11}-m_{22}}{\sin(\pi\beta)}, \quad B = \frac{m_{12}}{\sin(\pi\beta)}, \\ \cos(\pi\beta) = \frac{m_{11}+m_{12}}{2}. \end{gathered} \tag{10}$$

Note that the eigenvectors for matrices L and M coincide.

To find the general solution to equation (1), we consider its particular solution satisfying the initial conditions $u(0) = 1$ and $u'(0) = (i-A)/B$. In this case, the vector of the initial coordinates $X(0) = m_1$ coincides with the eigenvector of the one-period transformation matrix. According to equation (3), at the instant $t = nT + \tau$, this solution takes the form

$$\begin{aligned} u(t) &= \left(y_1(\tau) + \frac{i-A}{B}y_2(\tau)\right)\exp[(-\gamma T + i\pi\beta)n] \\ &= \phi(t)\exp[(i\Delta-\gamma)t], \end{aligned} \tag{11}$$

where $\Delta = \pi\beta T$ and $\phi(t)$ is the periodic function with the period T,

$$\phi(t) = \left(y_1(\tau) + \frac{i-A}{B}y_2(\tau)\right)\exp[(\gamma - i\Delta)\tau]. \tag{12}$$

The Floquet theorem [8] states that the Hill equation (1) has the solution of the form (11) if $\gamma = 0$. Hence, we will refer to the function $\phi(t)$ as the Floquet function. In (12), the Floquet function is expressed via two characteristic solutions to equation (1). Solution (11) can be used for constructing the general solution to the Hill equation. If the complex function $u(t)$ is the solution to a real equation, then the complex conjugate function $u^*(t)$ is the second linearly independent solution to the same equation. Thus, the general solution can be written as

$$x(t) = Cu(t) + C^*u^*(t) = [C\phi(t)\exp(i\Delta t) + C^*\phi^*(t)\exp(-i\Delta t)]\exp(-\gamma t). \tag{13}$$

The constant C is determined from the initial conditions $x(0) = x_0$ and $x(0) = v_0$. Using equation (13) and the initial conditions for the Floquet solution (11), the constant C is found to be

$$C = \frac{x_0 - i(Ax_0 + Bv_0)}{2}. \tag{14}$$

The general solution to the Hill equation (1) with damping is given by equations (12)–(14). To determine the general solution, two characteristic solutions $y_1(\tau)$ and $y_2(\tau)$ should be calculated over one period, $0 < \tau < T$.

CALCULATION OF THE FOURIER SPECTRUM

The Fourier spectrum of oscillations of a charged particle trapped in a periodic quadrupole field can be calculated using the general solution (13). We expand the periodic Floquet function $\phi(t)$ into the Fourier series

$$\phi(t) = \sum_{k=-\infty}^{\infty} \varphi_k \exp(ik\omega_0 t), \tag{15}$$

where $\omega_0 = 2\pi/T$ and

$$\varphi_k = \frac{1}{T}\int_0^T \varphi(t)\exp(-ik\omega_0 t)dt.$$

Substituting this expansion into (13) yields the solution to equation (1),

$$x(t) = \sum_k \Big\{ C\varphi_k \exp[i(k\omega_0 + \Delta)t] + C^*\varphi_k^* \times \exp[-i(k\omega_0 + \Delta)t] \Big\}\exp(-\gamma t). \tag{16}$$

To find the final expression, we should eliminate the factor $\exp(-\gamma t)$. The spectrum of signal (16) can be calculated by using the integral Fourier transformation,

$$x(\omega) = \frac{1}{2\pi}\int_{-\infty}^{\infty} x(t)e^{-i\omega t}dt, \qquad x(t) = \int_{-\infty}^{\infty} x(\omega)e^{i\omega t}d\omega. \tag{17}$$

When applying these formulas, we must define the function $x(t)$ at $t < 0$. In the context of our study, the specific form of this function is of no importance. Therefore, for $t < 0$, the solution (16) can be redefined by replacing the factor $\exp(-\gamma t)$ with $\exp(-\gamma|t|)$ without loss of generality. Thus, for the oscillation spectrum $x(\omega)$, we obtain

$$x(\omega) = \sum_{k=-\infty}^{\infty} \left[\frac{\gamma}{\pi}\frac{C\varphi_k}{(\omega - k\omega_0 - \Delta)^2 + \gamma^2} + \frac{\gamma}{\pi}\frac{C^*\varphi_k^*}{(\omega + k\omega_0 + \Delta)^2 + \gamma^2}\right]. \tag{18}$$

Equation (18) reveals the structure of the spectrum of parametric oscillations of a charged particle trapped in an RF quadrupole field. The spectrum consists of lines of the same width γ shifted by Δ to the “red” and “blue” sides from the harmonics $n\omega_0$: $\omega_n^+ = n\omega_0 + \Delta$, $\omega_n^- = (n+1)\omega_0 - \Delta$, where $n = 0, 1, 2, \ldots$. For undamped oscillations ($\gamma \longrightarrow 0$), the spectrum becomes discrete

$$x(\omega) = \sum_{k=-\infty}^{\infty} [C\varphi_k\delta(\omega - k\omega_0 - \Delta) + C^*\varphi_k^*\delta(\omega + k\omega_0 + \Delta)]. \tag{19}$$

Expressions (18) and (19) resolve the problem of analysis of the parametric oscillation spectrum. The inverse (synthesis) problem can be solved using equation (17). For undamped oscillations, taking into account the features of spectrum (19), we obtain

$$x(t) = 2\,\mathrm{Re}\left\{C\sum_{k=-\infty}^{\infty}\varphi_k\exp[i(k\omega_0 + \Delta)t]\right\}. \tag{20}$$

To calculate the spectrum, it is necessary to determine the complex amplitudes φ_k of the harmonics. For this purpose, two characteristic solutions $y_1(t)$ and $y_2(t)$ of the Hill equation should be determined for one period T. From (12) and (15), we find the amplitudes of the harmonics

$$\varphi_k = \Phi(k\omega_0 + \Delta), \tag{21}$$

where

$$\Phi(\omega) = \frac{1}{T}\int_0^T \left[y_1(t) + \frac{i - A}{B}y_2(t)\right]\exp(-i\omega t)dt.$$

According to (10), the ellipse parameters A and B and the frequency shift $\Delta = \pi\beta T$ are expressed through the values of the same solutions at the end of the period, $m_{11} = y_1(T)$, $m_{12} = y_2(T)$, and $m_{22} = \dot{y}_2(T)$. The expressions obtained are used below to calculate the ion oscillation spectrum in the cases most important from the practical standpoint.

STABILITY CONDITIONS AND THE SPECTRUM OF THE MATHIEU EQUATION

The obtained expressions for the spectrum of parametric oscillations of a charged particle in a quadrupole field are valid for the periodic source voltage of any shape. The amplitudes and phases of the harmonics depend on the shape of the source voltage $U(t)$. In case of harmonic voltage, $U(t) = U + V\cos(\omega_0 t)$, which is most frequently used in mass spectrometry, equation (1) reduces to the Mathieu equation. In this case, the motion of ions of given mass is determined by two dimensionless Mathieu parameters related to the amplitudes of the alternating and direct voltage components by

$$a = \varepsilon\frac{8eU}{mR_0^2\omega_0^2}, \quad q = \varepsilon\frac{4eV}{mR_0^2\omega_0^2}. \tag{22}$$

In the plane of parameters (a, q), we can separate out the stability regions, where the parameter β is real-valued, and the instability regions, i.e., the regions of parametric resonance. The boundaries of the regions are determined by the condition $\cos(\pi\beta) = \pm 1$. The parameter β of the Hill equation is determined accurate to unity. Therefore, it is impossible to determine uniquely from the value of the parameter β in which stability region the motion occurs. That is why, for the higher order stability regions, we take $n - 1 < \beta < n$, where n is the stability region number [6]. Note that, although the choice of one or another range of the parameter β variation affects the particle motion only slightly, it can change the meaning of the expressions. In the case under consideration, the parameter β enters in the expressions for the frequencies and amplitudes φ_k of the harmonics through the frequency shift Δ. In the first stability region, we have $0 < \beta < 1$; therefore, the lowest oscillation frequency (which corresponds to the amplitude of φ_0) is equal to $\beta\omega_0/2$. In the second stability region, we have $1 < \beta < 2$; therefore, the lowest oscillation frequency in this region is $(1 - \beta/2)\omega_0$ (the corresponding amplitude is φ_{-1}).

An uncertainty in determining the parameter β does not allow us to establish a qualitatively difference between the stability regions. Such a difference can be revealed through the analysis of the angular parameters of the Hill equation (1) [9]. These parameters are defined by analogy with the angular parameters of the harmonic oscillator equation

$$\kappa_1 = \int\limits_{U(t)>0}\sqrt{\frac{e}{mR_0^2}U(t)}\,dt,$$
$$\kappa_2 = \int\limits_{U(t)<0}\sqrt{-\frac{e}{mR_0^2}U(t)}\,dt. \tag{23}$$

The expression under the radical sign in (23) is the instantaneous oscillation frequency squared. Thus, the angular parameter κ_1 has the meaning of the oscillation phase incursion in the time interval during which the voltage is positive. In the negative- voltage intervals, the oscillation frequency is imaginary and, consequently, the motion in these intervals is not oscillating in character. As shown in [9], for harmonic and pulsed voltages, the nth stability region lies within the range $(n - 1)\pi < \kappa_1 < n\pi$. Thus, the stability regions differ by the phase incursion during the period T. In the positive-voltage intervals, an ion in the first region does not execute more than one-half oscillation, whereas an ion in the second region executes almost complete oscillation, etc. In turn, the numbers of zeros and maximum values in the dependence of the trapping ellipse parameters A, B, Γ on the field phase [6] vary according to the number of ion oscillations during the positive-voltage interval. That is why we defined the higher order stability regions as $n - 1 < \beta < n$. In this case, the parameter $\beta/2$ has the meaning of the number of ion oscillations during the period T.

Obviously, the change in the parameter β affects the spectral characteristics of motion. In the expression after formula (21), there is a pair of solutions to the Hill equation under the radical sign. The greater the number n of the stability region, the larger the number of oscillations executed by the particle during the period T. Thus, the width of the spectral function $\Phi(\omega)$ is proportional to the stability region number; i.e., the oscillation spectrum broadens. As will be shown below, this conclusion is supported by the results of calculations of the spectra in several important points in the stability regions.

Real ions move in the three-dimensional space. In a mass filter, the ions are separated along two directions, provided that $a_y = -a_x$, and, in an ion trap, they are separated along the three directions, provided that $a_x = a_y = -a_z/2$. Therefore, combined stability diagrams are constructed in the plane of the Mathieu parameters (a, q), in which the regions where the ion motion is stable in all directions are separated. As an example, such a diagram for a mass filter is shown in Fig. 1. The parameters (a, q) of ions of different masses lie on the same straight (working) line passing through the origin of coordinates. The inclination of the working line is $\tan\alpha = 2U/V$. To provide separation of ions of different masses, the source voltage parameters are selected so as the working line to intersect the stability regions near

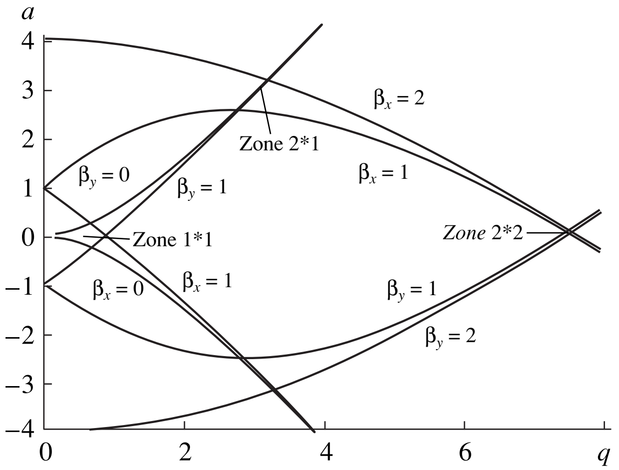

Fig. 1. Diagram of the stability of a quadrupole mass filter.

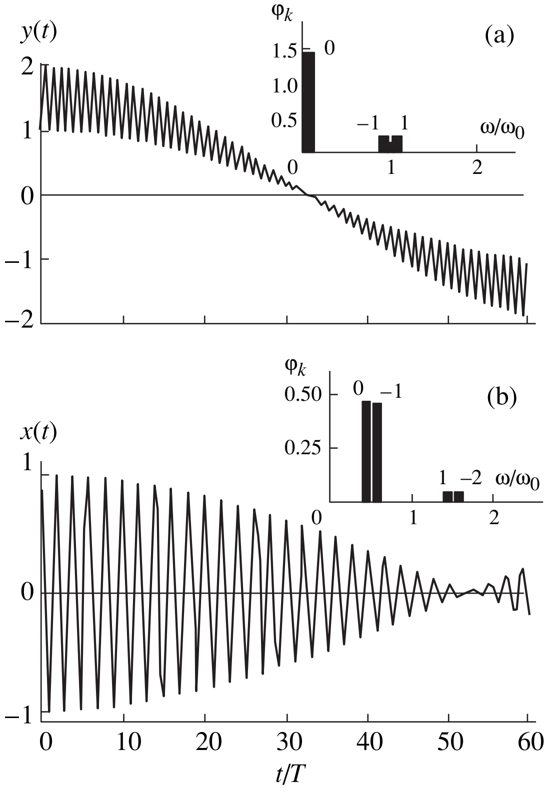

Fig. 2. Oscillations and their spectrum (see insert) at the vertex of the first stability region: (a) oscillations along the y-axis ($\beta_y = 0.015185$) and (b) oscillations along the x-axis ($\beta_x = 0.99046$). The working point ($a = 0.2368$ and $q = 0.706$) lies on the straight line corresponding to the resolution $R = 1000$.

its vertex. Thus, the ions moving outside the stability regions enter the region of parametric resonance along one of the coordinates and deposit on the electrodes of the system. That is why particular attention was given to the study of the spectral characteristics of motion at the vertices of the stability regions.

OSCILLATION SPECTRUM AT THE VERTICES OF THE STABILITY REGIONS

The dimensionless parameter $\xi = \omega_0 t/2$ is used to analyze the Mathieu equation. In dimensionless units, the source voltage period T is equal to π and the frequency ω_0 is equal to 2. If the initial phase is taken to be zero, the periodic voltage $U(\xi) = a + 2q\cos(2\xi)$ involved in the Mathieu equation is symmetric. As a result, the ellipse parameter A is zero, and the amplitudes φ_k of the harmonics are purely real. In this case, according to (20), the characteristic solution y_1 can be written as

$$y_1(t) = 2\sum_{k=-\infty}^{\infty}\varphi_k\cos(k\omega_0 + \Delta)t$$

$$= \sum_{k=-\infty}^{\infty}C_{2k}\cos(k\omega_0 + \Delta)t, \qquad (24)$$

$$\varphi_k = \frac{1}{2}C_{2k}.$$

This equation allows us to find the relation between the amplitudes φ_k and the coefficients C_{2k} conventionally used in the literature [3].

The upper vertex of the region 1×1 is formed by the intersection of the lines $\beta_x = 1$ and $\beta_x = 0$. Oscillations along the x-axis and y-axis are dissimilar. For the oscillations along the y-axis, we obtain that $\beta_y \approx 0$, the harmonic with the frequency $\Delta_y = \beta_y\omega_0/2$ has the maximum amplitude ϕ_0, the harmonics with the frequencies $\omega_0 + \Delta_y$ and $\omega_0 - \Delta_y$ have approximately equal amplitudes φ_1 and φ_{-1}, and the amplitudes of the other harmonics are small. In this case, the particle executes oscillations at a low frequency Δ_y accompanied by beatings at the carrier frequency ω_0 (Fig. 2a). The beat period is T/β_y; it is half as much as the low-frequency oscillation period. For the oscillations along the x-axis, we obtain that $\beta_x \approx 1$ and the harmonics with the frequencies $\beta_x\omega_0/2$ and $\omega_0 - \beta_x\omega_0/2$ have the maximum amplitudes approximately equal to each other. The motion along the x-axis (Fig. 2b) has the form of beatings at the frequency $\omega_0/2$ accompanied by beatings at the frequency $3\omega_0/2$ (they are formed by the harmonics $\omega_0 + \beta_x\omega_0/2$ and $2\omega_0 - \beta_x\omega_0/2$). Both beatings have the same period $T/(1 - \beta_x)$.

The results of calculating the oscillation spectrum at the vertex of the region 1×1 and other regions are given in the table. The parameters (a, q) lie on the working lines corresponding to the resolution $R = 1000$. It is seen from the table how the spectrum varies with increasing the region number. The upper boundary of the region 2×1 is formed by the intersection of the lines $\beta_x = 2$ and $\beta_y = 0$. In both cases, the low-frequency oscillations $\beta_y\omega_0/2$ and $(1 - \beta_x/2)\omega_0$ and the beatings at the frequency ω_0 are present. However, the beating amplitude in the first stability region (oscillations along the y-axis) is less than the low-frequency oscillation amplitude, whereas in the second stability region (oscillations along the x-axis), the low-frequency oscillation amplitude is significantly less than the beating amplitude. The lower boundary of the region 2 × 1 is formed by the intersection of the boundaries $\beta = 1$ of the first (oscillations along the y-axis) and second (oscillations along the x-axis) regions. In both cases, oscillations consist of beatings at the frequency $\omega_0/2$ (φ_0 and φ_{-1} harmonics) accompanied by the beatings at the frequency $3\omega_0/2$ (φ_1 and φ_{-2} harmonics). In the first region (oscillations along the y-axis), the amplitude of the beatings at the frequency $\omega_0/2$ is significantly greater than the amplitude of the beatings at the frequency $3\omega_0/2$, whereas in the second region (oscillations along the x-axis), the two amplitudes are approximately equal to each other. However, the amplitude of the beatings at the frequency $3\omega_0/2$ in the second region (see table, the top of the region 2 × 2, oscillations along the y-axis) can exceed the amplitude of the beatings at the frequency $\omega_0/2$ in the same region.

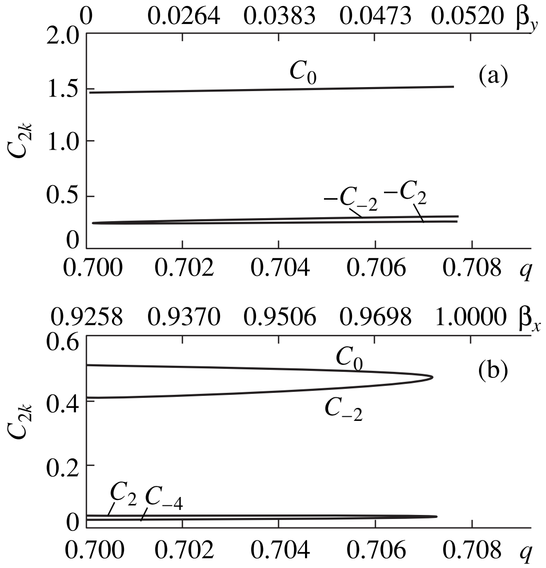

Fig. 3. Dependence of the amplitudes of spectral components on the parameter q at the upper vertex of the region 1 × 1 along the line corresponding to the theoretically determined resolution $R = 100$: (a) oscillations along the y-axis and (b) oscillations along the x-axis.

Dependences of the amplitudes of spectral components on the parameter q are shown in Figs. 3 and 4. The dependence of the amplitudes of spectral components on the parameter q at the vertex of the first stability region (i.e., near the boundary $\beta_y = 0$) for the motion along the y-axis is shown in Fig. 3a. It is seen that the amplitudes of spectral components varies only slightly with varying the parameter q. The same dependence at the vertex of the 2 × 1 region (i.e., also near the $\beta_y = 0$ boundary, but at higher values of the parameter q) is more pronounced and nonlinear (Fig. 4a). In both cases, the amplitudes of spectral components attain certain finite values at the boundary $\beta_y = 0$. The amplitudes of spectral components of oscillations along the x-axis as functions of the parameter q show a similar behavior near the boundary $\beta_x = 1$ (Fig. 3b). However, the same dependences in the second stability region near the boundary $\beta_x = 2$ are fundamentally different: at the boundaries of the region, the amplitudes of spectral components tend to infinity (Fig. 4b). An unbounded

Spectral components in various stability regions

Parameter	Top of the region 1 × 1	Top of the region 2 × 1	Bottom of the region 2 × 1	Top of the region 2 × 2
a	0.236813	3.16329	2.52194	0.026175
q	0.706000	3.23408	2.8153	7.54728
β_x	0.988491	1.978873	1.025012	1.847750
$\varphi_{0,x}$ ($C_0/2$)	0.467997	63.86192	59.89509	173.7649
$\varphi_{-1,x}$ ($C_{-2}/2$)	0.455282	–1.867393	–58.16327	–22.37399
$\varphi_{1,x}$ ($C_2/2$)	0.038039	16.72962	26.86175	100.3778
$\varphi_{-2,x}$ ($C_{-4}/2$)	0.036524	–62.03566	–27.43166	–173.7560
$\varphi_{2,x}$ ($C_4/2$)	0.001089	–1.669366	3.3522398	22.79408
β_y	0.0151852	0.102606	0.9194426	1.1550037
$\varphi_{0,y}$ ($C_0/2$)	1.4736736	5.749320	30.18155	3.308715
$\varphi_{-1,y}$ ($C_{-2}/2$)	–0.250983	–3.006374	–28.19290	2.628310
$\varphi_{1,y}$ ($C_2/2$)	–0.243811	–2.635821	–7.906595	–3.224624
$\varphi_{-2,y}$ ($C_{-4}/2$)	0.0110046	0.537883	6.766214	–3.566485
$\varphi_{2,y}$ ($C_4/2$)	0.0105312	0.431949	0.837913	0.9554039

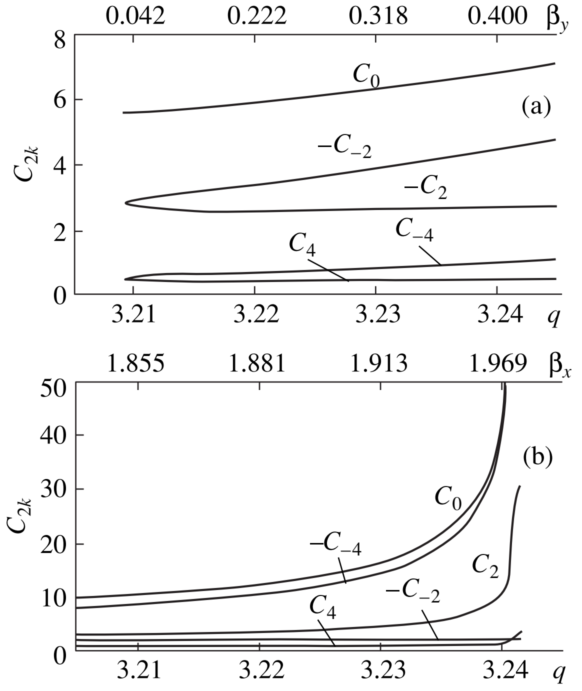

Fig. 4. Same as in Fig. 3 at the upper vertex of the region 2×1.

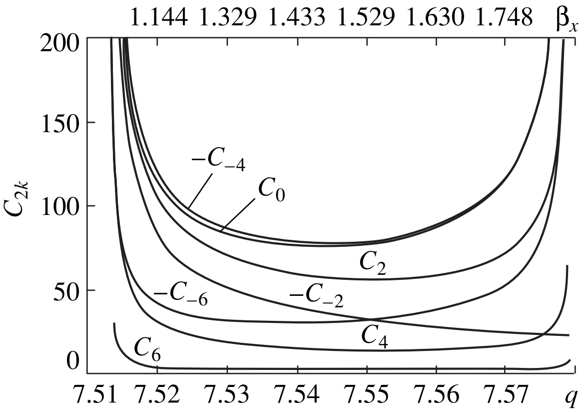

Fig. 5. Dependence of the amplitudes of spectral components of oscillations on the parameter q within the region 2×2 along the line $a = 0$.

increase in the amplitudes of spectral components when approaching the boundaries of the stability region is characteristic of the second stability region. Variations in the amplitudes of spectral components in the second stability region along the $a = 0$ line between the boundaries $\beta_x = 1$ and $\beta_x = 2$ are shown in Fig. 5. It is seen that, at the boundaries of the stability region, the amplitudes of spectral components tend to infinity.

Presumably, this fact explains why higher order stability regions are preferable as compared to the first stability region. The amplitude of oscillations of stable ions increases sharply near the boundary $\beta_x = 1$ as the value of $\beta_x - 1$ decreases. Therefore, the required selectivity can be achieved at lower values of $\beta_x - 1$, i.e., during a smaller number of periods of ion oscillations in a quadrupole field and at a smaller total length of the rods.

CONCLUSION

The spectrum of parametric oscillation described by the Hill equation (1) has been studied. In the general case, the spectrum (18) consists of two systems of lines. Each of the harmonics $n\omega_0$ of the fundamental frequency ω_0 is accompanied by satellites shifted to the "red" and "blue" sides by $\Delta - \beta\omega_0/2$. In the presence of linear damping, all the lines have the same half-width γ, whereas in the absence of damping, the spectrum is discrete. The dependence on the initial conditions enters the expressions obtained through the factor C (14), and the spectral composition is determined by the time profile of the source voltage. The amplitudes of the spectral components can be calculated using the spectral function $\Phi(\omega)$, which is determined by a pair of characteristic solutions to the Hill equation over one period (21). Equation (21) can be efficiently applied to calculating the amplitudes of spectral components.

The character of oscillations depends substantially on the fundamental parameter β. In the first stability region, where $0 < \beta < 1$, the low-frequency harmonic $\beta\omega_0/2$ has the maximum amplitude. Consequently, oscillations near the boundary $\beta = 0$ are close to harmonic. Near the boundary $\beta = 1$, the amplitudes and frequencies of the harmonics $\beta\omega_0/2$ and $(2 - \beta)\omega_0/2$ are almost equal, which results in beatings at the frequency $\omega_0/2$. In the higher order stability regions, the oscillation spectrum broadens, but oscillations always have the form of beatings. For example, in the second region near the boundary $\beta = 1$, the beatings at the frequency $\omega_0/2$ are accompanied by the beatings at the frequency $3\omega_0/2$ generated by the harmonics $(4 - \beta)\omega_0/2$ and $(2 + \beta)\omega_0/2$. Both beatings have the same frequency $(\beta - 1)\omega_0$. Thus, the oscillations have the form of complicated beatings at the frequency $(\beta - 1)\omega_0$. To avoid confusion, it should be noted that the beat frequency, which determines the shape of oscillations, is absent in the oscillation spectrum. Oscillations near the boundary $\beta = 2$ are the sum of beatings at the carrier frequencies ω_0, $3\omega_0$, …. All of the beatings have the same frequency $(2 - \beta)\omega_0$ equal to the frequency of the low-frequency harmonic φ_{-2}, which is present in the oscillation spectrum. However, near the boundary $\beta = 2$, the amplitude of the harmonic φ_{-2} is substantially smaller than the amplitudes of harmonics generating the beatings. Ion trajectories always have the form of beatings, which is due to the periodicity of the solutions to the Mathieu equation in cases when $\beta = m/n$ is a proper fraction [8].

The amplitudes of spectral components do not depend on the phase of the source voltage. Like the β_x and β_y parameters, they are determined by the position of the working point (a, q) on the stability diagram. The study of variations of the amplitudes of spectral component within the stability regions provides much more information than the study of the trajectories of motion in time and on the phase plane. It is shown that, in the first stability region, the amplitudes of spectral components tend to certain finite values when approaching the boundary of the region. In the second stability region, the amplitudes tend to infinity when approaching the boundary of the region. In my opinion, this explains the well-known fact [6] that, in the devices operating in the higher order stability regions, the required selectivity is attained at a smaller total length of the rods of the field-generating system, i.e., during a smaller number of periods of ion oscillations in a quadrupole field.

ACKNOWLEDGMENTS

I am grateful to N. V. Konenkov for his support and fruitful discussions.

REFERENCES

1. P. H. Dawson, *Quadrupole Mass Spectrometry and Its Applications* (Elsevier, Amsterdam, 1976).
2. R. E. March and R. J. Hughes, *Quadrupole Ion Storage Mass Spectrometry* (Wiley, New York, 1989).
3. N. W. McLachlan, *Theory and Applications of Mathieu Functions* (Clarendon, Oxford, 1947).
4. Y. Wang, J. Franzen, and K. P. Wanczek, Int. J. Mass Spectrom. Ion Processes **124**, 125 (1993).
5. R. L. Alfred, F. A. Londry, and R. E. March, Int. J. Mass Spectrom. Ion Processes **125**, 171 (1993).
6. N. V. Konenkov and V. I. Kratenko, Int. J. Mass Spectrom. Ion Processes **108**, 115 (1991).
7. V. I. Arnold, *Mathematical Methods of Classical Mechanics* (Springer-Verlag, New York, 1989; Nauka, Moscow, 1989).
8. *Handbook of Mathematical Functions*, Ed. by M. Abramowitz and I. A. Stegun (Dover, New York, 1965; Nauka, Moscow, 1979).
9. M. Yu. Sudakov, Zh. Tekh. Fiz. **64**, 170 (1994) [Tech. Phys. **39**, 96 (1994)].

Translated by K. Chamarovskiĭ

Technical Physics, Vol. 45, No. 3, 2000, pp. 330–333. Translated from Zhurnal Tekhnicheskoĭ Fiziki, Vol. 70, No. 3, 2000, pp. 44–47.
Original Russian Text Copyright © 2000 by Gabdullin, Golikov, Krasnova, Davydov.

ELECTRON AND ION BEAMS, ACCELERATORS

Application of Donkin's Formula in the Theory of Energy Analyzers: Part II.

P. G. Gabdullin, Yu. K. Golikov, N. K. Krasnova, and S. N. Davydov
St. Petersburg State Technical University, St. Petersburg, 195251 Russia

Received December 1, 1998; in final form, August 18, 1999

Abstract—Studies of conic-type electric-field structures are continued. The electric field is investigated, and its potential is described by the following analytical expression.

$$\Phi(x, y, z) = \frac{x}{z + \sqrt{x^2 + y^2 + z^2}}. \tag{1}$$

Expression (1) is derived on the basis of Donkin's formula. Properties of these electric fields are described in Part I [1]. © *2000 MAIK "Nauka/Interperiodica".*

We consider thoroughly the dynamics of a charged-particle flux in the electric field with potential (1). To obtain such an electric field in a certain spatial region, we make the limiting electrodes of a charged-particle energy analyzer in the form of equipotential surfaces. To do this, we ground the lower electrode and apply to the other electrode a deflecting voltage. For the lower electrode, we choose an equipotential surface with a number $\Phi = 1$. The upper electrode will be determined later, because its choice depends on the maximum height of particle trajectories in the electric field.

The actual motion of particles in the electric field is determined by the particle electric charge and mass, the electric-field distribution, the initial conditions, and the system linear size. The system isomorphic mathematical model contains a lesser number of independent parameters determining the structure of the particle motion, because some of them, by choice of special units of measurement are integrated into a single complicated nondimensional parameter. This simplifies mathematical expressions by excluding from them insignificant coefficients but preserving the clear physical meaning of all the values. It is the nondimensional mathematical model [2] that will be used in this paper.

The equations of particle motion (we imply electrons in this case) in the electric field can be written out in the form

$$\ddot{x} = -\frac{z^2 + y^2 + \sqrt{x^2 + y^2 + z^2}}{(z + \sqrt{x^2 + y^2 + z^2})^2 \sqrt{x^2 + y^2 + z^2}},$$

$$\ddot{y} = \frac{xy}{(z + \sqrt{x^2 + y^2 + z^2})^2 \sqrt{x^2 + y^2 + z^2}}, \tag{2}$$

$$\ddot{z} = \frac{x(z + \sqrt{x^2 + y^2 + z^2})}{62(z + \sqrt{x^2 + y^2 + z^2}) \sqrt{x^2 + y^2 + z^2}}.$$

Since analytically solving the set of simultaneous equations (2) is impossible, we have used numerical methods (for example, the fourth-order Runge–Kutta method).

A comprehensive computer code was developed in the framework of investigating all the electron-optical properties of the electric field. This made it possible to calculate and plot the entire set of trajectories by varying initial conditions including the energy of particles, their coordinates, and the angle of entry. Thus, the linear dispersion and coefficients of squeezing as functions of the initial particle energy were obtained. Since the results preliminary here are previous and have an evaluating character, we restrict ourselves by considering only the "boundary–boundary" focusing conditions.

POINT SOURCE

A point source is assumed to be located at a point with coordinates ($x = 1$, $y = 0$, $z = 0$) laying on the surface $\Phi = 1$. The initial nondimensional energy was varied within the range from 0 up to 1.4, the of angle entry into the field, i.e., the angle between the velocity particle vector and the x-axis, was chosen within the range 0° to 45°. A slightly divergent charged-particle beam directed along the x-axis towards a singular point of the field, which is located at the origin of coordinates, was been studied. The central trajectory of this beam lies in the plane $y = 0$. The beam is confined within a small angle of 1° in both directions with respect to this plane.

Figure 1 shows the particle angles of entry and exit as functions of the initial energy in the case of the first-order focusing at the electric-field boundary. As is seen from Fig. 1, the conditions of "boundary-boundary" focusing correspond to low values of the energy virtually in the same manner as in the case of a plane mirror, $\theta_{1\Phi} = \theta_{2\Phi} = 45°$. The angle of entry θ_1 decreases and the angle of exit θ_2 increases with raising the particle energy. In this case, the function $\theta_2(W)$ increases more rapidly compared to the decrease of the function $\theta_1(W)$. This is explained by the fact that the effect of the electric field is the most strong at the second part of a particle trajectory, because just in this region, the equipotential surfaces are deformed more strongly compared to the case of a plane capacitor. We note as a comparison that for a particle with the energy $W = 0.5$ the angles of entry and exit are 38° and 62°, respectively, whereas the corresponding values for a particle with the energy $W = 1$ are $\theta_1 = 27°$ and $\theta_2 = 90°$, respectively.

There exists a "telescopic" effect in conic-shape electric fields: an arbitrary parallel beam of particles with finite thickness and width, which propagates toward a singular point located at the origin of coordinates is subjected to squeezing. At the some time, the beam of particles propagating in the opposite direction diverges. The electric fields under study are not an exclusion; therefore in the regime consideration, the beam of charged particles with a finite initial size becomes narrower.

Figure 2 illustrates the effect of squeezing. The squeezing coefficients M and N represent the variation of the beam width along the x- and y-axes, respectively: $M = \Delta x_1/\Delta x_2$, $N = \Delta y_1/\Delta y_2$. For conic-shape electric fields the coefficient of squeezing along an arbitrary direction can be written out as a ratio of the initial and final beam coordinates:

$$M = \frac{x_1}{x_2}, \quad N = \frac{y_1}{y_2}. \tag{3}$$

As is seen from Fig. 2, the particle beam experiences the maximum squeezing along the direction of its propagation, whereas, in the transverse direction, the coefficient of squeezing does not exceed the value of 6 for a wide range of energies under study. For example, the coefficients of squeezing for a beam of particles with the energy $W = 1$ are $M = 23$ and $N = 6$ along the x- and y-axes respectively, while the same coefficient related to the beam area is $M \times N = 138$.

The energy dispersion defined by the formula

$$D = \frac{\Delta x}{\Delta W} W \tag{4}$$

is one of the principal electron-optical parameters for an energy analyzer.

Linear energy dispersion in the plane of propagation of the beam has a maximum within the energy range 0.45 and 0.55 (in conditional units), see Fig. 3.

Besides the aforesaid parameters, the quality of the energy analyzer is also defined by its resolution R: $R = W_0/\Delta W$, because the error of the analysis is determined, first of all, by the size of the non-resolved energy range ΔW. The value of R depends both on the linear energy dispersion and on the dimensions of the output diaphragm. The latter is much smaller than the input one owing to the "telescopic effect" in the conic electric fields. The dimensions of the output diaphragm can be estimated as a product of the width of the input one and the coefficient of squeezing. Therefore, in devices of this type, it is more reasonable to use, instead of the usual dispersion D in the expression for the resolution R, the value of effective dispersion D is reduced to the input diaphragm: D^*: $D^* = D \times M$.

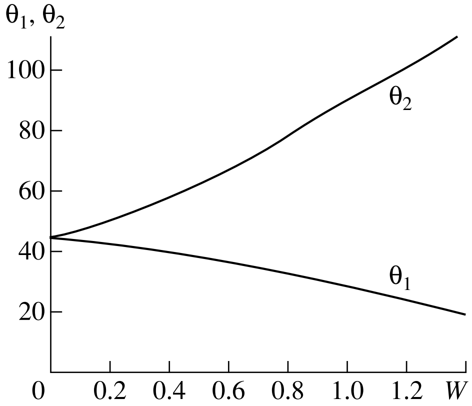

Fig. 1. Angle of entry (θ_1) and angle of exit (θ_2) for particles propagating in electric field (1) as a function of their initial energy in the regime of "boundary-boundary" focusing. The source coordinates are (1, 0, 0); slightly divergent beam of particles propagating to the origin has the angular spread of 2° with respect to the central trajectory lying in the plane $y = 0$.

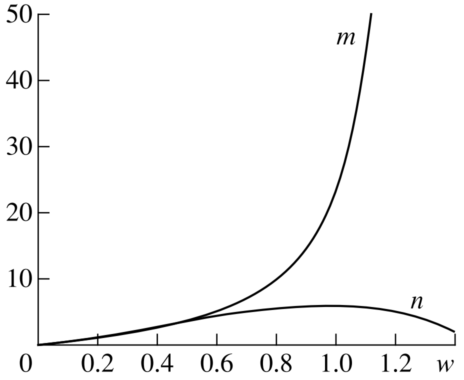

Fig. 2. Coefficients M and N of squeezing for a wide particle beam in electric field (1) along the x- and y-axes respectively. These coefficients are calculated for the regime of the first-order "boundary-boundary" focusing.

Figure 4 shows the variation of D^* asa function of the initial particle energy. As is seen from Fig. 4, the value of D^* increases according to the exponential law with increasing the particle energy. For comparison, the dashed line represents the similar dependence calcu-

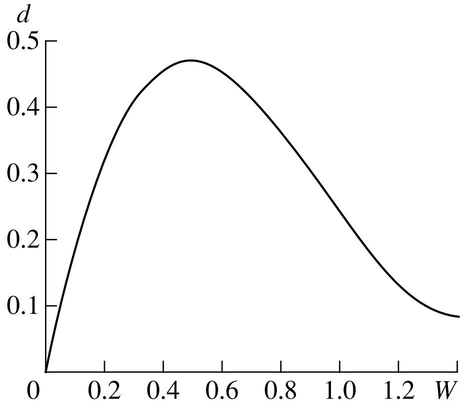

Fig. 3. Linear energy dispersion (*D*) in the electric-field structure under study.

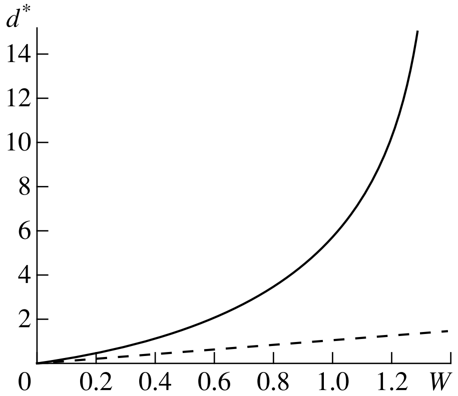

Fig. 4. Effective energy dispersion (D^*) reduced to the input as a function of the initial particle energy in the case of the first-order "boundary-boundary" focusing. Dashed line represents the same curve for the electric field of a plane capacitor.

lated under the same initial conditions for a plane capacitor. The effective dispersion $D^* = 5.5$ and 1 in the case of the electric field (1) and the plane capacitor, respectively, for particles with the energy $W = 1$.

A CASE OF FINITE-SIZE SOURCE

We now consider the transformation by the field (1) of the particle flux emitted from a certain area with a finite size. We choose the following working conditions: the initial energy of particles $W = 1$; the angle of entry for the beam is $\theta_1 = 27°$. The particles are emitted from an area of the lower electrode ($\Phi = 1$), which has the size $x = 1 \pm 0.05$, $y = 0 \pm 0.05$, the point with coordinates (1, 0, 0) being the central point of this area. Using the computer code developed, we have plotted the set of trajectories passing through the area chosen, each of them being lain in one of the planes y = const. The results of the calculations have shown that the particles are collected in to a spot whose shape is distorted with respect to the prescribed quadratic one, the size of the spot being decreased.

The following conclusion can be made on the basis of the analysis performed. Let the basic dimensions of the charged-particle energy analyzer be about 100 mm. The area of 10×10 mm^2 is used as a particle source. The beam of particles is injected into the field region at an angle of 27° through the lower electrode that has the shape of an equipotential surface with the number $\Phi = 1$. In this case, the beam exits the electric field practically at the right angle. The cross section of the beam in the x–y plane will decrease more than by a factor of 130, the beam being conserved the form of parallelepiped. In this operating regime, the effective dispersion D^* attains 5.5, and the relative energy resolution r is approximately equal to 0.08%.

Such an energy-analyzing system can be used for monochromatizing beams of charged particles with their further transportation and application of the monochromatized beams in the charged-particle energy analyzers. The monochromators of such a kind have a clear advantage compared to conventional analyzers used in electron spectroscopy. Exploiting the telescopic effect, we can inject through a wide input diaphragm in to the electric field, an electron beam with the intensity by the order an magnitude higher with respect to that in usual systems. For the narrow input diaphragm, we can obtain the monochromatized electron beam with the absolute resolution comparable with that of a conventional device but of much higher intensity. Thus, as calculations show, we can increase the intensity of a monochromatized electron beam at least by the factor of three, the absolute resolution being the same as that attained in the well-known modern monochromators. (We imply systems with the following parameters: maximum electric current is $I_m = 10^{-9}$ A and energy resolution is $\Delta E = 10$ meV.

Another application could be formation of wide-aperture weak particle beams, in experiments, e.g., with cosmic rays. Such a system close to those described in this paper and exhibiting high electron-optical properties could be used in the field of electron and ion spectroscopy as an efficient charged-particle energy analyzer.

IMPLEMENTATION OF THE SYSTEM

An advantage of implementing the system described above is, without doubt, its technological simplicity. An electrode corresponding to the equipotential surface $\Phi = 1$ can be manufactured by the following method. As was mentioned above, the equipotential surfaces studied relate to the class of conic structures. Therefore, for any equipotential surface, there exist its direct components, i.e., rays issued from the origin of coordinates and the plane of symmetry $y = 0$. The section of the equipotential surface by the planes x = const are parabolas with their shapes being transformed with the x-coordinate: the parabola branches approach the plane $y = 0$ as the x-coordinate approaches the point $x = 0$. Two metal mountings manufactured in the form of parabolas can be fixed firmly with respect to each other by threads pulled along the rays mentioned above. Such a structure is quite acceptable for manufacturing the lower electrode, because it is usually grounded or the voltage of a power source is applied to it. For the upper electrode, an almost plane plate mounted at the proper position can be used.

CONCLUSION

Thus, the simplest electric-field structures formed by conic equipotential surfaces, which had been calculated on the basis of Donkin's formula, were considered in Part I of this paper. In spite of the simplicity of analytical expressions for potentials of electric fields, such systems are promising from the should point of further studies and results expected. The effect of "telescopic" deformation of charged-particle fluxes attracts the attention researchers. A concept has been suggested for constructing conic electric fields including well-known structures, and it opens wide horizons for finding new configurations of electric fields for further studies and use in charged-particle energy analyzers. The boundary value problem has been solved for the "conic" electric fields having a symmetry plane. This leads, in turn, to a possibility of solving a variety of inverse problems in electron optics.

The results of calculations of electron-optical parameters for one of the simplest representations for the electric potential, which was derived on the basis of Donkin's formula are presented in Part II. These results demonstrate a possible application in practice of "conic"-type electric fields for monochromatizing or squeezing broad fluxes of charged particles. The input cross section of charged-particle source image is reduced more than by a factor of 100 after particles have passed through such a system. The energy dispersion in (reduced to the input) the plane of motion exceeds by several times the similar value for a plane capacitor. The conic nature of the field under consideration makes it possible to apply a simple and an elegant method of constructing equipotential surfaces and, correspondingly, to develop charged-particle energy analyzers.

REFERENCES

1. P. G. Gabdullin, Yu. K. Golikov, N. K. Krasnova, *et al.*, Zh. Tekh. Fiz. **70** (2), 91 (2000).
2. Yu. K. Golikov, K. G. Utkin, and V. V. Cheparukhin, *Calculations of Elements of Electrostatic Electron-Optical Systems* (Leningradsk. Politekh. Inst., Leningrad, 1984).

Translated by A. Lytkin

Technical Physics, Vol. 45, No. 3, 2000, pp. 334–338. Translated from Zhurnal Tekhnicheskoĭ Fiziki, Vol. 70, No. 3, 2000, pp. 48–51.
Original Russian Text Copyright © 2000 by Dziedzic, Snarskiĭ, Buda.

Nonlinear Properties of Two-Phase Composite Films with a Fractal Structure

A. Dziedzic*, A. A. Snarskiĭ, and S. I. Buda****
** Wroclaw Institute of Technology, Wroclaw, Poland*
*** National Technical University of Ukraine, Kiev, 256057 Ukraine*

Received March 10, 1998; in final form, July 26, 1999

Abstract—Inhomogeneous two-phase conducting films whose structure is intermediate between three- and two-dimensional configurations are discussed. The longitudinal film size exceeds the correlation length, and its thickness is less than the correlation length. In the case of weak nonlinearity, we found dependences of the film resistivity on the concentration and size of conducting particles, as well as on the film thickness, in the framework of a percolation approach. © *2000 MAIK “Nauka/Interperiodica”.*

INTRODUCTION

Film structures are widely used in modern microelectronics. Thick-film resistors (TFRs) are an example (see [1, 2] and references therein). Cubic nonlinearity in metal-ceramic and polymer-based TFRs, which is discussed below, was observed, for example, in [3, 4] (Fig. 1).

Typical dimensions of TFRs are L = 1–5 mm (length) and H = 20–25 μm (thickness). The particle size is about 0.1–1 μm for the conducting phase and ~0.7–7 μm for the glass. The conducting particles are spaced 1–2 nm apart (Fig. 2). If the general current flows over the substrate, local currents will have a component normal to the substrate, as follows from the aforesaid. Therefore, a TFR is not a two-dimensional (2D) structure with respect to the current flow. Neither is it a 3D structure in general. In order for a TFR be 3D, it should satisfy the condition $H \gg \xi$, where ξ is the correlation length. Thus, the problem of determining the TFR conductivity can be classified as intermediate between the 2D and 3D problems. For brevity, we shall refer to this problem as 2.5D.

Analysis of experimental data for TFRs and other composite systems is often based on the conventional two-phase percolation model. This model implies a universal dependence of the effective resistivity ρ_e on the content p of the conducting phase with a resistivity ρ_1. For example, at $p > p_c$ (p_c is the percolation threshold), $\rho_e \sim \rho_1(p - p_c)^{-t}$, where t is the unique critical conductivity exponent ($t_3 \approx 2$ for a 3D system). In many cases, such a percolation description agrees well with experiment. For example, the values of t ranging from 1.7 ± 0.2 to 2.3 ± 0.4 were reported [5, 6]. In these films, the resistance per square varied by a factor of 10^6. At the same time, the critical exponents calculated from data in [7] equal 2.65, 2.87, and even 2.99. Similar t values (between 2.26 and 2.87) were obtained for polymer thick-film resistors containing high-structure carbon black [8]. However, t values reported in [9] are as high as 20, which contradicts the hypothesis for the universatility of the critical exponents. In our opinion, the percolation theory for two-phase systems is not applicable to all TFRs (not to conditions, preparation techniques, etc.). Nevertheless, the percolation approach is in many cases adequate, not only giving an idea of the critical behavior of the conductivity but also fitting experimental data on $1/f$ noise and third harmonics generation (see, for example, [10–13]).

Linear conductivity in 2.5D TFRs was discussed in [14–18]. The basic concept in the theoretical description of the conductivity of an inhomogeneous film (Fig. 2) with $H < \xi_3$ and $L \gg \xi_3$ (ξ_3 is the correlation length of a 3D system) is that the film is represented as

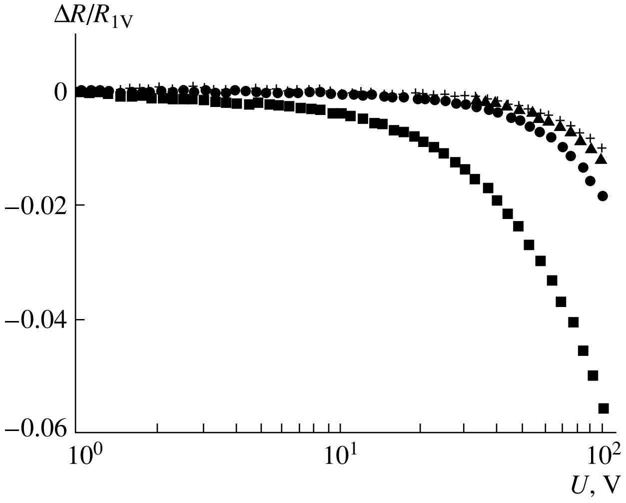

Fig. 1. Resistance of TU-10K-5 polymer thick-film resistors versus voltage. The drying temperatures are (■) 150, (●) 190, (▲) 230, and (+) 270°C. $R = R(U) - R_{U = 1V}$.

a set of $H \times H \times H$ cubes. In the simplest approximation, the film has a fractal configuration due to local structure fluctuations. Some of the cubes include a conducting cluster, while others do not; accordingly, these cubes are of high and low conductivity, respectively. A TFR appears as a 2D two-phase system consisting of high- and low-conductivity $H \times H \times H$ elements. Within this approximation, we can apply the conventional 2D description of TFRs. For example, the resistance of an a_0-thick film above the percolation threshold ($p > p_c$) can be written as $R = r_1((p - p_{c2})/p_{c2})^{-t_2}$, where $r_1 = \rho_1 a_0/a_0^2$, ρ_1 is the resistivity of the conductive phase ($\rho_1 \ll \rho_2$), and a_0 is the characteristic minimum size (in lattice problems, the link length).

CALCULATION OF NONLINEAR FILM RESISTANCE

When modeling a 2.5D system, we should replace (as with the 2D case) r_1 by $r_1(H)$, that is, by the resistance of an $H \times H \times H$ cube including the percolation structure. Then, we have for the 2.5D film

$$R_{2.5} = r_1(H)\left(\frac{P_H - p_{c2}}{p_{c2}}\right)^{-t_2}, \tag{1}$$

where P_H is the concentration of $H \times H \times H$ cubes with the resistance $r_1(H)$.

Thus, to calculate the film resistance under 2.5D conditions, one should know an $r_1(H)$ dependence and the probability of a conductive configuration. To find them, we will take advantage of the approach formulated in [19], which is easily extended to the nonlinear case. According to [19], $r(H)$ in the fractal range ($H < \xi$) is determined from the percolation scheme in the smear region [20, 13]. Here, the width of the smear region is given by $\tau_H = (H/a_0)^{-1/\nu_3}$, where ν_3 is the critical exponent for the correlation length.

In the smear region, according to the percolation scheme, we can find with a probability P_H a structure related to the percolation above the percolation threshold (that is, a bridge with a length N_1/a_0) and, with a probability $1 - P_H$, a spacer (N_2 poorly conductive links connected in parallel). The resistances of the bridge and the spacer are $R_1 = r_1N_1$ and $R_2 = r_2/N_2$, respectively. Here, $N_i = |\Delta|^{-\alpha_i}$; Δ is the smear width; $\alpha_1 = t - \nu(d - 2)$ and $\alpha_2 = q + \nu(d - 2)$; and t and q are the critical exponents above and below the percolation threshold, respectively.

Replacing Δ by, for example, τ_H in the expressions for R_1 and R_2 yields

$$r_1(H) = \rho_1(H/a_0)^{(t_3 - \nu_3)/\nu_3}/a_0 \tag{2}$$

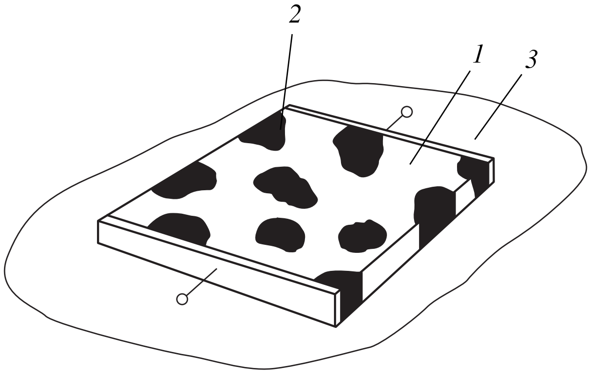

Fig. 2. Typical geometry of thick-film resistors: $a_0 \sim 0.1$–1, $b_0 \sim 0.7$–7, and $H \sim 20$–25 μm; (*1*) thick-film resistor, (*2*) highly conducting inclusions, and (*3*) nonconducting substrate.

for the highly conductive realization [21] and

$$r_2(H) = \rho_2(H/a_0)^{-(q_3 + \nu_3)/\nu_3}/a_0 \tag{3}$$

for the poorly conductive realization,

In (2) and (3), we neglect shunting of the second phase and the voltage drop across the first phase. The probabilities of finding the realizations with $r_1(H)$ and $r_2(H)$ are, respectively [19],

$$P_H = \frac{\tau_H + \tau_3}{2\tau_H}, \quad 1 - P_H = \frac{\tau_H - \tau_3}{2\tau_H}. \tag{4}$$

Thus, the closeness of the film to the percolation threshold is characterized by the parameter

$$\tau_{2.5} = \frac{P_H - p_{c2}}{p_{c2}} = \frac{\tau_3}{\tau_H}, \tag{5}$$

where we take into account that $p_{c2} = 1/2$ and the subscript 2.5 indicates that we are dealing with the concentration of $H \times H \times H$ cubes in the 2.5D system.

In what follows, we will consider a "highly fractal regime," where $\tau_H \gg |\tau_3|$ (for details, see [19]). From (5), $|\tau_{2.5}| \ll 1$ in this case; that is, we can assume that a 2.5D system is close to the percolation threshold and can be described in terms of the percolation theory. Substituting (2) and (5) into (1), we find for the 2.5D film

$$R_{2.5} = \rho_1(H/a_0)^{\frac{t_3 - t_2 - \nu_3}{\nu_3}}\tau_3^{-t_2}/a_0. \tag{6}$$

Let us now consider the case of weakly nonlinear conductivity. With an accuracy to cubic terms,

$$\begin{gathered}\mathbf{E} = \rho_i(\mathbf{j})\mathbf{j} = \rho_i\mathbf{j} + \mu_i\mathbf{j}^2\mathbf{j},\\ \mathbf{j} = \sigma_i\mathbf{E} + \chi_i\mathbf{E}^2\mathbf{E},\end{gathered} \tag{7}$$

where μ_i and χ_i are the nonlinear parts of the resistivity and conductivity, respectively. It is assumed that $\mu_i j^2 \ll \rho_i$ and $\chi_i E^2 \ll \sigma_i$. In terms of resistance, we can write

$$\begin{aligned} r_i(I_i, a_0) &= r_i(a_0) + m_i(a_0) I_i^2, \\ r_i(a_0) &= \rho_i/a_0, \quad m_i(a_0) = \mu_i/a_0^5, \end{aligned} \tag{8}$$

where $r_i(I_i, a_0)$ is the nonlinear resistance of an $a_0 \times a_0 \times a_0$ element in the ith phase and I_i is the total current through this element.

In the nonlinear case [see (8)], the resistance of the bridge is determined as above: $R_1 = r_1(I_1, a_0)N_1$. The resistance of the spacer is conveniently found from the conductance $g_2(\Delta\varphi)N_2$ of the $a_0 \times a_0 \times a_0$ element, where $\Delta\varphi$ is the voltage difference across this element. Then the conductance of the spacer is $G_2 = g_2(\Delta\varphi)N_2$, and its resistance $R_2 = 1/G_2$. With an accuracy to cubic terms of the current, we find

$$R_i(I, H) = r_i(H) + M_i(H) I^2, \tag{9}$$

where the total current I through the $H \times H \times H$ cube, as well as $r_1(H)$ and $r_2(H)$, have, of course, the same form as in (2) and (3). The nonlinear parts can be written as

$$\begin{aligned} M_1(H) &= \mu_1 \tau_H^{-(t_3 - \nu_3)} a_0^{-5}, \\ M_2(H) &= \mu_2 \tau_H^{3(q_3 + \nu_3)} a_0^{-5}. \end{aligned} \tag{10}$$

Apply the well-known expressions [22] for a two-dimensional film in the case of weak nonlinearity:

$$\sigma_e(p) = \sigma_1 \tau^{t_2}, \quad \chi_e = \chi_1 \tau^{-k_2}, \quad p > p_c, \tag{11}$$

$$\sigma_e(p) = \sigma_2 |r|^{q_2}, \quad \chi_e = \chi_2 |\tau|^{-k_2^0}, \quad p < p_c, \tag{12}$$

where k_2 and k_2' are the critical exponents for 1/f noise.

Note that, in [22], the nonlinear relationship between the current density and the field was chosen in the form $j = \sigma E + \chi E^2 E$. However, it is easy to see that $\mu = -\chi\sigma^4$ with an accuracy to cubic terms. If k_2 and k_2' are expressed through t, q, and ν [23], i.e., $k_2 = 2\nu_2 - t_2$, $k_2' = 2\nu_2 - q_2$, then we can write $R_{2.5}(I)$ in the following form instead of (1):

$$R_{2.5}(I) = r_1(H)\tau_{2.5}^{-t_2} + M_1(H)\tau_{2.5}^{-t_2} I^2, \quad p > p_{c2}, \tag{13}$$

$$R_{2.5}(I) = r_2(H)|\tau_{2.5}|^{q_2} + M_2(H)|\tau_{2.5}|^{3q_2} I^2, \quad p < p_{c2}. \tag{14}$$

Consider now the case of very strong inhomogeneity. We neglect the current through the poorly conductive phase above the percolation threshold and the voltage across the highly conductive phase under the threshold. Substituting (10) and (5) into (13) and (14), one finds

$$R_{2.5}^e(I) = r_{2.5}^e(H) + M_{2.5}^e(H) I^2, \tag{15}$$

where

$$\begin{aligned} r_{2.5}^e(H) &= a_0^{-1} \rho_1 (H/a_0)^{(t_3 - t_2 - \nu_3)/\nu_3} \tau_3^{-t_2}, \\ M_{2.5}^e(H) &= a_0^{-5} \mu_1 (H/a_0)^{(t_3 - t_2 - \nu_3)/\nu_3} \tau_3^{-t_2} \end{aligned} \tag{16}$$

above the percolation threshold and

$$\begin{aligned} r_{2.5}^e(H) &= a_0^{-1} \rho_2 (H/a_0)^{(q_2 - q_3 - \nu_3)/\nu_3} |\tau_3|^{q_2}, \\ M_{2.5}^e(H) &= a_0^{-5} \mu_2 (H/a_0)^{3(q_2 - q_3 - \nu_3)/\nu_3} |\tau_3|^{3q_2} \end{aligned} \tag{17}$$

below the threshold.

If we neglect the threshold shift then the linear film resistance found in [17] will coincide with our expressions. Note that, in [17], $r_{2.5}^e$ was found with quite a different approach, the so-called "percolative renormalization group" technique.

CALCULATIONS OF RESISTANCE FOR NONLINEAR FILMS TAKING INTO ACCOUNT THE SHIFT OF PERCOLATION THRESHOLD

Up till now, we have not taken into account the shift of the percolation threshold for cubes with a size $H \ll \xi$. According to [23, 24], the percolation threshold averaged over possible realizations $\langle p_{cH} \rangle$ is shifted with respect to p_{c3} by a value proportional to τ_H:

$$\langle p_{cH} \rangle = p_{c3} + A\tau_H, \tag{18}$$

where A is a constant.

With such a definition of the shift $\langle p_{eH} \rangle$, it is necessary to take into account the numerical factor (denoted B in [24, 25]) in the root-mean-squared fluctuation of the percolation threshold; instead of (4), we thus have

$$P_H = p - p_{c3} + (B - A)\tau_H / 2B\tau_H. \tag{19}$$

Relationship (19) coincides with (4) at $A = 0$ and $p_{c3}/B = 1$. The closeness to the film percolation threshold with regard for refined concentration (19) can be written as

$$\tau_{2.5} = \left(p_{c3}\frac{\tau_3}{\tau_H} - A\right)/B. \tag{20}$$

At $\tau_3 \longrightarrow 0$, the closeness to the percolation threshold becomes equal to A/B and not zero, in contrast to (5). Depending on τ_3, $\tau_{2.5}$ takes the following values:

$$\text{I} \ \tau_{2.5} = p_{c3}\frac{\tau_3}{B\tau_H} \ \text{at} \ 0 < \tau_c < \tau_3, \quad \tau_c = A\tau_H/p_{c3}, \tag{21}$$

$$\text{II} \ \tau_{2.5} = -\frac{A}{B} \ \text{at} \ 0 < \tau_3 < \tau_c, \tag{22}$$

$$\text{III}\ \tau_{2.5} = -p_{c3}\frac{\tau_3}{B\tau_H} \quad \text{at} \quad |\tau_3| > \tau_c, \tag{23}$$

$$\text{IV}\ \tau_{2.5} = (p_{c3}\frac{\tau_3}{\tau_H} - A)/B \approx 0 \quad \text{at} \quad \tau_3 \approx \tau_c. \tag{24}$$

In cases I and III, the film resistance coincides with (16) and (17), respectively, with an accuracy to the constant B. In case II, the film resistance is given by

$$\begin{aligned} r^e_{2.5}(H) &= C_1 a_0^{-1}\rho_2(H/a_0)^{-(q_3+\nu_3)/\nu_3}, \\ M^e_{2.5}(H) &= C_2 a_0^{-5}\mu_2(H/a_0)^{3(q_3+\nu_3)/\nu_3}, \end{aligned} \tag{25}$$

where the factors C_i are the product of A and B to certain powers.

In case IV, the film is in the smear region with a width $\Delta_{2.5} = (\rho_1/\rho_2)^{1/(t_2+q_2)}(H/a_0)^{(t_3+q_3)/\nu_3(t_2+q_2)}$. For $|\tau_{2.5}| \le \Delta_{2.5}$, its resistance is given by (13) or (14). At $\tau_{2.5} = \Delta_{2.5}$, we have

$$\begin{aligned} r^e_{2.5}(H) &= a_0^{-1}\rho_2\sqrt{h}(H/a_0)^{-(1+\frac{3q_3+t_3}{2\nu_3})}, \\ M^e_{2.5}(H) &= a_0^{-5}\mu_2 h^{\frac{3q_2}{t_2+q_2}}(H/a_0)^{-3(1+\frac{3q_3+t_3}{2\nu_3})}. \end{aligned} \tag{26}$$

Here, we took into account that $t_2 = q_2$.

CONCLUSION

To qualitatively illustrate the behavior of the film resistance, it is convenient to substitute the numerical values of the critical exponents into the expressions derived above. From [26], $t_3 = 2.0$, $t_2 = q_2 = 1.3$, $q_3 = 0.73$, and $\nu_3 = 0.88$. Using these values without taking into account the shift of the percolation threshold [see (16)], we find

$$r^e_{2.5}(H) \propto \rho_1 a_0^{-0.8}H^{-0.2}, \quad M^e_{2.5}(H) \propto \mu_1 a_0^{-4.8}H^{-0.2} \tag{27}$$

above the percolation threshold and

$$\begin{aligned} r^e_{2.5}(H) &\propto \rho_2 a_0^{-0.65}H^{-0.35}, \\ M^e_{2.5}(H) &\propto \mu_2 a_0^{-5.95}H^{-1.06} \end{aligned} \tag{28}$$

below it [see (17)].

If the shift of the percolation threshold is taken into account, we obtain [see (25)]

$$r^e_{2.5}(H) \propto \rho_2 a_0^{0.83}H^{-1.83}, \quad M^e_{2.5}(H) \propto \mu_2 a_0^{0.49}H^{-5.49} \tag{29}$$

for case II (22) and

$$\begin{aligned} r^e_{2.5}(H) &\propto \sqrt{\rho_1\rho_2}H^{-3.38}, \\ M^e_{2.5}(H) &\propto \mu_2(\rho_1/\rho_2)^{3/2}a_0^{5.14}H^{-10.14} \end{aligned} \tag{30}$$

in case IV [see (26)].

Note that $r^e_{2.5}(H)$ and $M^e_{2.5}(H)$ depend on H and a_0 in a different way. Therefore, a simultaneous change in H and a_0 by the same factor does not leave $r^e_{2.5}(H)$ and $M^e_{2.5}(H)$ unchanged. As a result, a change in the "coarseness" (size) of highly conductive particles gives rise to a nontrivial variation of the TFR resistance.

A large number of influencing parameters (τ, Δ, r_1/r_2, μ_1/μ_2, H, etc.) give rise to a great variety of resistance curves for 2.5D films. In experiments, however, additional "degrees of freedom" may be needed. For example, a large difference in particle sizes may require the application of the so-called Swiss Cheese model [26] or the inclusion of tunneling processes. This would necessitate solving problems with an exponentially broad spectrum of resistances [25, 26], etc. The role of these factors calls for separate discussion.

ACKNOWLEDGMENTS

This work was supported by grant KBN Z/7/2/97.

REFERENCES

1. A. Dziedzic, Microelectron. Reliab. **31**, 549 (1991).
2. I. A. Chaĭkovskiĭ, Mikroélektronika **17**, 291 (1988).
3. S. Kasukabe and M. Taketa, Electrocomponent Sci. Technol. **8**, 167 (1981).
4. A. Dziedzic, J. Kita, and P. Mach, Vacuum **50**, 125 (1998).
5. P. F. Carcia, A. Ferretti, and A. Suna, J. Appl. Phys. **53**, 5282 (1982).
6. A. Kubovy, J. Phys. D: Appl. Phys. **19**, 2171 (1986).
7. P. F. Carcia, A. Suna, and W. D. Childers, J. Appl. Phys. **54**, 6002 (1983).
8. A. Dziedzic, K. Nitsch, and A. Kolek, in *Proceedings of 11th European Microelectronics Conference* (1997), p. 622.
9. J. Kubat, R. Kuzel, I. Krivka, *et al.*, Synth. Met. **54**, 187 (1993).
10. M. B. Weissman and C. D. Dollinger, Appl. Phys. (Berlin) **52**, 3095 (1987).
11. M. A. Dubson, Y. C. Hui, M. B. Weissman, *et al.*, Phys. Rev. B: Condens. Matter **39**, 6807 (1989).
12. Y. Yagil, G. Deutscher, and D.J. Bergman, Int. J. Mod. Phys. B **7**, 3353 (1993).
13. A. A. Snarskiĭ, A. E. Morozovsky, A. Kolek, *et al.*, Phys. Rev. E **53**, 5596 (1996).
14. J. P. Clerc, G. Giraud, S. Alexander, *et al.*, Phys. Rev. B: Condens. Matter **22**, 2489 (1980).
15. M. Gadenne and P. Gadenne, Physica A **157**, 344 (1989).
16. P. Gadenne, Y. Yagil, and G. Deutscher, Physica A **157**, 279 (1989).
17. A. V. Neĭmark, Zh. Éksp. Teor. Fiz. **98**, 611 (1990) [Sov. Phys. JETP **71**, 341 (1990)].

18. P. Gadenne, M. Gadenne, Y. Yagil, *et al.*, Physica A **207**, 228 (1994).
19. A. E. Morozovskiĭ and A. A. Snarskiĭ, Zh. Éksp. Teor. Fiz. **109**, 674 (1996) [JETP **82**, 361 (1996)].
20. A. E. Morozovskiĭ and A. A. Snarskiĭ, Int. J. Electron. **78**, 135 (1995).
21. A. L. Efros and B. I. Shklovskiĭ, Phys. Status Solidi B **76**, 475 (1976).
22. D. Stroud and P. M. Hui, Phys. Rev. B: Condens. Matter **37**, 8719 (1988).
23. A. E. Morozovskiĭ and A. A. Snarskiĭ, Zh. Éksp. Teor. Fiz. **95**, 1844 (1989) [Sov. Phys. JETP **68**, 1066 (1989)].
24. M. E. Levinshteĭn, B. I. Shklovskiĭ, M. S. Shur, *et al.*, Zh. Éksp. Teor. Fiz. **69**, 386 (1975) [Sov. Phys. JETP **42**, 197 (1975)].
25. B. I. Shklovskiĭ and A. L. Efros, *Electronic Properties of Doped Semiconductors* (Nauka, Moscow, 1979).
26. D. Stauffer and A. Aharony, *Introduction to Percolation Theory*, 2nd ed. (Taylor and Francis, London, 1992).

Translated by K. I. Kugel

Technical Physics, Vol. 45, No. 3, 2000, pp. 339–342. Translated from Zhurnal Tekhnicheskoĭ Fiziki, Vol. 70, No. 3, 2000, pp. 52–55.
Original Russian Text Copyright © 2000 by Shikhaliev.

SURFACES, ELECTRON AND ION EMISSION

X-ray-Induced Secondary Electron Emission in Porous Materials

P. M. Shikhaliev
Ioffe Physicotechnical Institute, Russian Academy of Sciences,
Politekhnicheskaya ul. 26, St. Petersburg, 194021 Russia

Received April 15, 1998

Abstract—Electron emission induced by X-ray radiation in secondary-emission porous materials was investigated. © *2000 MAIK “Nauka/Interperiodica”.*

Secondary-emission porous materials are widely used as a working substance in electromagnetic and corpuscular radiation detectors [1–5]. The detection process in this case is governed by the interaction between primary radiation and a porous material, fast-primary-electron and slow-secondary-electron emissions, as well as by avalanche generation and transfer of secondary electrons.

The use of secondary-emission materials in detecting X-ray radiation poses certain difficulties. First, the possibility of the X-quantum–porous medium interaction may be low; and second, X-ray-induced emission is ambiguously related to structure parameters (pore size, pore wall thickness, and pore shape), the chemical composition of the material, and the quantum energy [5–8]. Optimization of the detector performance (in particular, sensitivity improvement) implies the elaboration of a model for X-ray-induced electron emission in porous materials.

In [6–8], electron emission in porous materials was considered for the case of a microchannel plate (MCP) to determine its sensitivity to X-ray radiation. However, the authors used simplified models and failed to discover the effect of the material structure and composition, as well as radiation energy, on the emission.

In this work, we suggest a model of X-rays-induced secondary emission in porous materials with both channel-like and closed pores. The study of closed-pore materials seems to be topical in the context of the development of porous insulator technology [2] and a new type of secondary-emission material—microspherical plates [9]. Our model takes into account all structure and composition parameters of the material and possible quantum energies.

The probability P of photon-induced electron emission in a porous body is given by

$$P = P_1 P_2, \tag{1}$$

where P_1 is the probability of quantum–body interaction and P_2 is the probability that a photogenerated or Compton electron will escape from the wall of a pore into the free space.

The probability P_1 is found from the exponential expression [10]

$$P = 1 - \exp(-\bar{\mu} L), \tag{2}$$

where L is the sample thickness and $\bar{\mu}$ is the mean attenuation coefficient of X-rays in the sample. With regard for porosity,

$$\bar{\mu} = \mu \frac{\bar{\rho}}{\rho}. \tag{3}$$

Here, $\bar{\rho} = \rho(1 - V_0/V)$ is the mean density of the material, ρ is the density of the material, μ is the attenuation coefficient of X-rays in the material, V_0 is the pore volume, and V is the total volume of the sample.

It can be shown [11] that

$$\frac{V_0}{V} = \frac{\alpha}{(1 + w/d)^n}, \tag{4}$$

where $n = 2$ or 3 for channel-like and closed pores, respectively; α is a pore-shape-dependent parameter; and w and d are the mean thickness of the pore wall and the mean pore size.

In view of (3) and (4), we find from (2):

$$P = 1 - \exp\left[-\mu L\left(1 - \frac{\alpha}{(1 + w/d)^n}\right)\right]. \tag{5}$$

The probability P_2 that a fast electron will escape from the wall of a pore into the free space depends on the mean distance from the point of electron generation to the pore surface, electron energy, and chemical composition of the body. Let the mean path of electrons in the wall be x_0. To find the escape probability, consider a layer of thickness x_0 where N_0 uniformly generated monoenergetic primary electrons move isotropically.

One can show that the number of electrons leaving this layer is [11]

$$N = N_0\int_0^{x_0}\frac{x}{x_0}dx\int_x^R(1/r^2 + 1/rR)dr. \qquad (6)$$

Here, R is the extrapolated range of electrons in the material (it can be found from Tabata's semiempirical equation [12]) and the probability that electrons will pass through an r-thick layer is linearly approximated as $1 - r/R$ [10]. From (6), we obtain the probability P_{21} that a primary electron will leave the wall:

$$P_{21}(x_0) = \frac{N(x_0)}{N_0} = \begin{cases} 1 - \dfrac{3x_0}{4R} + \dfrac{x_0}{2R}\ln\dfrac{x_0}{R} & \text{at } R > x_0 \\ \dfrac{R}{4x_0} & \text{at } R < x_0. \end{cases}$$

If all primary electrons move normally to the surface,

$$P_{22}(x_0) = \begin{cases} 1 - \dfrac{x_0}{2R} & \text{at } R > x_0 \\ \dfrac{R}{2x_0} & \text{at } R < x_0. \end{cases}$$

Primary photogenerated and Compton electrons have known emission-angle distributions, and the true probability $P_2(x_0)$ of their emission lies between $P_{21}(x_0)$ and $P_{22}(x_0)$. It follows from this condition that the dependence $P_2(x_0)$ can be approximated by the exponential function

$$P_2(x_0) = \exp(-kx_0)$$

more convenient for analysis. Here, k has the meaning of absorption coefficient of electrons and obeys the condition $\ln 2 < kR < \ln 4$.

The value of k can be found from the well-known empirical expression [10]

$$k = 17E^{-1.42}, \qquad (7)$$

which was derived for the absorption coefficient of unidirectional β-electrons with a continuous energy spectrum and a mean energy equal to the mean energy of primary electrons.

The mean path of electrons in the wall depends on the pore size, pore shape, and pore wall thickness. It can be given by [11]

$$x_0 = \beta d[(1 + w/d)^n - \gamma], \qquad (8)$$

where β and γ are parameters dependent on pore shape and arrangement.

Thus, the probability P_2 that primary electrons will escape from the wall into the free space is

$$P_2 = \exp[-\beta kd((1 + w/d)^n - \gamma)]. \qquad (9)$$

Note that μ and k in (5) and (9) depend on the X-quantum energy and the composition of the porous body according to known laws. Hence, the derived expression for the probability P_1P_2 of radiation-induced emission of fast electrons in a porous body takes into account all structure and composition parameters of the material and the X-quantum energy. From (5) and (9), it is easy to see that P_1P_2 plotted against w and d exhibit maxima. The dependence of P_1P_2 on quantum energy also peaks if the empirical expression for μ

$$\mu(E) = C\exp(-3.5E)\ [10]$$

is included in (5).

When fast primary electrons traverse the pores, transmission and reflection secondary electron emissions arise. The number of generated slow secondary electrons is related to the secondary emission coefficient of the material [13] and the number of pores traversed by a primary electron. The latter is expressed as $N = R/x_0$, where R and x_0 are, as previously, the extrapolated range and the mean path of primary electrons in the wall.

Among currently available porous materials, MCPs, including those with channel-like pores, are of most interest for applications. First, MCP parameters can be optimized to obtain the maximum X-rays-induced electron emission and the maximum sensitivity of MCP detectors. Second, the MCP measured sensitivity can be compared with calculated values. In Figs. 1a and 1b, calculated relative emissions in the MCP are plotted against the structure parameters.

It is known that the efficiency of X-quantum detection by an MCP detector depends on the probability that fast primary electrons will be generated and emitted into MCP channels. Calculated (within the suggested model) and experimental [6] efficiencies of the MCP detector vs. X-quantum energy are depicted in Fig. 2.

The MCP material (lead glass) consists of Si, Pb, and O to the extent of 95%. Their relative content may vary within wide limits. These elements, however, enter into the composition as compounds (SiO_2 and PbO) rather than as individual components. Therefore, the weight fraction of one of them (say, lead) specifies those of the other two. This makes it possible to set a correlation between the photo-induced emission in an MCP and the content of one constituent [14]. Figure 3 shows the fast electron emission vs. lead percentage in the MCP material.

With expressions derived for photon-induced electron emission in porous materials, we estimated the efficiency of MCP detectors studied in our previous

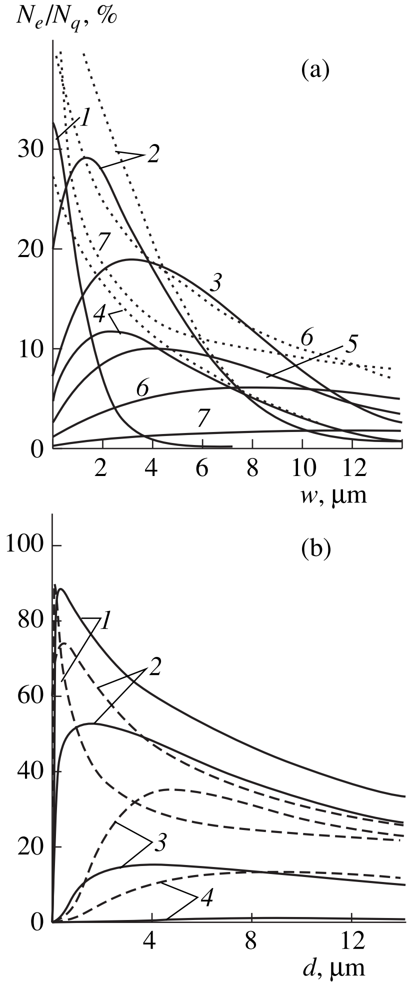

Fig. 1. (a) Relative photon-induced emission of fast (solid lines) and slow (dotted lines) electrons in the MCP vs. channel wall thickness w; channel diameter d = 15 µm: (*1*) 25, (*2*) 40, (*3*) 60, (*4*) 122, (*5*) 150, (*6*) 250, and (*7*) 662 keV. (b) Relative photon-induced emission in the MCP vs. channel diameter d: w = (*1*) 0.1, (*2*) 0.5, (*3*) 1.5, and (*4*) 5.0 µm; solid line, 25 keV; dashed line, 40 keV. L = 1 mm, MCP thickness; N_e and N_q, the number of electrons and quanta, respectively.

work [3] and elsewhere [7, 8, 15]. Analytic values were compared with experimental data (Fig. 4).

It was found that today's MCP parameters used in detecting X-rays are not optimum. Their optimization with the suggested model may greatly improve MCP sensitivity to X-ray radiation.

It should be noted that our procedure for photon-induced electron emission characterization is also applicable to other porous materials, such as porous insulators and microspherical plates. The latter are a new secondary-emission substance [9], namely, a ~1-mm-thick plate with closely packed glass microspheres of diameter ~40 µm inside. The spheres are covered by a special film with a high secondary emission coefficient. Microspherical plates differ from

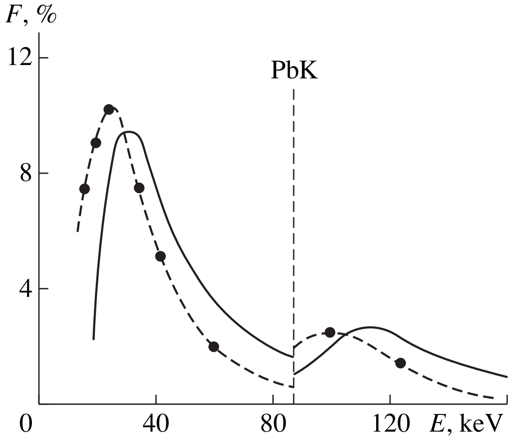

Fig. 2. Analytic (solid line) and experimental (dashed line) dependences of the efficiency of the MCP X-ray detector vs. X-quantum energy.

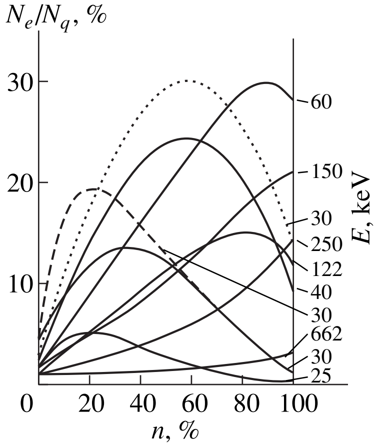

Fig. 3. Relative photon-induced emission of fast electrons against the lead percentage n in the MCP materials; d = 15 µm. Solid lines: L = 1 mm, w = 3 µm; dashed line: L = 3 mm, w = 3 µm; dotted line: L = 1 mm, w = 1 µm.

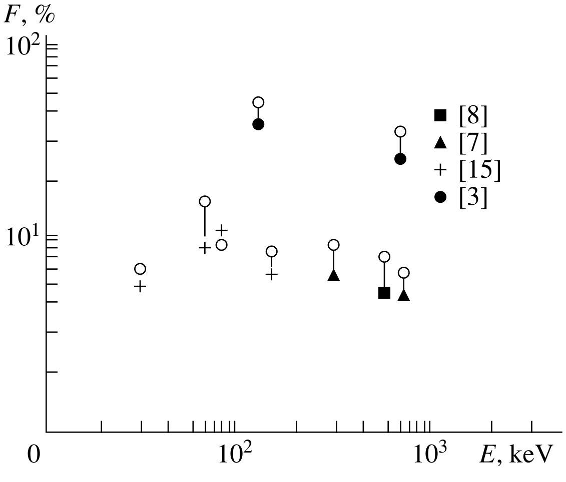

Fig. 4. Calculated (empty circles) and experimental values of the efficiency F of the MCP X-ray detector for different quantum energies E.

MCPs in that avalanche generation of secondary electrons takes place between the spheres.

ACKNOWLEDGMENTS

The author is indebted to B. A. Mamyrin for valuable discussions.

REFERENCES

1. C. Chianelli, P. Aregon, J. Boulet, *et al.*, Nucl. Instrum. Methods Phys. Res., Sect. A **273**, 245 (1988).
2. M. P. Lorikyan, Usp. Fiz. Nauk **165**, 1323 (1995).
3. P. M. Shikhaliev, Rev. Sci. Instrum. **67**, 700 (1996).
4. P. M. Shikhaliev, Nucl. Instrum. Methods Phys. Res., Sect. A **379**, 307 (1996).
5. G. W. Fraser, Nucl. Instrum. Methods Phys. Res., Sect. A **221**, 115 (1984).
6. J. E. Bateman, Nucl. Instrum. Methods Phys. Res., Sect. A **144**, 537 (1977).
7. J. Adams, Adv. Electron. Electron Phys. **22A**, 139 (1966).
8. W. T. A. McKee, A. C. Duffy, W. B. Feller, *et al.*, Nucl. Instrum. Methods Phys. Res., Sect. A **310**, 255 (1991).
9. A. S. Tremsin, J. E. Pearson, J. E. Lees, *et al.*, Nucl. Instrum. Methods Phys. Res., Sect. A **368**, 719 (1996).
10. K. Zigban, *Alpha-, Beta-, and Gamma-Spectroscopy* (Atomizdat, Nauka, 1969).
11. P. M. Shikhaliev, Candidate's Dissertation (St. Petersburg, 1998).
12. T. Tabata, R. Ito, and S. Okabe, Nucl. Instrum. Methods Phys. Res. **103**, 85 (1972).
13. L. G. Dobretsov and M. V. Gamayunova, *Emission Spectroscopy* (Nauka, Moscow, 1966).
14. P. M. Shikhaliev, Rev. Sci. Instrum. **68**, 3676 (1997).
15. R. J. Gould, P. F. Judy, and B. E. Bjarngard, Nucl. Instrum. Methods Phys. Res. **144**, 493 (1977).

Translated by V. A. Isaakyan

Technical Physics, Vol. 45, No. 3, 2000, pp. 343–348. Translated from Zhurnal Tekhnicheskoĭ Fiziki, Vol. 70, No. 3, 2000, pp. 56–61.
Original Russian Text Copyright © 2000 by Suvorov, Cheblukov, Lazarev, Bobkov, Popov, Babaev.

EXPERIMENTAL INSTRUMENTS AND TECHNIQUES

Field Ion and Scanning Tunnel Microscopy Studies of Surface and Bulk Defects in Carbon and Silicon

A. L. Suvorov, Yu. N. Cheblukov, N. E. Lazarev, A. F. Bobkov,
M. O. Popov, and V. P. Babaev

Institute of Theoretical and Experimental Physics, Bol'shaya
Cheremushkinskaya ul. 25, Moscow, 117259 Russia

Received September 28, 1998

Abstract—Complex study of surface and bulk defects was performed by field ion and scanning tunnel microscopy. Specimens were irradiated by 20- to 50-keV He^+, Ar^+, and Bi^+ ions at room temperature. The irradiation fluences were between 10^{18} and 10^{20} ion m^{-2}. Calculated parameters of depletion zones and atomic displacement cascades were compared with theoretical estimates. It was shown that controlled ion bombardment of material surface is an effective tool for fabricating field-emission cathodes for vacuum microelectronics. © *2000 MAIK "Nauka/Interperiodica".*

INTRODUCTION

Although two advanced, extremely sensitive and powerful methods for solid surface analysis—field ion microscopy (FIM) [1] and scanning tunnel microscopy (STM) [2]—differ essentially in several facets, they are often thought of as related techniques naturally complementing each other. STM issues were included in the agenda of the annual International Field Emission Symposium (its 45th meeting was held in 1998), together with FIM, field-emission microscopy, and quantum mechanical processes under high electric fields, immediately after STM discovery (see, for example, [3, 4]). Moreover, several combined instruments that implement both techniques have been produced to date [5].

FIM and STM have the following features in common: atomic resolution, the use of the field emission phenomenon, and the application of tips to generate fields of an appropriate strength. The fundamental difference is that, in FIM, a tip is essentially a specimen, while in STM, it is a probe that scans the surface of a flat specimen. Both techniques provide an atomic resolution of surface images from conducting materials; in the case of FIM, however, the use of field evaporation makes it possible to take images from many (tens or hundreds of) surface atomic layers, visualizing the bulk of a material. This is impossible with STM. Finally, modern field-ion microscopes are equipped with an attachment for probe mass-spectrometric chemical analysis of surface particles [6]. In this respect, an atomic-probe ion-field microscope is a true cluster that integrates two complementary techniques to study different properties of the same specimen. In the case of an STM–FIM cluster, an ion-field microscope plays an essential yet secondary role of a probe-quality analyzer.

The list of similarities and differences between FIM and STM can be extended. Considering the potentialities of both, we have come to the conclusion that they do complement each other and, when used in tandem, are appropriate in investigating radiation-induced defects both on the surface and in the bulk of conducting materials. Note that such studies are routine for the FIM technique [7, 8]; as to STM, relevant data are very scarce (see, for example, [9, 10]).

This article opens a series of related publications concerned with FIM and STM investigations that were performed from December 1, 1997, to November 30, 1999.

SPECIMENS

Specimens were made of carbon (graphite) and silicon. Note that FIM and STM substantially differ by specimen preparation and analytical procedures involved. With this in mind, we selected materials more appropriate for STM analysis, since invoking this technique for the study of radiation-induced defects was among the primary goals of this work.

FIM specimens were tips with a mean radius of curvature of about 100.0 nm. Silicon specimens and specimens of MPG-6 high-strength reactor graphite [11] were prepared by conventional electrochemical etching of small bars with a cross section of 0.3×0.3 mm. The bars were precut by an electric spark method.

STM specimens were thin plane-parallel one-side-polished platelets measuring $10.0 \times 10.0 \times \sim 0.5$ mm. Silicon specimens were prepared from KDB-12 (boron-doped, resistivity 12 Ω cm) Si(100) wafers. Since the instrument operated in air, the specimens were passivated in an HBF_4 solution [12] to prevent their oxidation. After such a treatment, the silicon surface remained clean for 30 h.

SPECIMEN IRRDIATION

Specimens preexamined in the microscope were irradiated by 20- to 50-keV He^+, Ar^+, and Bi^+ ions outside the instruments. The fluences varied between 10^{18} and 10^{20} m^{-2}. In the case of the tips, the bombarding beam was perpendicular to their axis of symmetry. The plates for STM investigation were bombarded normally to their surface.

FIM RESULTS

We noted above that carbon and silicon are difficult to study with FIM. The major challenge here is that the evaporating fields are relatively low and that evaporation is an irregular process. Hence, the poor quality of FIM images and the impossibility of identifying individual point defects and their clusters of a low multiplicity. Yet, FIM images from these materials allow the identification of small pores and sometimes depleted zones (as a result of atomic displacement cascades [13]), as well as the determination of their parameters, such as size, volume, geometry, and approximate vacancy concentration in them. Under favorable conditions, defects like dislocations can be identified and characterized.

In this work, experiments were preformed with a vacuum ion-field microscope at the Institute of Theoretical and Experimental Physics. During examinations, specimens were kept at 78 K, and helium was used as an imaging gas. In the experiments, we took

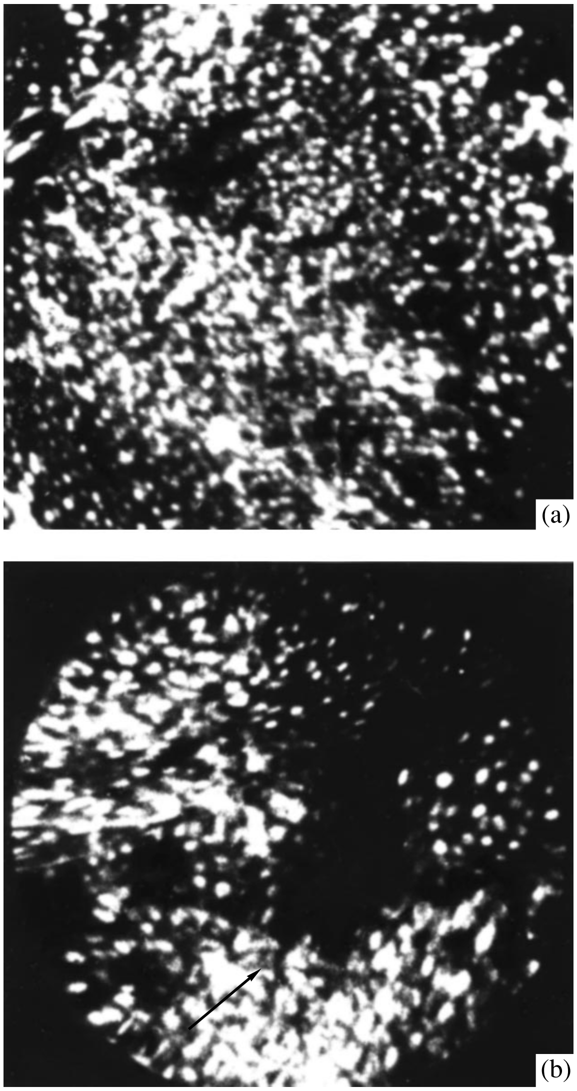

Fig. 1. FIM images from the (a) reference and (b) Ar^+-irradiated (50 keV) specimens of MPG-6 high-strength reactor graphite. The irradiation fluence is 10^{18} m^{-2}.

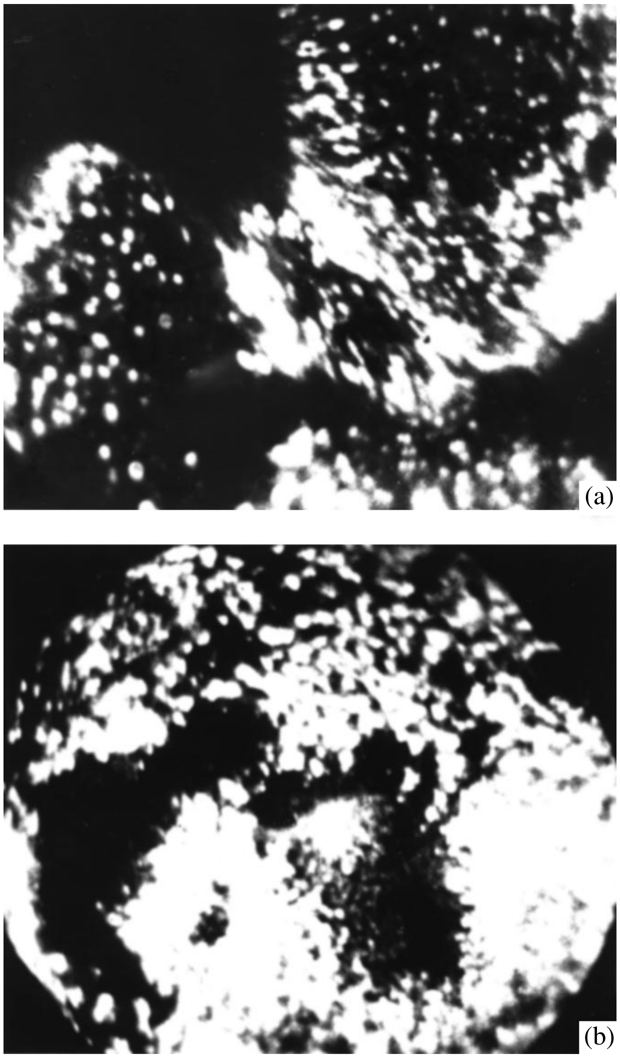

Fig. 2. FIM images from the silicon specimens irradiated by (a) 40-keV Ar^+ ions and (b) 30-keV Bi^+ ions. The fluence is $\geq 10^{20}$ m^{-2} in both cases.

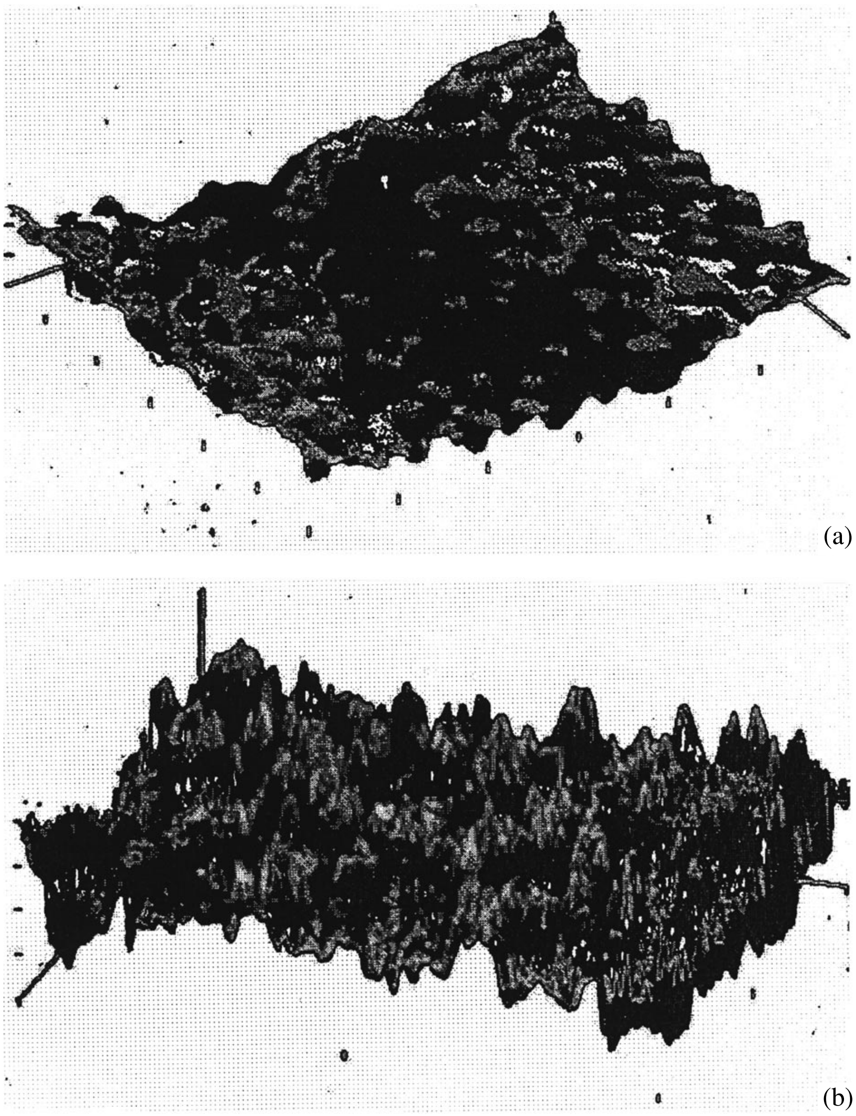

Fig. 3. STM images from the (a) reference and (b) Ar^+-irradiated (50 keV) specimens of MPG-6 reactor graphite. The irradiation fluence ~ 10^{20} m^{-2}.

advantage of methodological expedients used in our previous work [14].

Typical FIM images from the surfaces of (a) reference and (b) Ar^+-ion (50 keV) irradiated MPG-6 graphite are depicted in Fig. 1. The irradiation fluence was 10^{18} m^{-2}. The arrow in Fig. 1b indicates a depleted zone. Presumably, it arises when a single atomic-displacement cascade is developed in the crystal lattice. FIM images of the silicon surfaces irradiated by Ar^+ (40 keV) and Bi^+ (30 keV) ions are shown in Figs. 2a and 2b, respectively. The relatively high fluences in both cases ($\geq 10^{20}$ ion/m^2) imply that the observed defect regions correlate to an overlap of many atomic displacement cascades.

Note that, for individual cascades, the parameters of depleted zones could be found only if the defect region could be "opened" and totally traversed during the successive field evaporation of the irradiated specimens.

Tables 1 and 2 list parameters of the depleted zones and cascade functions ν for MPG-6 graphite and silicon, respectively. They were estimated from FIM images. It should be realized that, while the depleted-zone volume was determined fairly accurately (the error is no more than 15%), the vacancy concentration in them, which was estimated according to concepts put forward in [15], is accurate to 50–60%. Accordingly, the tabulated cascade functions ν involve the same error.

Comparing values given in Tables 1 and 2 with those obtained from the simple Khinchin–Pees formula or within the Sneider–Noifeld modified theory [13], one can draw the following conclusion. For carbon (graphite), the experimentally found parameters of atomic dis-

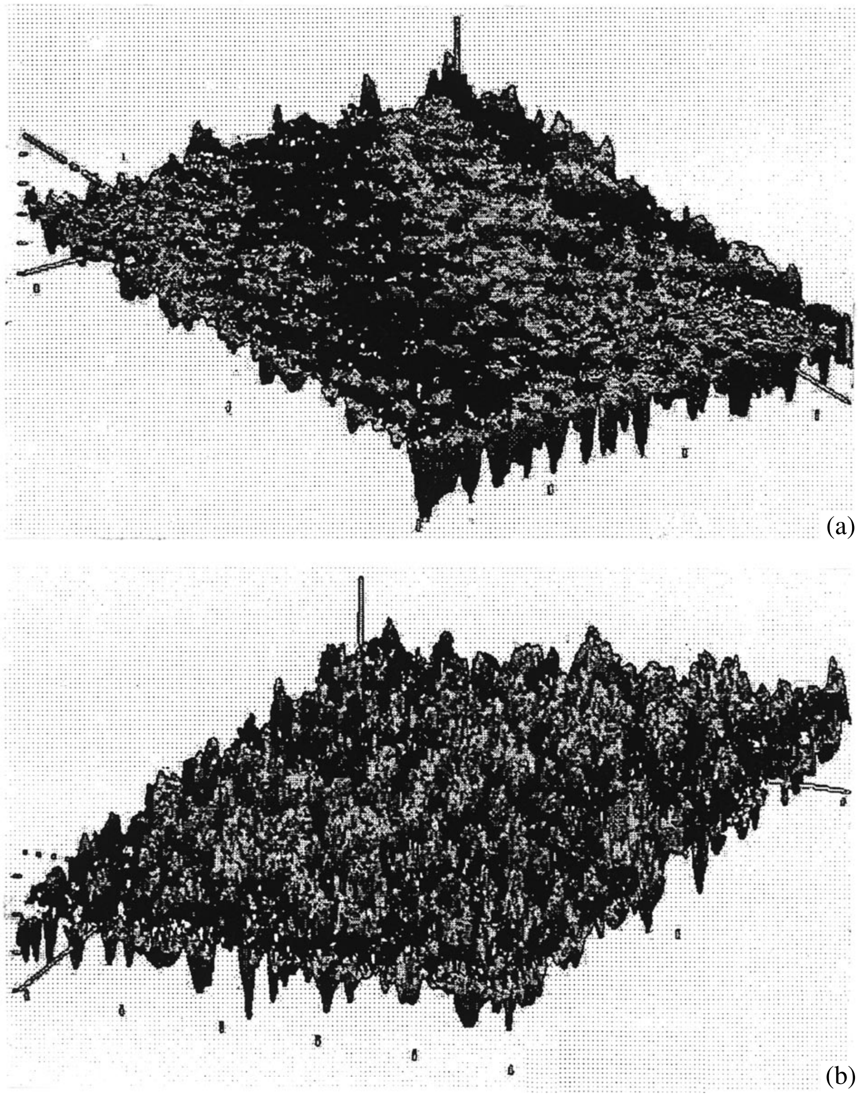

Fig. 4. STM images from the (a) reference and (b) Ar^+-irradiated (50 keV) silicon specimens. The irradiation fluence ~ 10^{20} m^{-2}.

placement cascades are close to theoretical estimates. For silicon, however, the discrepancy may be as high as 80 and even 120%. This can be explained by an error in determining the vacancy concentration in the depleted zones, but only to an extent, since FIM images for carbon and graphite are qualitatively similar. The ultimate answer will be provided once much more experimental data are obtained.

STM RESULTS

Surface roughness of the reference and irradiated specimens was examined in an SMM-2000-T scanning tunnel microscope (KPD, Russia) operating in air. Flat graphite and silicon specimens were irradiated in an ion injector under a high vacuum (at a pressure of 10^{-4} torr). The ions used and their energies are listed in Tables 1 and 2. Since our work was also aimed at developing radiation technology for flat, large-area field-emission cathodes [16], current–voltage characteristics of field emission were taken from several specimens.

Figures 3b (MPG-6 graphite) and 4b (silicon) show rather illustrative, if not quite typical, STM images of the irradiated specimens (Figs. 3a and 4a demonstrate the images of the references). In both cases, the specimens were irradiated by Ar^+ ions (50 keV) at a fluence of ~10^{20} m^{-2}. Under these conditions, the cathode area was the most developed and the current–voltage characteristics (in the Fowler–Nordheim coordinates) were close to those in our previous work [17]. The emission current per cm^2 of the cathode was up to 100 A for graphite and 10 A for silicon at an operating voltage of about 5.0 kV and a flat anode–cathode distance of 1.0 cm (in a diode configuration).

Table 1

Ions	Energy, keV	Atomic volume Ω_e	Approximate vacancy concentration, %	Cascade function ν
He^+	20.0	150	30	45
	30.0	180	30	54
	50.0	540	20	108
Ar^+	30.0	150	30	45
	40.0	350	30	105
	50.0	350	30	105
Bi^+	20.0	15	100	15
	30.0	15	100	15

Table 2

Ions	Energy, keV	Atomic volume Ω_a	Approximate vacancy concentration, %	Cascade function ν
He^+	20.0	15	100	15
	30.0	20	100	20
	50.0	70	30	21
Ar^+	30.0	150	30	45
	40.0	150	30	45
	50.0	240	30	72
Bi^+	20.0	10	100	10
	30.0	15	100	15

Qualitatively, the surface roughness of the irradiated specimens essentially depends on the sputtering coefficient and parameters of atomic displacement cascades. It was found that, the greater the sputtering coefficient and the larger the cascade regions, the more developed the surface (i.e., the higher its roughness). On the other hand, the roughness linearly depends on the fluence within certain intervals. It was shown that there exists a threshold fluence above which the surface roughness of the materials is reduced or at least remains constant.

Using known values of the sputtering coefficients for silicon and carbon exposed to 50-keV Ar^+ ions [18], we made an attempt to locate the initial surface of the irradiated specimens from their STM images.

It was of interest whether the material is merely removed (sputtered) from the surface upon irradiation or some sputtered (more precisely, displaced in atomic collision cascades) surface atoms complete microsteps being formed. It was found that sputtered (removed) atoms amounted up to ~60 and 80–90% in the case of carbon and silicon, respectively.

CONCLUSIONS

(1) A combination of two ultramicroscopic methods, FIM and STM, proves to be reasonable in investigating the effect of radiation on the surface and bulk structures of materials, since it provides additional information.

(2) Scanning tunnel microscopy is an efficient tool for studying radiation-induced surface defects and controlling surface modifications.

(3) The parameters of atomic displacement cascades occurring in MPG-6 high-strength reactor graphite irradiated by moderate-energy ions are close to the existing theoretical estimates.

(4) The parameters of atomic displacement cascades occurring in silicon irradiated by moderate-energy ions greatly differ from the existing theoretical estimates; the experimentally found efficiency of stable atomic displacement in cascades was found to be 80–120% less than the theoretical value. This cannot be explained by the specifics of the used method alone.

(5) At relatively small energies of atomic displacement cascades in graphite and silicon (the energies of primary knocked-out atoms at a level of 1.0–1.5 keV), defect regions of single cascades are pores (depleted zones with a vacancy concentration of 100%).

(6) Upon ion irradiation, the surface roughness essentially depends on the sputtering coefficient and also on the parameters of atomic displacement cascades: the greater the coefficient and the larger the size (the space of development) of the cascades, the higher the roughness. An increase in the irradiation fluence increases the roughness (the degree of surface development) to a certain limit only.

(7) Radiation-induced surface modification of conducting materials is a promising way for producing flat, large-area field-emission cathodes needed in vacuum microelectronics. Conditions for radiation treatment can be optimized by varying the type of bombarding ions and their energy; angle of incidence; radiation density and fluence; and, possibly, the initial stress state and the spectrum of preformed (e.g., by heat treatment) crystal defects.

ACKNOWLEDGMENTS

This work was financially supported by the International Research Center (project no. 467-97 “Atomic Probe Microscopy and Scanning Tunnel Microscopy of Defects and Structural and Phase Transformations in Metals and Alloys under Pulse and Steady-State Irradiation by Energetic Particles”).

REFERENCES

1. E. W. Müller and T. T. Tsong, *Field-Ion Microscopy: Principles and Applications* (Elsevier, New York, 1969; Mir, Moscow, 1972).
2. G. Binnig and H. Rohrer, Rev. Mod. Phys. **59**, 615 (1987).

3. Proceedings of 42nd International Field Emission Symposium, Appl. Phys. Lett. **94–95**, 1 (1996).
4. Proceedings of 43rd International Field Emission Symposium, J. Phys. IV (Paris) **6** (9), 5-5-5-308 (1996).
5. T. Sakurai, T. Hashisume, I. Kamiya, *et al.*, Prog. Surf. Sci. **33**, 3 (1990).
6. M. Miller and G. Smith, *Atom Probe Microanalysis: Principles and Applications to Materials Problems* (Materials Research Society, Oxford (UK), 1989; Mir, Moscow, 1993).
7. A. L. Suvorov, *Field-Ion Microscopy of Radiation-Induced Defects in Metals* (Energoizdat, Moscow, 1982).
8. A. L. Suvorov, *Structure and Properties of Surface Atomic Layers in Metals* (Energoatomizdat, Moscow, 1990).
9. H. Kemmer, S. Grafstrom, M. Neitzert, *et al.*, Ultramicroscopy **42–44**, 1345 (1992).
10. T. Matsukawa, S. Suzuki, T. Fukai, *et al.*, Appl. Surf. Sci. **107**, 227 (1996).
11. *Properties of Carboniferous Structural Materials: A Handbook*, Ed. by V. P. Sosedov (Metallurgiya, Moscow, 1975).
12. V. V. Levenets, V. I. Beklemishev, B. A. Loginov, *et al.*, Jpn. J. Appl. Phys. **34**, 1723 (1995).
13. V. V. Kirsanov, A. L. Suvorov, and Yu. V. Trushin, *Radiation-Induced Formation of Defects in Metals* (Energoatomizdat, Moscow, 1985).
14. D. E. Dolin, A. A. Sosunov, A. L. Suvorov, *et al.*, Zh. Tekh. Fiz. **60** (12), 115 (1990) [Sov. Phys. Tech. Phys. **35**, 1430 (1990)].
15. A. L. Suvorov and A. G. Sokolov, Kristallografiya **20**, 379 (1975) [Sov. Phys. Crystallography **20**, 232 (1975)].
16. I. Brodie and C. Spindt, Adv. Electron. Electron Phys. **83**, 1(1992).
17. A. L. Suvorov, E. P. Sheshin, V. V. Protasenko, *et al.*, Zh. Tekh. Fiz. **66**, 156 (1996) [Tech. Phys. **41**, 719 (1996)].
18. *Sputtering by Particle Bombardment*, Ed. by R. Behrische (Springer, Heidelberg, 1981; Mir, Moscow, 1984).

Translated by V. Isaakyan

Technical Physics, Vol. 45, No. 3, 2000, pp. 349–350. Translated from Zhurnal Tekhnicheskoĭ Fiziki, Vol. 70, No. 3, 2000, pp. 62–63.
Original Russian Text Copyright © 2000 by Shtepa.

BRIEF COMMUNICATIONS

Combined Focusing of an Uncharged Particle Beam by Axially Symmetric Magnetic and Electric Fields in a Vacuum

N. I. Shtepa
Shevchenko State Pedagogical University, Chernigov, 250038 Ukraine

Received September 28, 1998

Abstract—A way of simultaneously focusing a circular uniform beam of fine uncharged diamagnetic particles in the longitudinal and transverse directions is explored. Focusing is performed by a short magnetic lens and a diaphragm providing a time-dependent electric field. The size of the particles is within the range of 10^{-4}–10^{-1} cm. © *2000 MAIK “Nauka/Interperiodica”.*

As is known, transverse (normal) focusing of fine uncharged particles in a vacuum can be performed by a constant axially symmetric magnetic [1] or electric [2] field. The size of the particles varies between 10^{-4} and 10^{-1} cm. It has also been demonstrated [3] that a uniform beam of uncharged particles can be transformed into a stream of clusters that are compressed in the longitudinal direction under the action of an axially symmetric periodic electric field. The clusters are compressed to a maximum degree after they have traveled a certain distance, which can be regarded as the focal distance for longitudinal focusing.

This study addresses combined focusing of an uncharged particle beam, i.e., focusing that is performed in both directions. The approach is hampered by the fact that a time-dependent electric field employed for longitudinal focusing performs time-varying transverse focusing as well. The additional focusing in the transverse direction adversely affects that provided by a constant axially symmetric magnetic or electric field. Although this drawback is inherent in the technique, it is reduced to a large extent if focusing parameters are set appropriately.

Consider combined focusing of a uniform circular beam of fine (10^{-4}–10^{-1} cm) uncharged diamagnetic particles in a vacuum. The focusing system comprises a short magnetic lens ML for transverse focusing and a planar diaphragm D having a fine circular aperture of a given radius R (see figure). The diaphragm generates a time-dependent electric field, thus providing longitudinal focusing. Let the particles move along the axis of symmetry z and have the same initial velocity v_0. The magnetic field $H = H(z)$ is confined to an interval $z_1 \le z \le z_2$, and the electric field of the diaphragm next to ML lies within an interval $z_3 \le z \le z_4$ in the vicinity of the diaphragm. The latter interval is comparable in size to the diaphragm aperture. Outside the interval $z_3 \le z \le z_4$, and the electric field is uniform: $E_3 = 0$ and $E_4 = E = \text{const} \ne 0$ (in a static mode). The electric-field potential is distributed as [4]

$$\Phi(z) = \Phi_0 - \frac{1}{\pi}ER\left(\frac{|z|}{R}\arctan\frac{|z|}{R} + 1\right) - \frac{1}{2}Ez,$$

where Φ_0 is the potential at the diaphragm center ($z = 0$).

Following [3], the electric field along the axis is given by $\varphi = \varphi(z, t)$, i.e.,

$$\varphi(z, t) = \Phi(z)\eta(t),$$

where $\eta = \eta(t)$ is a periodic function with a period T.

The diaphragm field forms clusters, which experience maximum longitudinal compression (at the longitudinal focus) at a distance l ($l \gg Tv_0$) if

$$\eta(t) \simeq A\sqrt{t},$$

where

$$A = \frac{\sqrt{2}\,v_0^{3/2}}{\sqrt{\dfrac{3(\varepsilon - 1)}{4\pi\rho(\varepsilon + 2)}E^2 l}},$$

ρ is the particle density, and ε is the relative permittivity of the particles.

Let the effect of the diaphragm on the transverse focusing be negligible (it is provided by ML alone). Then the focal points F are the same for the magnetic

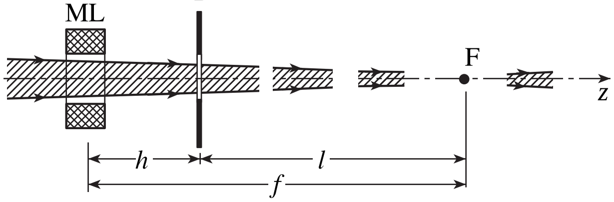

Figure.

1063-7842/00/4503-0349$20.00 © 2000 MAIK “Nauka/Interperiodica”

lens and the diaphragm if $f = l + h$, where f is the focal distance of the magnetic lens and h is the distance between the two elements. At this point, the clusters are most compressed in both directions, so that combined focusing is realized. According to [1],

$$f = \frac{16\pi v_0^2(\mu + 2)\rho}{9(1-\mu)\int\limits_{z_1}^{z_2} H'^2 dz},$$

where $H' = \partial H/\partial z$ and μ is the relative permeability of the particles. The condition for combined focusing therefore becomes

$$\frac{16\pi v_0^2(\mu + 2)\rho}{9(1-\mu)\int\limits_{z_1}^{z_2} H'^2 dz} = \frac{8\pi\rho v_0^3(\varepsilon + 2)}{3(\varepsilon - 1)A^2E^2} + h.$$

Thus, combined focusing can be achieved regardless of the particle size.

Since we have $|z_1 - z_2| \ll f$ and $|z_3 - z_4| \ll l$, the magnetic lens and the diaphragm can be placed so close to each other that $h \ll f, l$, which allows one to assume $h \approx 0$. Then combined focusing is feasible regardless of the particle density as well. However, it should be borne in mind that the focal distance depends on the density $[l = l(\rho)]$ rising with the latter.

The assumption that the effect of the diaphragm on the transverse focusing is negligible is tantamount to

$$\left|\frac{1}{f_0}\right| \ll \frac{1}{f} = \frac{1}{l},$$

where f_0 is the focal distance for transverse focusing performed by the diaphragm.

Since [2]

$$\frac{1}{f_D} \approx -\frac{9(\varepsilon - 1)}{16\pi(\varepsilon + 2)\rho v_0^2}$$

$$\times \int\limits_{z_3}^{z_4} \varphi''^2(z, t)dz \quad (\text{at } \dot{z} \approx v_0)$$

and

$$\frac{1}{l} = \frac{3(\varepsilon - 1)A^2E^2}{8\pi\rho(\varepsilon + 2)v_0^3},$$

we have

$$\left|\frac{1}{f_0}\right| \sim \frac{t}{v_0^2} \text{ and } \frac{1}{l} \sim \frac{1}{v_0^3}.$$

This means that this inequality can be met by decreasing the period T (since $0 \le t \le T$) and the velocity v_0.[1] The effect of combined focusing is also enhanced if E and R are selected optimally, since f_0 and l are variously governed by the electric field distribution.

Finally, note that combined focusing of fine uncharged particles by axially symmetric magnetic and electric fields in a vacuum is possible in a first approximation.

REFERENCES

1. N. I. Shtepa, Zh. Tekh. Fiz. **49**, 1839 (1979) [Sov. Phys. Tech. Phys. **24**, 1034 (1979)].
2. N. I. Shtepa, Zh. Tekh. Fiz. **36**, 470 (1966) [Sov. Phys. Tech. Phys. **11**, 347 (1966–1967)].
3. N. I. Shtepa, Zh. Tekh. Fiz. **48**, 2139 (1978).
4. A. A. Rusterholz, *Elektronenoptik* (Birkhäuser, Basel, 1950; Inostrannaya Literatura, Moscow, 1952).

Translated by A. A. Sharshakov

---

[1] The number of particles in a cluster is proportional to v_0 and T; hence, the above conditions decrease it.

Technical Physics, Vol. 45, No. 3, 2000, pp. 351–352. Translated from Zhurnal Tekhnicheskoĭ Fiziki, Vol. 70, No. 3, 2000, pp. 64–65.
Original Russian Text Copyright © 2000 by Sankin, Teslenko.

BRIEF COMMUNICATIONS

Slow Variation of the Electrical Conductivity of Water under Weak Permanent Magnetic Fields

G. N. Sankin and V. S. Teslenko

Lavrent'ev Institute of Hydrodynamics, Siberian Division, Russian Academy of Sciences,
pr. akademika Lavrent'eva 15, Novosibirsk, 630090 Russia

Received October 19, 1998

Abstract—Slow variation (for 10–40 min) of the electrical conductivity of a water cell in weak permanent magnetic fields was studied. Relaxation characteristics and the dependence of the resistivity on a magnetic field ranging between 0.02 and 0.11 G were obtained. It was found that the cell response lags behind magnetic field switching-on and switching-off. © *2000 MAIK "Nauka/Interperiodica".*

Extralow (comparable to geomagnetic) ac (0.01–200 Hz) magnetic fields are known to influence physicochemical properties of aqueous solutions, water, and ice [1–3]. The electrical conductivity, dielectric loss tangent, refractivity index, and other properties vary within several hours after magnetic treatment.

In this work, we show that below-geomagnetic permanent magnetic fields may reversibly alter the electrical properties of a water-filled cell through which a direct current passes.

Experiments were performed against the magnetic field of the Earth. The mean field strength, its vertical and horizontal components, and the component normal to the electric field of the cell were 0.59, 0.56, 0.17, and 0.58 G, respectively. Geomagnetic fluctuations were not taken into account.

An additional magnetic field was generated by a permanent magnet, a solenoid, or a straight conductor 4.5 cm distant from the center of the cell. In the last case, the field generated at the center of the cell was directed vertically and normally to the electric field of the cell. Hereafter, magnetic field values in the text and in the figures are those at the center of the cell.

The cell was a Teflon cylinder 20 mm in diameter with planar electrodes spaced 5 mm apart. Stainless-steel, titanium, and carbon electrodes were tested. The electrodes were arranged vertically.

The cell was filled with distilled or twice-distilled water (with a conductivity of $4 \times 10^{-6}\ \Omega^{-1}\ \mathrm{cm}^{-1}$). The liquid was exposed to air. Prior to experiments, the water-filled cell settled for a day. Then, the current was passed through the cell for 1 or 2 h until the liquid was completely polarized. The cell was placed in a thermostat made of foamed plastic. A magnetic field source was outside the thermostat. The experiments were performed at temperatures of 21–23°C and 1.3°C. Figures 1 and 2 refer to the cell with stainless-steel electrodes at 21°C.

We used a dc measuring bridge where the cell was one of the branches. The supply voltage of the bridge was constant, 1.5 V. The resulting signal was amplified by a U5-10 differential amplifier and then recorded with an S9-27 digital oscilloscope. The time resolution of the bridge was 0.15 s. The desired effect was observed against a monotone current drift. The drift was taken into account upon processing oscillograms.

Figure 1 shows a current oscillogram for the cell with distilled water when a magnetic field $B = 0.11$ G was generated by the straight conductor. The resistance of the cell increases to a maximum value for a time lag $\tau_L = \tau_1 + \tau_2$ (τ_1 and τ_2 are the delay time and the time of response to field switching-on) and then relaxes to its initial value for a time $\tau_R = \tau_3 + \tau_4$ (τ_3 and τ_4 are the delay time and time of response to field switching-off). For a current through the cell of 0.83 $\mu\mathrm{A/cm}^2$, the resistance increased by about 1% for $\tau_L \approx 20$ min. The delay between field switching-on and the beginning of resistance change was $\tau_1 \approx 5$ min. Once the magnetic field

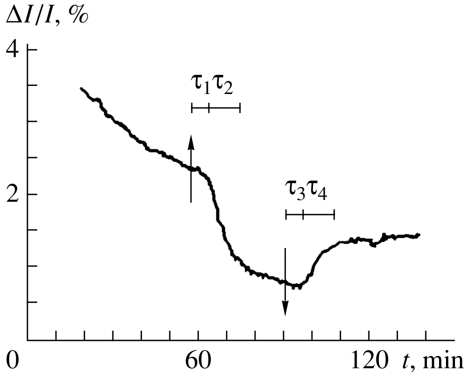

Fig. 1. Time variation of the relative change in the current through the cell in the presence of the additional magnetic field $B = 0.11$ G of the conductor (switching-on and switching-off instants are indicated by arrows).

1063-7842/00/4503-0351$20.00 © 2000 MAIK "Nauka/Interperiodica"

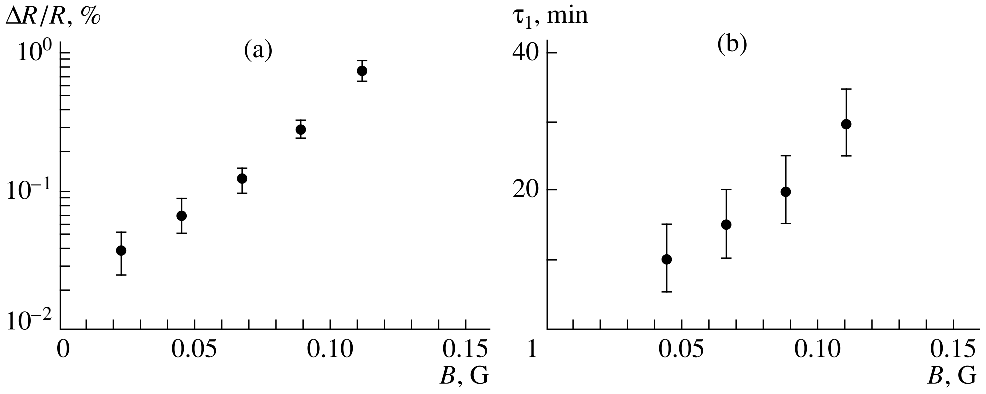

Fig. 2. (a) Relative change in the cell resistance and (b) time τ_L vs. additional magnetic field of the conductor at 21°C.

was switched off, the cell passed into its initial state (with a delay $\tau_3 \approx 5$ min) for a time $\tau_R \approx 20$ min. When the cell was filled with twice-distilled water, the relative current change was the same for the same magnetic field.

Similar effects are observed in the fields of the solenoid and the permanent magnet. When the field of the solenoid, $B = 0.15$ G, was switched on, the current change was 2.5% with $\tau_L \approx 30$ min for a cell current of 1.5 μA/cm^2. An increase in the resistance does not depend on the field polarity. At 1.3°C, the current behaved in a similar way.

In Fig. 2a, the relative change in the resistance of the cell with distilled water is plotted against the applied magnetic field for a cell current of 0.78 μA/cm^2. Figure 2b shows the dependence of the transition time τ_L on the applied magnetic field. The effect also takes place if the magnetic field is aligned with the electric field of the cell and is again independent of the magnetic field direction.

Note that, when the magnetic field is switched off within the time τ_2, an increase in the resistance grows during the time of inertia $\tau_i \le \tau_2$ and, after attaining a maximum, it returns to its initial value in both cases (the magnetic field is parallel or normal to the electric field of the cell).

Thus, by measuring the relative change in water conductivity, we discovered the effect of initiating slow physicochemical processes in an electrolytic cell when extralow magnetic fields are applied. It was found that the cell response lags behind magnetic field switching-on and switching-off.

The effect can be attributed to a change in the degree of impurity-ion (primarily dissolved carbon dioxide) hydration in the bulk of water, probably because of the modified water structure [4]. As a result, the adsorption of ions hydrated on the electrode surfaces changes, causing the reconstruction of the double electrical layer.

ACKNOWLEDGMENTS

The authors thank A. P. Drozhzhin for assistance in performing the experiments and also V. V. Mitrofanov for valuable discussions.

This work was partially supported by the Russian Foundation for Basic Research (grant no. 96-02-19329).

REFERENCES

1. L. P. Semikhina and V. F. Kiselev, Izv. Vyssh. Uchebn. Zaved., Fiz., No. 5, 13 (1988).
2. M. V. Berezin, G. N. Zatsepina, V. F. Kiselev, *et al.*, Zh. Fiz. Khim. **65**, 1338 (1991).
3. V. V. Novikov, Biofizika **39**, 825 (1994).
4. S. F. Timashev, Zh. Fiz. Khim. **64**, 1142 (1990).

Translated by V. A. Isaakyan

Technical Physics, Vol. 45, No. 3, 2000, pp. 353–355. Translated from Zhurnal Tekhnicheskoĭ Fiziki, Vol. 70, No. 3, 2000, pp. 66–68.

BRIEF COMMUNICATIONS

Instrument for Analyzing the Composition of Multicomponent Ion Beams

L. P. Veresov, O. L. Veresov, M. I. Dzkuya, V. V. Dorokhov†, and I. A. Tsekvava
Sukhumi Physicotechnical Institute, Academy of Sciences of the Republic of Abkhazia,
Sukhumi, Abkhazia, 384914 Georgia
Received December 28, 1998

Abstract—A compact multichannel mass analyzer is described, which enables one to analyze the composition of multicomponent ion beams. © *2000 MAIK "Nauka/Interperiodica".*

INTRODUCTION

Beam technologies presently find increased usage in mechanical engineering. New ion sources for these purposes are under development, including sources with a multicomponent (mixed) ion beam. These include ion sputtering sources, whose beams contain ions of working gas in addition to metal ions. In order to determine the composition of ion beams produced by such sources, we have developed and employed a compact multichannel mass analyzer. Small dimensions and mass of the instrument make it possible to employ it even in small vacuum chambers. Thanks to multichanneling, the instrument enables one to determine the mass of ions of all elements of the periodic table and their ratios in the beam.

PRINCIPLE OF OPERATION OF THE INSTRUMENT

As in the case of most mass analyzers, the operation of the instrument is based on the dependence of the radius of turning of charged particles in a transverse uniform magnetic field on their mass and energy according to the equation

$$R = \frac{144 - \sqrt{WM}}{zB},$$

where R is the Larmor radius (cm), W is the particle energy (eV), M is the particle mass (amu), z is the atomic number, and B is the magnetic induction (G) [1].

The distinguishing feature of the instrument consists in the fact that its magnetic field is constant; and ten magnetic tracks are selected in this field with preassigned radii, each track with its own collector. Therefore, only two quantities are variable, namely, the mass of particles and their energy. By varying the particle energy, one can receive the beam jet and measure its current in different collectors, thereby determining the particle mass in the beam or, with fixed energy of the beam, search for its components of different masses in different collectors, which makes it possible to analyze the composition of the beam without varying the operating mode of the ion source being investigated.

INSTRUMENT DESIGN

The uniform magnetic field in the instrument is produced with the aid of magnet poles (see figure). The magnetic gap between the poles is taken to be 5 mm from the considerations that the magnetic field must be as maximum as possible with acceptable resolution of low values of current by the measuring instrument. The magnetic field is realized with the aid of permanent samarium–cobalt exciters $40 \times 40 \times 12$ mm in size with induction on the surface of ≈2 kG. Five piles of two exciters each are installed between the magnet pole and the magnet system yoke closing the external magnetic flux. Therefore, 20 exciters in all are used in the instrument. The magnetic induction in the working magnetic gap is 3500G ± 1.5%. Both magnet poles, each 7 mm thick, are made of magnetically soft iron.

It was decided to use ten magnetic tracks, i.e., radii, in the following sequence: R_1 = 5.2 cm, R_2 = 5.9 cm, R_3 = 9 cm, R_4 = 12 cm, R_5 = 19 cm, R_6 = 29 cm, R_7 = 38 cm, R_8 = 58 cm, R_9 = 86 cm, and R_{10} = 650 cm. Owing to this choice of radii, one could use two or three tracks in the energy range from 5 to 70 keV to determine the mass of some element. The radius R_{10} = 650 cm was selected for recording charged clusters.

All collectors of each track are identical. A collector is a plate bent to form a bracket with parallel walls. The gap between the walls is 3 mm, with a thickness of each wall of 0.3 mm. The collectors are secured on insulators, which make it possible to arrange them on a tangent to a preassigned radius. Each collector is located at a distance of 1 mm from the magnet poles, the scattered field from which (of ≈200 G) extends to cover the collectors. This is sufficient to suppress the secondary electron emission.

---

† Deceased.

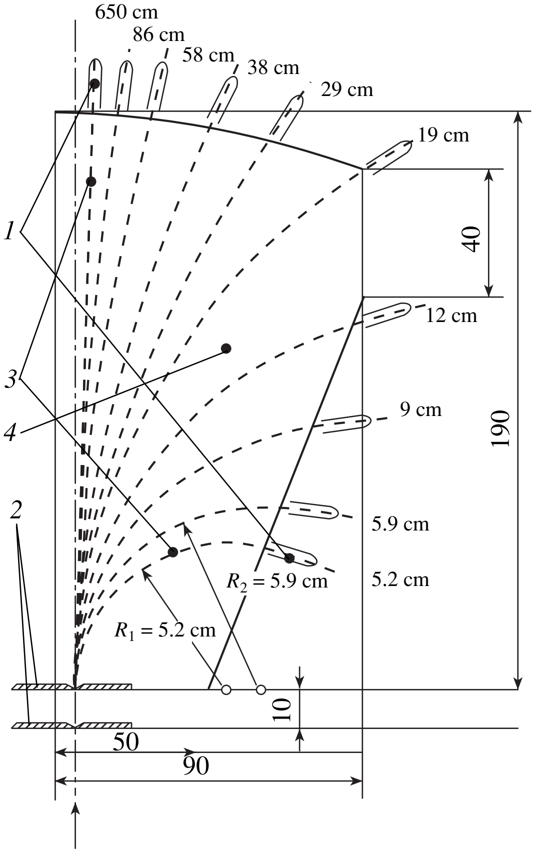

Magnetic pole of the mass analyzer: (*1*) collectors, (*2*) slits for cutting out the beam jet, (*3*) paths of magnetic tracks, (*4*) magnet pole.

Signals from the collectors are measured by an M95 microammeter with a multiple shunt, which permits us to measure currents of up to 10^{-8} A.

Two slits arranged horizontally to the ion beam axis are used to cut from the beam a jet entering the magnetic field of the analyzer. The size of the jet is defined by the gap between the slits and the gap between the magnet poles of the mass analyzer (equal to 5 mm). The gap between the slits may vary. It was experimentally selected to be 0.4 mm. The distance between the first and second slits is 10 mm.

Located on the face of the mass analyzer is a square collector plate insulated from the housing, sized 100 × 100 mm, covering the entire front surface of the instrument and receiving the entire beam. The secondary electron emission from this plate is suppressed by the scattered field of the mass analyzer and by magnetic strips of barium ferrite specially installed for the purpose. The error of measurement of the beam current using this collector does not exceed 15%. The second slit is arranged on this plate at a horizontal distance of 10 mm from the first slit of the mass analyzer and perpendicular to the latter, with a size of 2 × 1 mm and with a collector behind it for measuring the density of the beam current.

The entire instrument is installed in four vertical guides with two adjusting screws for aligning the instrument axis with the beam axis.

ADJUSTMENT OF THE INSTRUMENT

(1) The exactly measured radii of the first and second magnetic tracks ($R_1 = 5.2$ cm and $R_2 = 5.9$ cm) were used to determine the real magnetic field of the mass analyzer.

(2) The inert gases He, Ne, Ar, Kr, and Xe were used as reference masses to exactly determine all of the remaining radii except for the last radius R_{10}.

(3) The resolving power of the mass analyzer was estimated for nitrogen and oxygen by the equation $\Delta m/m = 1/r$, where Δm is the difference between the masses being measured, m is the maximum mass, and r is the resolving power [2] when atmospheric air was used as the working gas in the source. The resolving power proved to be equal to 8.

(4) In some cases in measuring beam components, usually with heavy masses, when the beam jet currents were very low, the current-measuring instrument registered a negative current of the order of 10^{-6}–10^{-7} A. This reading may be attributed to the departure of positive ions from the collector or to the penetration of negative ions into the collector. The latter possibility is ruled out, because negative particles cannot enter the collector in passing through the magnetic field of the mass analyzer. The departure of positive ions from the collector may occur in the case of ion–ion emission and repulsion of bombarding ions. Both these processes are insignificant in magnitude and, in balance with ions migrating to the collector, cannot produce a negative current through the microammeter. Most likely, when a wall plasma is formed in the collector as a result of the processes of gas release, dispersion, neutralization, recombination, secondary electron emission, and others, low-energy positive ions are emitted from this plasma and get onto the housing of the mass analyzer to form a negative current through the current-measuring instrument. In so doing, it becomes impossible to accurately measure the beam jet with the microammeter.

This obstacle may be overcome in two ways, namely, by increasing the width of the mass analyzer slits to increase the beam jet current or by performing calorimetric measurements. The main contribution to the collector heating is made by much higher energy ions arriving at the collector in the beam jet. Their energy is several orders of magnitude higher than that of ions leaving the collector, which provides for an almost exact measurement of energy and, consequently, of the beam jet current, according to the equation

$$I = \frac{cm\Delta T}{Ut},$$

where c is the heat capacity of the collector material, m is the mass of the collector, ΔT is the temperature difference, I is the beam current, U is the particle energy, and t is the time during which the beam affects the collector.

Therefore, with a fixed energy and time during which the beam affects the collector (microcalorimeter), it is only the temperature difference that is measured. Experience suggests that the most acceptable sensor for measuring the temperature difference is provided by a base-emitter transistor *p–n* junction, which retains the linearity of the temperature characteristic in a wide range and a high sensitivity, as distinct from thermocouples and thermal resistors.

CONCLUSIONS

(1) An instrument installed on a moving carriage across the beam axis enables one to measure the total beam current, the distribution of the beam current density, the mass composition of the beam, the ratios of the beam components, and their distribution over the beam cross section.

(2) The small size (20 × 18 × 12 cm) and mass (17 kg) of the instrument make possible its use under simple laboratory conditions.

(3) The recording of currents by a microammeter enables one to perform a rapid analysis of the beam and affect the source operation during the experiment. The calorimetric method of measurement is also prompt, because the temperature difference in the bridge comparison circuit is likewise measured by a microammeter.

(4) The operating experience of the instrument indicates that its resolving power may be increased both by increasing the magnetic field and by increasing the magnetic track length.

The mass analyzer described above proved to be a convenient instrument for the investigation of sources producing multicomponent beams in facilities that are not provided with special separation magnets.

REFERENCES

1. E. V. Shpol'skiĭ, *Atomic Physics* (Nauka, Moscow, 1984), Vol. 1.
2. L. A. Artsimovich and S. Yu. Luk'yanov, *The Motion of Charged Particles in Electric and Magnetic Fields* (Nauka, Moscow, 1972).

Translated by Henri A. Bronstein

Technical Physics, Vol. 45, No. 3, 2000, pp. 356–358. Translated from Zhurnal Tekhnicheskoĭ Fiziki, Vol. 70, No. 3, 2000, pp. 69–71.
Original Russian Text Copyright © 2000 by Smolyakov.

BRIEF COMMUNICATIONS

Invariance of Electromagnetic Radiation Spectra in Undulators Based on Plane Magnets

M. N. Smolyakov

Moscow State University, Vorob'evy gory, Moscow, 119899 Russia

Received January 28, 1999

Abstract—Radiation of relativistic particles in a plane magnetic field (for example, in an undulator) is studied. The magnetic system is assumed to be plane and composed of permanent magnets. It is shown that there is a class of special continuous rotations of the magnetization vector for magnetic substances providing changes in the magnetic field of the system without changing the spectrum of spontaneous radiation of relativistic particles. This property of electromagnetic radiation can be used in developing new models for undulators. *© 2000 MAIK "Nauka/Interperiodica".*

INTRODUCTION

Undulators currently used as sources of magnetic field are usually based on permanent magnets. Two types of undulators are the most widely used: purely rare-earth undulators [1] and undulators of the hybrid type [2, 3]. In some cases, however, undulators of nonconventional design (especially microundulators) are used [4–7]. The purely rare-earth undulator used in the free electron laser described in [8, 9] also has a nonconventional scheme. The alignment of the magnetization vectors of all magnets along the undulator axis causes a significant increase in the amplification coefficient of this undulator. Thus, the problem of studying the general properties of plane undulators based on permanent magnets and the properties of electromagnetic radiation of relativistic electrons in such undulators assumes great importance. In particular, the so-called Rotation Theorem is well known [10]. The theorem states that, if the magnetic moment of a magnetic substance at each point of a plane magnetic system is rotated through an angle θ without changing the system configuration, the vector of the magnetic field of the system is rotated through the angle –θ. The goal of this work was to prove another general property of plane magnetic systems consisting of permanent magnets. It is shown that if the magnetic moment of a magnetic substance at each point of the upper part of a plane magnetic system is rotated through an angle θ, whereas each magnetic moment at the lower part of the system is rotated through the angle –θ, the modulus of the Fourier transform of the magnetic field produced by the system remains unchanged, although the form of the magnetic field is changed.

1. UNIVERSALITY OF FOURIER TRANSFORMATION OF A PLANE MAGNETIC FIELD

Consider an infinite magnetic system uniform along the horizontal X-axis. The magnetic field produced by the system is [11]

$$\mathbf{H}(y, z) = \int_V d\mathbf{r}'^3 \frac{3\mathbf{R}(\mathbf{M}(y', z')\mathbf{R}) - \mathbf{M}(y', z')R^2}{R^5}, \quad (1)$$

where $\mathbf{M}(y, z)$ is the magnetization vector of the system and $\mathbf{R} = \mathbf{r} - \mathbf{r}'$, $R = |\mathbf{R}|$.

Substituting (1) into the equation for Fourier transformation of a magnetic field along the y-axis in the median plane ($z = 0$) gives on rearrangement [12]

$$\begin{aligned}\tilde{H}_z(p) = 2\pi \int_{-\infty}^{\infty} dy'dz' \exp(ipy')\exp(-|pz'|) \\ \times\{|p|M_z(y', z') - ipM_y(y', z')(\operatorname{sgn} z')\}.\end{aligned} \quad (2)$$

Consider rotation of the magnetic moment at each point of the upper part of the system through an angle θ ($z' > 0$). From the analytical geometry equations for vector rotation, it follows that, if $z' > 0$ and $p > 0$, then

$$\begin{aligned}M'_z(y', z') - iM'_y(y', z') \\ = [M_z(y', z') - iM_y(y', z')]\exp(-i\theta).\end{aligned} \quad (3)$$

The rotation of the magnetic moment at each point of the lower part of the system ($z' < 0$) through the angle –θ can be considered similarly. It was found that the same phase factor appears in integral (2) taken over the lower part of the system. Thus, for $p > 0$,

$$\tilde{H}'_z(p) = \tilde{H}_z(p)\exp(-i\theta). \quad (4)$$

1063-7842/00/4503-0356$20.00 © 2000 MAIK "Nauka/Interperiodica"

In the same manner, we obtain for $p < 0$

$$\tilde{H}'_z(p) = \tilde{H}_z(p)\exp(i\theta). \tag{5}$$

Equations (4) and (5) show that the modulus of the Fourier transform of the magnetic field does not change if the magnetic moment at each point of the upper part of the magnetic system is rotated through an angle θ and each magnetic moment in the lower part of the system is rotated through the angle $-\theta$ (see figure). However, the Fourier transforms for $p > 0$ and $p < 0$ have different phase factors. Therefore, the shape of the magnetic field is changed. The difference between the magnetic fields of two undulators of various design is considered briefly in [8]. The second undulator is obtained by rotating the permanent magnets in the upper part of the first undulator by the angle $-\pi/2$; and in the lower part, by the angle $+\pi/2$. The results of brief comparison of the magnetic fields produced by these undulators are in complete agreement with the results discussed above.

2. INVARIANCE OF ELECTROMAGNETIC RADIATION SPECTRA

Consider spontaneous electromagnetic radiation generated by relativistic particles in a plane magnetic field. First, we consider the case of dipole radiation. The spectral characteristics of the dipole radiation are determined by the modulus of the Fourier transform of the vertical component of the magnetic field [13]. Let the magnetic system be rearranged as described in Section 1. It follows from the results obtained in Section 1 and the above-mentioned property of the dipole radiation that the spectral characteristics of the electromagnetic radiation of a relativistic particle remain unaffected by such a rearrangement of the magnetic system.

Consider an infinitely long plane undulator with the period l. The integral of the magnetic field over the undulator period is zero. The wavelength λ of the nth harmonic of the undulator radiation at an angle θ to the undulator axis is

$$\lambda = \frac{l}{2n\gamma^2}(1 + \gamma^2\theta^2 + 0.5K^2). \tag{6}$$

The undulation parameter K in the case of a nonsinusoidal magnetic field is

$$K^2 = \frac{2}{l}\gamma^2\int_0^l \beta_x^2(y)\,dy, \tag{7}$$

where $\beta_x(y)$ is the horizontal component of the reduced velocity of the particle.

As follows from the equations of motion,

$$\beta_x(y) = \frac{e}{mc^2\gamma}\int_0^y H_z(y')\,dy' + \beta_x(0), \tag{8}$$

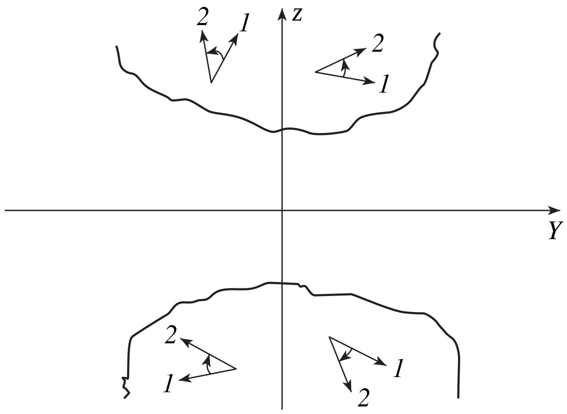

Magnetic moment rotation in a plane magnetic system based on permanent magnets: (*1*) initial position of the magnetic moments; (*2*) final position of the magnetic moments.

where e is the particle charge, m is the particle mass, and c is the velocity of light.

The Fourier coefficients of the function $\beta_x(y)$ are

$$\beta_{xk} = \frac{1}{l}\int_0^l \exp\left(i\frac{2\pi}{l}ky\right)\beta_x(y)\,dy. \tag{9}$$

The lateral displacement of the particle on traversing one undulator period is zero. Therefore, the Fourier coefficient at $k = 0$ is also zero; i.e., $\beta_{x0} = 0$. According to the Parseval theorem,

$$\frac{1}{l}\int_0^l \beta_x^2(y)\,dy = \sum_{k=-\infty}^{\infty} |\beta_{xk}|^2. \tag{10}$$

It can be easily obtained from (8) that at $k \neq 0$ the Fourier coefficients of the reduced velocity of the particle are proportional to that of the undulator magnetic field

$$\beta_{xk} = \frac{i}{2\pi}\frac{el}{kmc^2\gamma}H_{zk}, \tag{11}$$

$$H_{zk} = \frac{1}{l}\int_0^l \exp\left(i\frac{2\pi}{l}ky\right)H_z(y)\,dy. \tag{12}$$

The Fourier coefficient of the undulator magnetic field (12) can be written in a manner similar to (2). The following statement can be proven using equations (7)–(12).

Let the magnetic moments in the upper part of the system be rotated through an angle θ and in the lower part, through the angle $-\theta$ (see figure). In this case, only the phase factors in the Fourier coefficients of the undulator magnetic field (12) and in the reduced velocity of the particle (9) are changed, whereas the undulation parameter remains unaltered, as follows from (7) and (10). Therefore, the position of spectral lines of the undulator radiation also remains unchanged. However, the intensity of a particular harmonic of the undulator radiation can be changed because of variations in the undulator magnetic field. This problem should be studied in more detail.

ACKNOWLEDGMENTS

I am grateful to N.V. Smolyakov for formulation of the problem and constructive discussion.

REFERENCES

1. K. Halbach, Nucl. Instrum. Methods Phys. Res. **187**, 109 (1981).
2. G. A. Kornyukhin, G. N. Kulipanov, V. N. Litvinenko, *et al.*, Nucl. Instrum. Methods Phys. Res. **208**, 189 (1983).
3. K. Halbach, J. Phys. (Paris) **44** (C-1), 211 (1983).
4. G. Ramian, L. Elias, and I. Kimel, Nucl. Instrum. Methods Phys. Res., Sect. A **250**, 125 (1986).
5. R. Tatchyn and P. Csonka, Appl. Phys. Lett. **50**, 377 (1987).
6. R. Tatchyn, P. Csonka, and A. Toor, Rev. Sci. Instrum. **60**, 1796 (1989).
7. I. Kimel and L. Elias, Nucl. Instrum. Methods Phys. Res., Sect. A **296**, 611 (1990).
8. P. G. O'Shea, S. C. Bender, D. A. Byrd, *et al.*, Nucl. Instrum. Methods Phys. Res., Sect. A **341**, 7 (1994).
9. R. W. Warren and C. M. Fortgang, Nucl. Instrum. Methods Phys. Res., Sect. A **341**, 444 (1994).
10. K. Halbach, Nucl. Instrum. Methods **169**, 1 (1980).
11. L. D. Landau and E. M. Lifshits, *Field Theory* (Nauka, Moscow, 1967; Pergamon Press, Oxford, 1970).
12. N. V. Smolyakov, Nucl. Instrum. Methods Phys. Res., Sect. A **308**, 80 (1991).
13. R. Coisson, Phys. Rev. A **20**, 524 (1979).

Translated by K. Chamorovskiĭ

Technical Physics, Vol. 45, No. 3, 2000, pp. 359–361. Translated from Zhurnal Tekhnicheskoĭ Fiziki, Vol. 70, No. 3, 2000, pp. 72–74.

BRIEF COMMUNICATIONS

Enhancement of the Kerr Effect in Magnetooptical DyFeCo/GeO Carriers

L. V. Burkova, V. A. Seredkin, and V. Yu. Yakovchuk

Kirenskiĭ Institute of Physics, Siberian Division, Russian Academy of Sciences,
Akademgorodok, Krasnoyarsk, 660036 Russia

Received March 12, 1999

Abstract—The optimum parameters of a dielectric layer near the substrate in the interference multilayer structure are calculated. The calculations showed that this layer should have the index of refraction $n \sim 3$. The results are presented of measuring the Kerr angle of magnetooptical rotation in the multilayer structure, in which GeO films were used as dielectric layers for the first time. The maximum Kerr angle of rotation and magnetooptical quality observed in this system were 0.75° and 0.34°, respectively. These values exceed those inherent in the known information carriers, which demonstrates the advantage of this structure for use in magnetooptical discs. *© 2000 MAIK "Nauka/Interperiodica".*

At present, rare earth–transition metal amorphous films are extensively used for manufacturing magnetooptical (MO) discs [1]. For this reason, the search for methods of increasing the Kerr polar effect, which determines the magnitude of the detected signal, is urgent. One of the methods is the deposition of a dielectric layer (DL) [2], which, according to the theory [3], allows one to increase the Kerr rotation by a factor of n^2 due to interference effects, where n is its index of refraction. According to the ISO International Standard, information should be read from the substrate side of the MO disc. In this case, the DL is placed between the substrate and the magnetic layer and the MO rotation substantially depends on the difference between the indices of refraction of the substrate and the DL, which means that the latter should have large n [4]. As a storage medium in the MO discs, a multilayer interference structure is used, which consists of a magnetoactive layer embedded between the dielectric layers and of a reflection layer. The systems with SiO [4], ZnS [5], and AlN [4, 6] used as DLs were studied. They demonstrated an increase in the Kerr rotation angle by factors of 1.6, 1.75, and 1.9 compared to a single-layer film. Theoretical calculations showed that the Kerr effect can be enhanced up to 90° by selecting optimum parameters of the DL [7].

In this paper, we present the calculation and the experimental study of a multilayer structure in which GeO films were used as DLs for the first time and amorphous DyFeCo films were used as the magnetoactive and reflecting layers.

Samples were prepared by thermal evaporation in vacuum (3×10^{-4} Pa). The interfering dielectric GeO layer, the magnetoactive DyFeCo layer (10 nm thick), the dielectric GeO layer (34 nm thick), and the reflecting DyFeCo layer were successively deposited on glass substrates whose temperature was 20–30°C. The structure thus obtained was covered with a protective GeO layer 150 nm thick. The thickness of the dielectric GeO layer near the substrate was varied from 60 to 102 nm. The reflecting layer was selected to be larger than the skin layer for the wavelength range from 780 to 820 nm used in the MO storage and was 70 nm thick. The schematic of this system is presented in Fig. 1.

The DyFeCo magnetic layers contained 20 at.% of Dy and 80 at.% of FeCo, the ratio of Fe to Co being 2 : 1. This provided perpendicular anisotropy in the films, the optimum value of the coercive force ($H_c \approx 3$ kOe), and the maximum Kerr angle of rotation per layer $\theta_k \approx 0.17°$.

The MO parameters were measured on an MO setup with zero compensation in fields up to 16 kOe. The coercive force was measured from the MO hysteresis loops. The reflection coefficient R was measured with a Specord UV-VIS modernized spectrophotometer. To find optimum parameters of the DL near the substrate at which the Kerr angle of rotation should resonantly

Air	0	$N_0 = n_0 = 1$
Glass substrate	1	$N_1 = n_1 = 1.52$
Dielectric layer	2	$N_2 = n_2 = ?$
Magnetoactive DyFeCo layer	3	$N_3 = 2.4 - i2.6$
Dielectric GeO interlayer	4	$N_4 = n_4 \sim 2.8$
Reflecting DyFeCo layer	5	$N_5 = 2.4 - i2.6$
Protective GeO layer	6	$N_6 = n_6 \sim 2.8$

$Q_3 = Q_5 = 0.0149 + i0.006$

Fig. 1.

1063-7842/00/4503-0359$20.00 © 2000 MAIK "Nauka/Interperiodica"

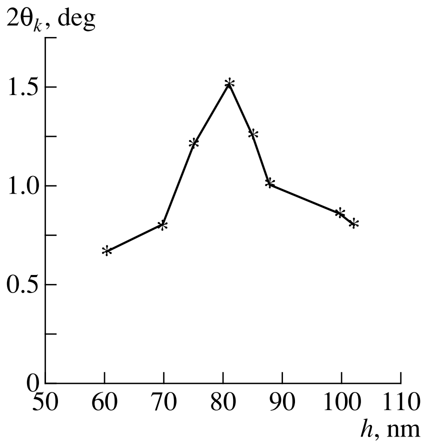

Fig. 2. Dependence of the Kerr angle of rotation on the thickness of the dielectric layer near the substrate.

increase due to interference effects, we calculated the index of refraction and thickness of this layer from the expressions [7]

$$n_2^2 = n_1 n_3 + (n_3 k_1^2 - n_1 k_3^2)/(n_1 - n_3), \qquad (1)$$

$$\tan\delta_2 = -n_2(n_1 - n_3)/(n_1 k_3 + n_3 k_1), \qquad (2)$$

where $\delta_2 = 2\pi n_2 h_2/\lambda$ is the phase incursion in a layer of thickness h_2; $N_j = n_j - ik_j$ is the complex index of refraction of the jth layer, where n_j is the real index of refraction and k_j is the absorption coefficient; and the subscripts correspond to the situation when the dielectric layer (j = 2) is adjacent, on one side, to the external medium (j = 1) and to the magnetic layer (j = 3) on the other side.

The calculations were performed for the structure presented in Fig. 1. Here, the media on both sides of the DL providing the interference themselves consist of a set of layers; n_1, k_1, n_3, k_3 correspond to the effective values, which in turn were determined from coefficients of reflection from corresponding interfaces.

Taking into account that the glass substrate is transparent ($N_2 = n_2$), we can write the amplitude reflectance from the substrate side in the form [8]

$$\begin{aligned} r_{02} &= (r_{01} + r_{12}\cos 4\pi n_1 h_1/\lambda) \\ &\times (1 + r_{01} r_{12} \cos 4\pi n_1 h_1/\lambda)^{-1} \end{aligned} \qquad (3)$$

and the reflection coefficient of the system will be described by the expression

$$R_{02} = \frac{r_{01}^2 + r_{12}^2 + 2 r_{01} r_{12}\cos(-\Delta_{01} + \Delta_{12} - 4\pi n_1 h_1/\lambda)}{1 + r_{01}^2 r_{12}^2 + 2 r_{01} r_{12}\cos(\Delta_{01} + \Delta_{12} - 4\pi n_1 h_1/\lambda)}, \qquad (4)$$

where $r_{ij} = (N_i - N_j)/(N_i + N_j)$ and Δ_{01} and Δ_{12} are the changes in the phase at the interfaces, which are equal to 0 or π, depending on whether r_{01} and r_{12} positive or negative; i.e., in this case, $\Delta_{01} = \Delta_{12} = \pi$. Thus, the calculation of R_{02} results in the replacement of the two interfaces on the substrate side relative to the DL by one effective surface. The effective value $n_{1\,\mathrm{eff}}$ of the real index of refraction of the medium on the substrate side was obtained from the expression [8]

$$R_{02} = (n_{1\,\mathrm{eff}} - n_2)^2 (n_{1\,\mathrm{eff}} + n_2)^{-2}, \qquad (5)$$

$$n_{1\,\mathrm{eff}} = n_2(1 + R_{02} \pm 2\sqrt{R_{02}})(1 - R_{02})^{-1}. \qquad (6)$$

The effective value of the index of refraction $n_{3\,\mathrm{eff}}$ and the absorption coefficient $k_{3\,\mathrm{eff}}$ on the side of the magnetoactive layer were obtained from the measured amplitude reflection coefficient of the effective surface, which replaced two neighboring interfaces, starting with the protecting GeO layer. To simplify the calculations, we neglected complex magnetooptical parameters in the index of refraction of the DyFeCo films because of their smallness. Based on the general expression for the amplitude reflection coefficient [7], we can write the following expressions:

$$\begin{aligned} r_{46} &= [r_{45} + r_{56}\exp(-i4\pi n_5 h_5/\lambda)] \\ &\times [1 + r_{45} r_{56} \exp(-i4\pi n_5 h_5/\lambda)]^{-1}, \\ r_{45} &= (N_4 - N_5)/(N_4 + N_5), \\ r_{56} &= (N_5 - N_6)/(N_5 + N_6); \end{aligned} \qquad (7)$$

$$\begin{aligned} r_{36} &= [r_{34} + r_{46}\exp(-i4\pi n_4 h_4/\lambda)] \\ &\times [1 + r_{34} r_{46} \exp(-i4\pi n_4 h_4/\lambda)]^{-1}, \\ r_{34} &= (N_3 - N_4)/(N_3 + N_4); \end{aligned} \qquad (8)$$

$$\begin{aligned} r_{26} &= [r_{23} + r_{36}\exp(-i4\pi n_3 h_3/\lambda)] \\ &\times [1 + r_{23} r_{36} \exp(-i4\pi n_3 h_3/\lambda)]^{-1}, \\ r_{23} &= (N_2 - N_3)/(N_2 + N_3); \end{aligned} \qquad (9)$$

$$R_{26} = r_{26}^2, \qquad (10)$$

$$N_{3\,\mathrm{eff}} = n_2(1 + R_{26} \pm 2\sqrt{R_{26}})(1 - R_{26})^{-1}, \qquad (11)$$

$$N_{3\,\mathrm{eff}} = n_{3\,\mathrm{eff}} - ik_{3\,\mathrm{eff}}. \qquad (12)$$

Our calculations showed that the DL should have the index of refraction $n = 3$. The GeO films are the best candidates for such layers, because the measurement showed that their index of refraction is $n \sim 2.8$. Calculated from (2), the optimum thickness h_2 of the GeO film in the structure considered was ~95 nm.

The Kerr angle of rotation in the dielectric GeO film with optimum thickness can be evaluated from the polarization of light reflected from the external surface of this multilayer structure. In the approximation linear in magnetization, this angle is [9]

$$\theta_k = \mathrm{Im}(\chi/r), \text{ if } |\chi| \ll |r|, \qquad (13)$$

where $r^{\pm} = r \pm \chi$ is the amplitude reflection coefficients for circularly polarized components with right (+) and left (–) directions of rotation, respectively.

These coefficients were determined using the scheme described above, but using the index of refraction for circularly polarized waves in the magnetoactive medium, which is described by the expression [9]

$$N_j^{\pm} = N_j\sqrt{1 \pm Q_j}, \tag{14}$$

where N_j is the complex index of refraction, which is determined by the diagonal component of the dielectric constant tensor, and Q_j is the complex MO parameter related to the gyrotropy of the magnetic medium.

In contrast to the above calculations, we should consider the entire system, so that expressions (7)–(9) should be supplemented by the expressions

$$r_{16} = [r_{12} + r_{26}\exp(-i4\pi n_2 h_2/\lambda)]$$
$$\times[1 + r_{12}r_{26}\exp(-i4\pi n_2 h_2/\lambda)]^{-1}, \tag{15}$$
$$r_{12} = (N_1 - N_2)/(N_1 + N_2);$$
$$r_{06} = [r_{01} + r_{16}\exp(-i4\pi n_1 h_1/\lambda)]$$
$$\times[1 + r_{01}r_{16}\exp(-i4\pi n_1 h_1/\lambda)]^{-1}, \tag{16}$$
$$r_{01} = (N_0 - N_1)/(N_0 + N_1).$$

Having thus obtained r_{06}^{+} and r_{06}^{-}, we can determine θ_k from (13). The necessary values of MO and optical parameters of the DyFeCo films (Fig. 1) were taken from the data for amorphous TbFe films [10, 11]. The Kerr angle of rotation was measured to be ~0.7°.

The experimental dependence of the Kerr angle of rotation on the DL thickness for the multilayer structure is shown in Fig. 2. This dependence exhibits a resonance, which suggests that the interference effect increases the MO rotation. One can see from Fig. 2 that the maximum angle of rotation $2\theta_k = 1.5°$ corresponds to the structure with the DL thickness ~81 nm, in good agreement with calculations. Such an angle of rotation is 4.5 times larger than that for a single-layer magnetic film, and the corresponding MO quality $\sqrt{R}\,\theta_k$ is 0.34°. These values exceed the corresponding parameters for known information carriers, made of rare earth–transition metal films. Thus, GeO films of optimum thickness used as the DL in multilayer film structures increase the Kerr angle of rotation by several times compared to a single-layer film. These are promising media structures for use in MO discs. The calculations based on the interference effects are in good agreement with the experimental data and can be used for the evaluation of optimum parameters of the dielectric layer.

ACKNOWLEDGMENTS

This work was supported by the Russian Foundation for Basic Research, grant no. 98-02-16139.

REFERENCES

1. L. V. Burkova and G. I. Frolov, Zarubezhn. Élektron. Tekh. **9**, 3 (1987).
2. M. M. Noskov, Dokl. Akad. Nauk SSSR **31**, 112 (1941).
3. A. V. Sokolov, *Optical Properties of Metals* (Gos. Izd. Fiz.-Mat. Lit., Moscow, 1961).
4. T. Niihara, N. Ohta, K. Kaneko, *et al.*, IEEE Trans. Magn. **22**, 1215 (1986).
5. F. Tanaka, Y. Nagao, and N. Imamura, IEEE Trans. Magn. **20**, 1033 (1984).
6. M. Tabata, Jpn. J. Appl. Phys. **33**, 5811 (1994).
7. G. A. Bolotin, Fiz. Met. Metalloved. **6**, 197 (1991).
8. T. N. Krylova, *Interference Coatings* (Mashinostroenie, Leningrad, 1973).
9. G. A. Bolotin and A. V. Sokolov, Fiz. Met. Metalloved. **12**, 785 (1961).
10. G. A. Prinz, J. J. Krebs, D. W. Forester, *et al.*, J. Magn. Magn. Mater. **15–18**, 779 (1980).
11. T. R. McGuire, R. J. Gambino, A. E. Bell, *et al.*, J. Magn. Magn. Mater. **54–57**, 1387 (1986).

Translated by S. Bulanov

Technical Physics, Vol. 45, No. 3, 2000, pp. 362–364. Translated from Zhurnal Tekhnicheskoĭ Fiziki, Vol. 70, No. 3, 2000, pp. 75–77.
Original Russian Text Copyright © 2000 by Buznikov, Pukhov, Rakhmanov.

BRIEF COMMUNICATIONS

The Stability of Wide High-Temperature Superconducting Films with Varying Transport Current

N. A. Buznikov, A. A. Pukhov, and A. L. Rakhmanov

Scientific Center for Applied Problems of Electrodynamics, Associated Institute of High Temperatures,
Russian Academy of Sciences, Izhorskaya ul. 13/19, Moscow, 127412 Russia

Received March 12, 1999

Abstract—The current-carrying capacity of a wide high-temperature superconducting film under conditions of rapid injection of current is investigated theoretically. An analytic expression is derived for the rate of current injection into the film at which a marked degradation of the current-carrying capacity of the film occurs. The obtained results may be important from the standpoint of analyzing the stability of superconducting ac devices. *© 2000 MAIK “Nauka/Interperiodica”.*

The close relationship between thermal and electromagnetic phenomena in superconductors may lead to the emergence of thermomagnetic instability in them [1]. The conditions of emergence and development of thermomagnetic instability have been studied in detail for low-temperature superconductors. It is known that this effect defines the value of the current-carrying capacity I_q of composite superconductors [2, 3] and superconducting films [4] and leads to anomalies of inception and propagation of the normal phase [5, 6]. Upon transition to nitrogen temperatures, the above-mentioned phenomena are extended to high-temperature superconductors (HTSC) to only a small degree. We have investigated the scale of the rate of variation of current I at which degradation of the current-carrying capacity of a wide high-temperature superconducting film becomes pronounced.

We will consider an HTSC film of thickness D_f and width $W \gg D_f$ placed on a dielectric substrate of thickness $D_s \gg D_f$, whose reverse side is stabilized with respect to temperature $T = T_0$. A transport current I is injected into the film at a high rate $\dot{I}$. As the current increases, saturated regions $W_c\langle Y\rangle W/2$ are formed at the film edges (Fig. 1), in which current density j is equal to the critical density j_c [7, 8]. The quantity W_c is defined by the expression [7]

$$W_c = W(1-i^2)^{1/2}/2. \tag{1}$$

Here, $i = I/I_c$, and $I_c = j_c W D_f$ is the critical current of the HTSC film. Because j_c depends on temperature, a minor fluctuation of temperature $\delta T > 0$ causes a decrease in J_c, and the magnetic flux penetrates into the greater part of the film. As a result of the flux motion, an additional electric field δE is induced in the film, which causes additional heat release. Under certain conditions, this process assumes an avalanche behavior [1] and the film makes a transition to the normal state at a current I_q that is less than the critical current I_c.

In a linear (with respect to minor perturbations) approximation, the heat and Maxwell equations in the saturated region of the film have the form

$$C_f = \frac{\partial(\delta T)}{\partial t} = k_f \frac{\partial^2(\delta T)}{\partial X^2} + j_c \delta E, \tag{2}$$

$$\frac{\partial^2(\delta E)}{\delta Y^2} = \mu_0 \left\{ \sigma(E) \frac{\partial(\delta E)}{\delta t} + \frac{\partial j_c}{\partial T} \frac{\partial(\delta T)}{\partial t} \right\}, \tag{3}$$

where X and Y are coordinates (Fig. 1), t is the time, C_f and k_f respectively denote the specific heat and thermal conductivity of the film, and $\sigma(E) = \partial j/\partial E$ is the differential conductance of the film.

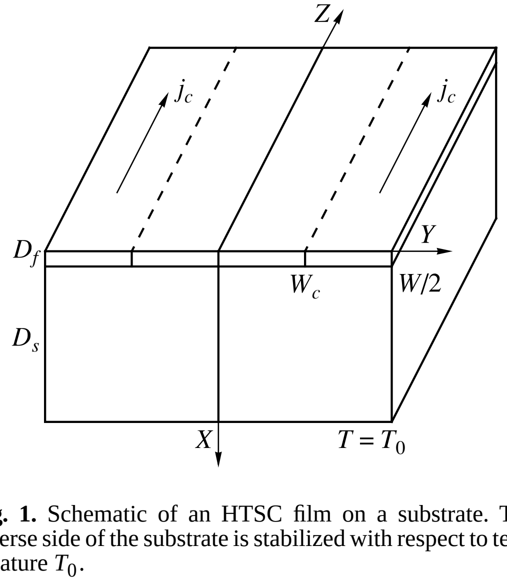

Fig. 1. Schematic of an HTSC film on a substrate. The reverse side of the substrate is stabilized with respect to temperature T_0.

1063-7842/00/4503-0362$20.00 © 2000 MAIK “Nauka/Interperiodica”

In equation (2), we disregarded the variation of temperature over the film width, because $W \gg D_f$, and in equation (3), we ignored the nonuniformity of the electric field distribution over the film thickness. The distribution of j, E, δT, and δE over the film width is shown schematically in Fig. 2.

The temperature variation δT in the substrate is described by the equation

$$C_s \frac{\partial(\delta T)}{\partial t} = k_s \frac{\partial^2(\delta T)}{\partial X^2} \tag{4}$$

with the boundary condition $\delta T = 0$ at $X = D_s$. Here, C_s and k_s are the specific heat and thermal conductivity of the substrate, respectively. For a linear analysis of stability, we will seek δT and δE in the form

$$\begin{aligned} \delta T &= \theta(X)(T_c - T_0)\exp(4k_f \lambda t / C_f W^2), \\ \delta E &= \varepsilon(Y)\frac{4k_f(T_c - T_0)}{j_c W^2}\exp(4k_f \lambda t / C_f W^2), \end{aligned} \tag{5}$$

where T_c is the critical temperature and λ is the increment of the rise of perturbation.

We will substitute (5) into equations (2)–(4) and integrate (2) and (3) with respect to the film thickness (ignoring the dependence of δT and E on X) and (4) with respect to the substrate thickness. We use the condition of continuity of the heat flux on the film–substrate boundary, with due regard for the effect of thermal resistance of the interface R_{bd}, to derive for the dimensionless perturbation ε the equation

$$\begin{aligned} \frac{\partial^2 \varepsilon}{\partial y^2} + \Bigg[\frac{\beta}{\lambda + a\sqrt{\lambda}\coth(b\sqrt{\lambda})/\{1 + r\sqrt{\lambda}\cosh(b\sqrt{\lambda})\}} \\ - \tau(E)\Bigg]\lambda\varepsilon = 0 \end{aligned} \tag{6}$$

with the boundary conditions $\varepsilon = 0$ at $y = 2W_c/W$ and $\partial\varepsilon/\partial y = 0$ at $y = 1$ [4]. Here,

$$\begin{gathered} y = \frac{2Y}{W}, \quad \beta = -\mu_0 \frac{\partial j_c}{\partial T}\frac{j_c W^2}{4C_f}, \quad \tau(E) = \frac{\mu_0 k_f \sigma(E)}{C_f}, \\ a = \frac{W}{2D_f}\sqrt{\frac{C_s k_s}{C_f k_f}}, \quad b = \frac{2D_s}{W}\sqrt{\frac{C_s k_f}{C_f k_s}}, \\ r = \frac{2R_{bd}}{W}\sqrt{\frac{C_c k_s k_f}{C_f}}. \end{gathered} \tag{7}$$

It follows from equation (6) that the film stability increases with $\tau(E)$. In the region of low electric fields, the film conduction σ increases with the decrease in the electric field E proportional to the rate of current injection $\dot{I}$ [1]. For small values of $\dot{I}$, the value of $\sigma(E)$ is high and the current-carrying capacity is equal to the critical current I_c. As $\dot{I}$ decreases, the value of $\sigma(E)$ decreases and the current I_q becomes less than I_c. In order to derive the analytical solution of equation (6), we will represent the dependence $\sigma(E)$ in the form $\sigma(E) = j_1/\langle E\rangle$, where $j_1 \ll j_c$ and $\langle E\rangle$ is the electric field averaged over the film width [7],

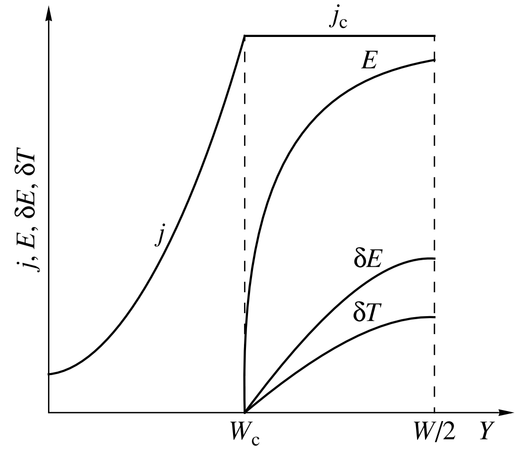

Fig. 2. The distribution of j, E, δT, and δE over the film width.

$$\langle E\rangle = \frac{\mu_o \dot{I}}{4\pi}\left[\ln\left(\frac{1+i}{1-i}\right) - 2i\right]. \tag{8}$$

The condition of existence of a nontrivial solution of equation (6), in view of (1), yields the equation for the increment λ,

$$\begin{aligned} \frac{\lambda\beta}{\lambda + a\sqrt{\lambda}\coth(b\sqrt{\lambda})/\{1 + r\sqrt{\lambda}\coth(b\sqrt{\lambda})\}} \\ - \lambda\tau = \varphi(i), \quad \varphi(i) = \frac{\pi^2}{4[1 - (1 - i^2)^{1/2}]^2}. \end{aligned} \tag{9}$$

Assuming that the thermal conductivity of the substrate and its thickness are sufficiently great ($a \gg |\sqrt{\lambda}|$, $b|\sqrt{\lambda}| \gg 1$) and the effect of the thermal resistance of the boundary is small ($r|\sqrt{\lambda}| \ll 1$), we derive the condition of emergence of thermomagnetic instability ($\mathrm{Re}\lambda = 0$)

$$\beta = a\sqrt{2\tau\varphi(i_q)}, \tag{10}$$

where $i_q = I_q/I_c$.

We use (7)–(9) to derive from this condition the following equation for the current-carrying capacity:

$$\begin{aligned} &[\ln\{(1 + i_q)/(1 - i_q)\} - 2i_q] \\ &\times [1 - (1 - i_q^2)^{1/2}]^2 = \dot{I}_0/\dot{I}. \end{aligned} \tag{11}$$

The characteristic scale of the rate of injection of current

$$\dot{I}_0 = \frac{8\pi^3 j_1 k_s C_s}{\mu_0^2 j_c^2 (\partial j_c / \partial T)^2 D_f^2 W^2} \qquad (12)$$

defines the degree of degradation of the current-carrying capacity. If $\dot{I} \le \dot{I}_0$, then $I_q \cong I_c$ and a marked degradation of the current-carrying capacity will be observed at $\dot{I} \ge \dot{I}_0$. We will estimate the value of $\dot{I}_0$ for a Y–Ba–Cu–O film located on a $LaAlO_3$ substrate. For estimation, we assume that $j_c \cong 10^{10}$ A m^{-2}, $j_1 \cong 10^8$ A m^{-2}, $\partial j_c/\partial T \cong 10^9$ A m^{-2} K^{-1}, $D_f \cong 10^{-6}$ m, $k_s \cong 20$ W m^{-1} K^{-1}, and $C_s \cong 10^5$ J m^{-3} K^{-1} to derive $\dot{I}_0 \approx 3 \times 10^8$ A s^{-1} at $W \cong 10^{-3}$ m and $\dot{I}_0 \approx 3 \times 10^4$ A s^{-1} at $W \cong 10^{-1}$ m.

Therefore, in view of the model assumptions made above, one can assume that no marked degradation of the current-carrying capacity upon rapid injection of current, which is associated with thermomagnetic instability, will be observed in film bridges ($W \cong 10^{-3}$ m). At the same time, recent progress in the technology of manufacturing high-quality wide ($W \cong 10^{-1}$ m) films and new applications associated with high rates of variation of current (($\dot{I} \cong 10^5$–10^6 A s^{-1}) make it necessary to include the degradation of the current-carrying capacity.

In so doing, a decrease of I_q with a rise in the rate of current variation may lead to an anomalously rapid propagation of the normal phase [5], its multiple inception on the defects [6], a redistribution of gas on the film surface with normal regions [9], and an abrupt decrease in the energy of critical perturbations destroying the superconducting state [5, 9, 10]. The criterion of the emergence of such singularities is provided by the condition [11]

$$\dot{I}_0 t_h / I_c \ll 1, \qquad (13)$$

where $t_h = C_s D_s^2 / k_s$ is the characteristic relaxation time of temperature of the film–substrate system.

For wide HTSC films ($W \cong 10^{-1}$ m) at $t_h \cong 5 \times 10^{-3}$ s and $I_c \cong 10^2$ A, equation (13) yields $\dot{I}_0 t_h / I_c \approx 10^{-2}$. Therefore, the above-identified anomalies of destruction of superconductivity may be observed in wide films. In conclusion, note that in low-temperature superconducting films a marked degradation of the current-carrying capacity occurs at relatively low rates of injection of current $\dot{I} \approx 10^3$ A s^{-1} [4], which is associated with a substantial decrease in the heat capacity of the substrate upon transition from nitrogen to helium temperatures.

ACKNOWLEDGMENTS

This study received support from the State Scientific and Technical Program on “Topical Trends in the Physics of Condensed Media” (project no. 96083) and from the Russian Foundation for Basic Research (project no. 98-02-16046).

REFERENCES

1. A. V. Gurevich, R. G. Mints, and A. L. Rakhmanov, *The Physics of Composite Superconductors* (Nauka, Moscow, 1987).
2. V. V. Andrianov, V. P. Baev, S. S. Ivanov, *et al.*, Cryogenics **22**, 81 (1982).
3. A. A. Pukhov, A. L. Rakhmanov, V. N. Tsikhon, and V. S. Vysotsky, Supercond. Sci. Technol. **7** (3), 154 (1994).
4. A. B. Vaganov, T. Yu. Patsaeva, and A. L. Rakhmanov, Fiz. Tverd. Tela (Leningrad) **31**, 151 (1989) [Sov. Phys. Solid State **31**, 260 (1989)].
5. N. A. Buznikov, A. A. Pukhov, and A. L. Rakhmanov, Cryogenics **34**, 761 (1994).
6. N. A. Buznikov, A. A. Pukhov, and A. L. Rakhmanov, Cryogenics **35**, 623 (1995).
7. W. T. Norris, J. Phys. D **3**, 489 (1970).
8. A. I. Larkin and Yu. N. Ovchinnikov, Zh. Éksp. Teor. Fiz. **61**, 1221 (1971) [Sov. Phys. JETP **34**, 651 (1971)].
9. J.-P. Wu and H.-S. Chu, Cryogenics **36**, 925 (1996).
10. A. Unal and M.-C. Chyu, Cryogenics **34**, 123 (1994).
11. N. A. Buznikov and A. A. Pukhov, Cryogenics **37**, 71 (1997).

Translated by Henri A. Bronstein

Technical Physics, Vol. 45, No. 3, 2000, pp. 365–368. Translated from Zhurnal Tekhnicheskoĭ Fiziki, Vol. 70, No. 3, 2000, pp. 78–81.
Original Russian Text Copyright © 2000 by Sher, Mikushkin, Sysoev, Melekh.

BRIEF COMMUNICATIONS

The Effect of Energetic Oxygen Atoms on the Formation of CuO Films by Magnetron Sputtering

É. M. Sher, V. M. Mikushkin, S. E. Sysoev, and B. T. Melekh

Ioffe Physicotechnical Institute, Russian Academy of Sciences,
Politekhnicheskaya ul. 26, St. Petersburg, 194021 Russia

Received April 4, 1996; in final form, February 5, 1999

Abstract—The chemical composition of thin copper oxide films was studied by X-ray photoelectron spectroscopy (XPS). The films were obtained by magnetron sputtering of copper metal, which was simultaneously oxidized by atomic oxygen. It was demonstrated that a high rate of oxidation in molecular oxygen is achieved only under relatively low rates of film growth ($v < 100$ Å/min). However, the growth rate of cupric oxide can be drastically increased to $v > 750$ Å/min in a flow of accelerated oxygen atoms. High growth rates are necessary to substantially cut the thermal budget and reduce the diffuseness of heterofunctions in fabricating layered structures containing copper oxide. © *2000 MAIK "Nauka/Interperiodica".*

INTRODUCTION

In this work, we solve the problem of drastic (more than two orders of magnitude) increase in the rate of copper oxidation upon forming thin oxide films. The fabrication of oxide, and especially high-temperature superconducting (HTSC) heterostructures with sharp heterojunctions, is still a challenge. Low rates of copper oxidation and final oxidation of cuprite (Cu_2O) result in a great thermal budget being needed for the growth of cuprate materials and in an additional interface diffuseness by hundreds of angstroms [1]. This problem is inherent not only in MBE and magnetron sputtering of metal copper but also in magnetron and laser sputtering of completely oxidized copper. The fact is that, under thermal decomposition, a partial transformation of cupric oxide into cuprous oxide takes place and oxidized copper can be reduced to the metal state under ion bombardment. The problem was solved by using a flow of atomic, instead of molecular, oxygen. It was demonstrated earlier that the application of a plasma source generating a beam of oxygen atoms and ions makes it possible to completely oxidize copper at substantially lower temperatures and to grow good HTSC films without postgrowth annealing [2, 3]. However, the growth rate of films with completely oxidized copper remained very low ($v < 6$ Å/min). The increased rate of CuO growth reported in this work ($v > 750$ Å/min) is explained in simple thermodynamic terms. However, the applicability of the thermodynamic approach was not immediately evident, because the oxidation process takes place in a nonequilibrium system consisting of a limited number of copper atoms (in one or two monolayers of the material) and a still lesser number of oxygen atoms in the flow. That oxygen atoms coming from the existing sources are accelerated and thus can break already formed chemical bonds aggravates the situation.

EXPERIMENTAL

Copper oxide films were grown with a magnetron sputterer (Ion Tech, England). Two FAB-110 sources of atomic particles were placed into the vacuum chamber. The sources are constructed in such a way that the molecules of a working gas, when subjected to internal fields, dissociate and ionize. The ionized particles are then accelerated towards the grid where they are neutralized by a beam of secondary electrons. The outcoming beam consists of only accelerated atoms, which prevents static charging of the samples. One of the FAB-110 sources was used for cleaning the substrate ($SrTiO_3$) by means of argon atom bombardment immediately before copper deposition. The second source was used for the oxidation of deposited metal with oxygen atoms. The temperature of the substrate during growth was $T = 700$°C.

The elemental and chemical compositions of the films were studied by XPS with an LHS-11 electron spectrometer (Leybold-AG, Germany). An aluminum anode tube (AlK_α line, $h\nu = 1486.6$ eV) was used as an X-ray source. The energy spectra of primary photoelectrons were recorded at a constant incident energy $E =$ 100 eV and an energy resolution $\Delta E = 1.0$ eV. The energy scale of the spectrometer was calibrated from the metallic copper and gold lines. The spectra of copper and oxygen photoelectrons were obtained by summing data of several successive measurements. This substantially diminishes errors due to variations of the X-ray intensity and the detector efficiency.

Samples were transported from the load lock to the spectrometer in an atmosphere of dry nitrogen. This, however, could not completely prevent the surface from being contaminated by carbon-containing molecules or water. XPS is a surface-sensitive technique; that is why it was important to get rid of the contaminations or to take them into account in the results of analysis. Conventional (for XPS) cleaning of the surface by ion etching was inapplicable, since the chemical composition of the copper oxide was severely affected by the ion beam: the cupric oxide lost oxygen and became cuprous. Therefore, we used a computer "cleaning" procedure to analyze the chemical composition. The procedure lies in determining the contribution of adsorbed molecules [2]. The binding energies of CO and H_2O, necessary for this procedure, were determined by examining a gold surface exposed to air. The same lines, along with the copper satellite, were used for the determination of static charges on dielectric samples [2].

RESULTS AND DISCUSSION

Figure 1 shows photoelectron spectra of $\mathrm{Cu2p}_{3/2}$ for three samples of copper oxide: (*1*) a bulk reference sample and two films grown in the sputterer in the atmosphere of molecular oxygen with (*2*) low and (*3*) high growth rates. The reference was obtained by thermally oxidazing bulk copper metal in molecular oxygen to the formation of black CuO oxide scale. The spectra contain the principal line *A* and the satellite *B*. Their energy scale—the scale of binding energies of a primary electron—was corrected for the value of the static charge. The observed lines involve unresolved elementary components that correspond to different chemical states of copper. The analysis of the chemical composition of the samples is presented in Fig. 2 as a decomposition of the lines Cu2$p_{3/2}$ and O1s. The contribution from the adsorbed water and carbon oxide molecules to the photoelectron lines of oxygen (Fig. 2, curves 1*b*–3*b*) is no higher than several percent. The decomposition of the photoelectron lines of copper and oxygen allows one to determine the relative contents of copper oxides and copper hydroxide. The latter is formed by interaction of the surface with atmospheric water or due to insufficient purification of molecular oxygen used for film growth.

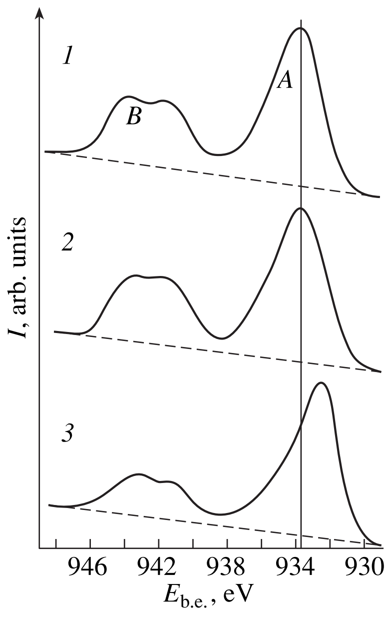

Fig. 1. (*A*) Principal and (*B*) satellite Cu2$p_{3/2}$ lines in the X-ray photoelectron spectra of (*1*) the bulk reference CuO sample and copper oxide films grown in the atmosphere of molecular oxygen with (*2*) low and (*3*) high rates.

The decomposition of the photoelectron lines into the components corresponding to different chemical phases was performed according to the method described in [4] and used earlier for the analysis of the chemical composition of InP native oxides. In our case, the problem is unambiguously solved by setting a "comb," i.e., differences between the binding energies of the ground level of an atom in different chemical states. The uniqueness of the decomposition was proved by coincidence of the chemical compositions determined with the copper and oxygen lines. Note that this approach does not require accurate predetermination of the static charge on the samples. The charge is found from joint analysis of both lines [5]. A comparison of the spectra presented in Fig. 2 suggests that sample *2*, obtained at the low growth rate ($v = 10$ Å/min), contains a greater fraction of CuO than sample *3*, grown with the high growth rate ($v = 750$ Å/min).

Decomposing photoelectron lines is a rather tedious procedure, and further analysis of ten samples used the ratio between the intensities of the satellite line *B* and the principal line *A*. A satellite is absent in the spectrum of monovalent copper; hence, its relative intensity may characterize the fraction of bivalent copper or cupric oxide in the mixture of the oxides. In this case, calibration was performed with regard for Fig. 2 for the reference sample, containing no more than 5% of monovalent copper. Degree of copper oxidation vs. the oxide growth rate curves constructed from the relative satellite intensities for two groups of samples are shown in Fig. 3. Samples from the first group (curve *2*) were grown in the atmosphere of molecular oxygen; and those from the second group (curve *1*), in the flow of atomic oxygen produced by the FAB-110 source. The filled circle corresponds to the film subjected to two-hour postgrowth annealing in the atmosphere of molecular oxygen. As seen from Fig. 3, such an annealing does not increase the degree of oxidation in comparison with the best samples grown *in situ*. It also follows from this figure that a high degree of oxidation in molecular oxygen is achieved only at low growth rates ($v < 10$ Å/min), whereas the use of atomic oxygen makes it possible to achieve the same result even at very high rates ($v > 750$ Å/min) that exceed those reported in [1–3] by two orders of magnitude.

Consider a mechanism of oxidation. Note, first of all, that the densities of the oxygen and copper atom flows are too low for the near-surface reaction in the gas phase to proceed. According to our estimates, copper islands, one or two monolayers covering cupric oxide, or the mixture of cuprous and cupric oxides are oxidized. Such a situation is observed under dynamic equilibrium, when unoxidized copper is continuously deposited onto a layer being oxidized. This process is basically different from the oxidation of bulk metal by gaseous oxygen, where the rate of the reaction is defined not only by its free energy but also by diffusion through the oxide layer. If the molar volumes of the oxide layer and the metal are the same, the oxide may completely inhibit oxidation, as, for example, with aluminum. That is why, in our case, the oxidation process can be treated in thermodynamic terms. Under atmospheric pressure and a substrate temperature $T = 1000$ K, molecular oxygen can oxidize copper completely, partially, or in two stages, because each of the following reactions is characterized by a negative free energy $\Delta G°$ [6]:

$$Cu + 0.5O_2 \longleftrightarrow CuO, \quad \Delta G° = -16.05 \text{ kcal}, \qquad (1)$$

$$2Cu + 0.5O_2 \longleftrightarrow Cu_2O, \quad \Delta G° = -23.7 \text{ kcal}, \qquad (2)$$

$$Cu_2O + 0.5O_2 \longleftrightarrow 2CuO, \quad \Delta G° = -8.35 \text{ kcal}. \qquad (3)$$

In actual growth processes, oxidation, and especially final oxidation (3) of copper, are hindered because of both an insufficiently high partial density of oxygen and a high energy barrier of the reactions, which is related to the necessity of breaking at least one bond in an O_2 molecule. Complete oxidation of copper by molecular oxygen observed in our experiments indicates that the energy barrier can be overcome at $T =$ 1000 K. However, an insufficient partial pressure of oxygen lowers the magnitude of the free energy $\Delta G°$ of reactions (1)–(3) and, hence, the reaction rates. Therefore, complete oxidation is achieved only at low growth rates $v < 10$ Å/min.

The use of atomic, instead of molecular, oxygen ($0.5O_2 \longrightarrow O$) increases the absolute values of the free energy of reactions (1)–(3) by 28 kcal and virtually eliminates the problem of energy barrtier. Therefore, a sharp increase in the copper oxidation rate could be expected for the case of classical atomic ensembles described in terms of thermodynamics. Our system is not classical. Here, a limited number of oxygen atoms or molecules interact with copper atoms within a one- or two-atom-thick surface layer. In addition, the oxygen atoms are energetic (in practice, a beam of atoms is difficult to thermalize). Nevertheless, as follows from our experimental results, such a substitution has a great beneficial effect. In this case, oxygen–copper interaction can be considered as follows. Some atoms of an oxygen flow are scattered by the surface and lost. The rest enter the near-surface growth area of the film and lose an excess of kinetic energy in collisions, sometimes destroying already formed chemical bonds and

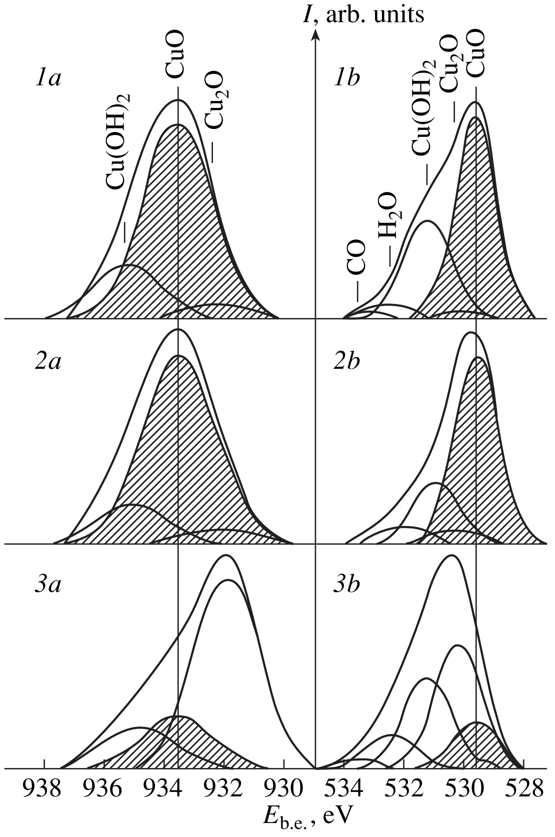

Fig. 2. Decomposition of the (*a*) $Cu2p_{3/2}$ and (*b*) O1s photoelectron lines into the components corresponding to different chemical states of copper and oxygen. (*1*) Bulk reference CuO sample and films of copper oxides grown in the atmosphere of molecular oxygen with (*2*) low and (*3*) high rates.

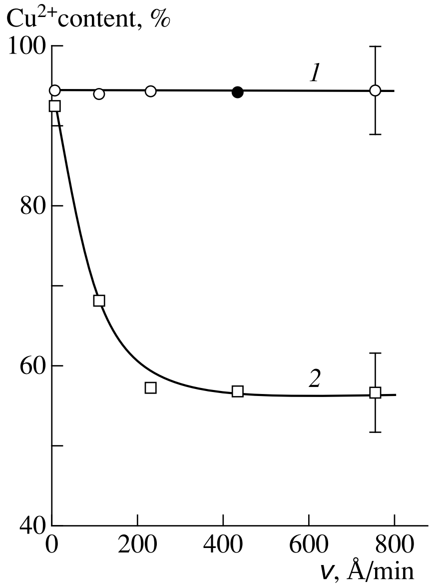

Fig. 3. Dependence of the bivalent copper content in oxide films on the growth rate (*1*) in the flow of atomic oxygen and (*2*) in the atmosphere of molecular oxygen; the filled circle corresponds to two-hour postgrowth annealing in molecular oxygen.

causing the cupric-to-cuprous oxide transformation. Multiple collisions thermalize oxygen atoms, and eventually they form chemical bonds.

Thus, we demonstrated that the use of a beam of energetic oxygen atoms allows one to drastically increase the degree of copper oxidation and the growth rate of cupric oxide. This cuts the thermal budget and reduces the diffuseness of heterojunctions in layered structures.

ACKNOWLEDGMENTS

This work was supported by the Research Program "Physics of Solid State Nanostructures," project no. 97-3005.

REFERENCES

1. Yu. S. Gordeev, P. S. Kop'ev, V. V. Mamutin, *et al.*, Sverkhprovodimost: Fiz., Khim., Tekh. **7**, 1417 (1994).
2. V. V. Mamutin, P. S. Kop'ev, A. V. Zakharevich, *et al.*, Sverkhprovodimost: Fiz., Khim., Tekh. **6**, 797 (1993).
3. V. V. Mamutin, N. F. Kartenko, S. I. Goloschapov, *et al.*, Appl. Phys. Lett. **64**, 2031 (1994).
4. S. E. Sysoev, V. M. Mikoushkin, A. V. Zakharevich, in *Abstracts of 14th European Conference on Surface Science*, *Leipzig, Germany, 1994*, p. 184.
5. E. M. Sher, A. A. Mansurov, V. M. Mikoushkin, *et al.*, in *Proceedings of Second German–Russian Seminar on Physics of Novel Materials*, *St. Petersburg, Russia, 1995*, p. 196.
6. K. U. Wiks and F. E. Block, *Thermodynamic Properties of 65 Elements—Their Oxides, Halides, Carbides, and Nitrides* (United States Department of the Interior; Metallurgiya, Moscow, 1965), pp. 70–71.

Translated by A. Chikishev

Technical Physics, Vol. 45, No. 3, 2000, pp. 369–373. Translated from Zhurnal Tekhnicheskoĭ Fiziki, Vol. 70, No. 3, 2000, pp. 82–86.
Original Russian Text Copyright © 2000 by Tarnavskiĭ, Shpak.

BRIEF COMMUNICATIONS

Quasi-Periodic Relaxation to a Steady Flow Regime after Pulsed Energy Input into the Incoming Stream

G. A. Tarnavskiĭ and S. I. Shpak
Institute of Theoretical and Applied Mechanics, Siberian Division, Russian Academy of Sciences,
ul. Institutskaya 4/1, Novosibirsk, 630090 Russia

Received June 30, 1998; in final form, February 16, 1999

Abstract—Numerical simulation was used to analyze the quasi-periodic process induced against the steady flow pattern around a blunt forebody by a pulse from an external source located in the incoming stream. © *2000 MAIK "Nauka/Interperiodica".*

Analysis of new methods of vehicle motion control through external energy input into the incoming gas stream is a current topic of substantial interest. Experimental [1–6], analytical [7, 8], and computational [9–17] studies of the effects of parameters of steady or pulsed periodic sources (such as their location, geometry, intensity, and frequency spectra) on the flow structure and aerodynamic characteristics of vehicles have been performed. Interesting phenomena discovered and analyzed in these studies include the formation of circulation flow regions at the nose of the body and considerable reduction of wave drag (for certain combinations of flow parameters). The most realistic and feasible method of energy deposition in the incoming stream can be executed by means of focused high-frequency laser light pulses [4, 5].

In this paper, we present some results of a numerical study of the passage of the first pulse, which substantially modifies and restructures the steady supersonic flow pattern around a blunt forebody. We performed numerous computational experiments with the following statement of the problem. We analyzed the flow of a spherical nose of a cylindrical or conical forebody placed in a supersonic stream of a viscous heat-conducting gas. In the region bounded by the surface of a thermally insulated body, the bow wave (whose location and geometry were computed in the course of the solution), the symmetry axis, and the downstream boundary, we numerically integrated the Navier–Stokes equations, written in the conventional dimensionless form with the parameters M_∞, Re_∞, Pr, and γ, by the first-order accurate in time and second-order accurate in space method described in [18, 19]. Here, M_∞ and Re_∞ are the free-stream Mach and Reynolds numbers, respectively; Pr is the Prandtl number; and γ is the ratio of specific heats. The system was closed by the equation of state for a perfect gas with a variable γ and nondimensionalized by using the nose radius R, density ρ_∞, velocity U_∞, and their combinations as reference parameters. This unambiguously defines the dimensional form of the dimensionless quantities considered below.

The steady flow pattern was perturbed by energy release pulses with intensity I and repetition period T, $E(x, t) = I\delta(\omega t - kx)$, carried by the incoming stream and characterized by a steep leading and trailing edges. Here, δ is the unit pulsed function (Durac's delta function),

$$\delta(z) = \begin{cases} 1; & z = \pm 0, 1, 2, \ldots \\ 0; & z \neq \pm 0, 1, 2, \ldots, \end{cases}$$

and the frequency ω, wavenumber k, and wavelength L are related to T and U_∞ as $\omega = 2\pi/T$, $k = 2\pi/L$, and $L = U_\infty T$.

Time was measured from the moment when the first pulse reached the bow wave. The analysis below mainly concerns the transient process of flow restructuring in the interval $0 \le t < T$ between the first and second pulse incidences. This model was used in a computational experiment to facilitate analysis of the physical mechanisms of the onset and development of an unsteady (probably quasi-periodic) regime involving essentially different stages. It provides a complementary alternative to the statement of the problem analyzed in [9–14], where a high-energy distributed hot spot located ahead of the body protected it from the incoming stream.

Figures 1a–1h show the typical result of a numerical experiment performed to simulate the principal stages of the quasi-periodic process induced by the passage of the first pulse and the corresponding spatiotemporal evolution of the flow pattern. An external pulse interacting with the bow wave gives rise to the two-wave pattern of "shock disintegration" (here, contact discontinuities are not considered and their evolution is not monitored). The new bow wave moves upstream and rapidly reaches a steady state. Inside the perturbed region, an inner shock wave is generated (a), which then moves toward the body (b). Its angle of inclination

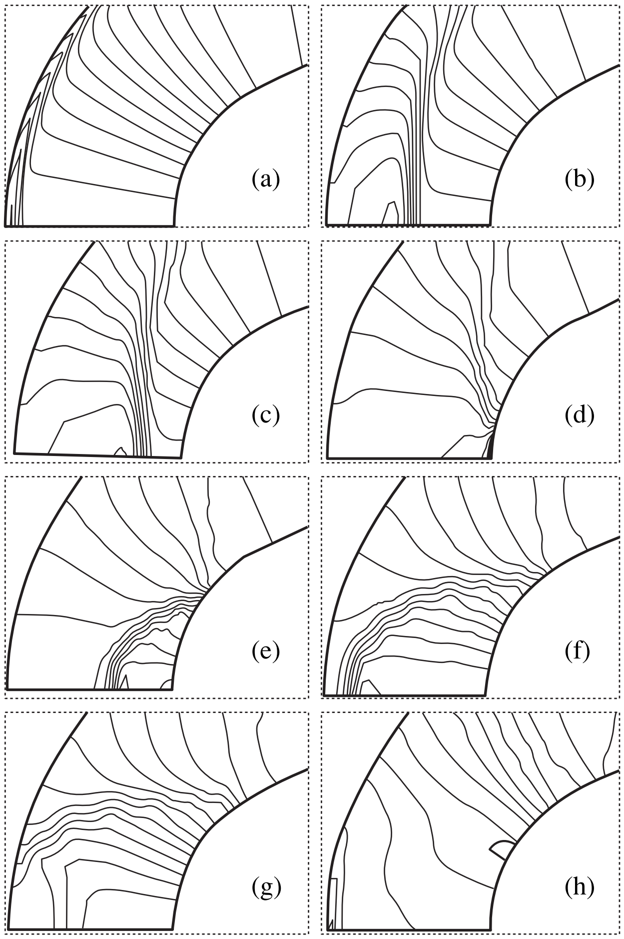

Fig. 1. Fragments of flow field (isobars) for $M_\infty = 10$, $Re_\infty = 0.83 \times 10^5$, and $I = 1.7$. The length scale is increased by a factor of 2 along the normal to the body; $t = 0.003$ (a), 0.1 (b), 0.15 (c), 0.2 (d), 0.3 (e), 0.4 (f), 0.5 (g), and 0.75 (h).

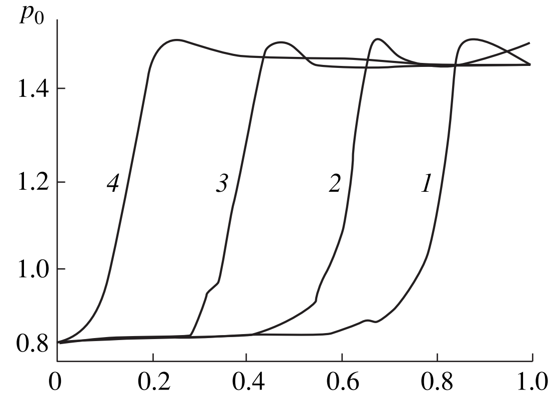

Fig. 2. Pressure distribution along the symmetry axis from the bow wave ($x = 0$) to the body ($x = 1$) at $t = 0.25$ (*1*), 0.3 (*2*), 0.35 (*3*), and 0.4 (*4*).

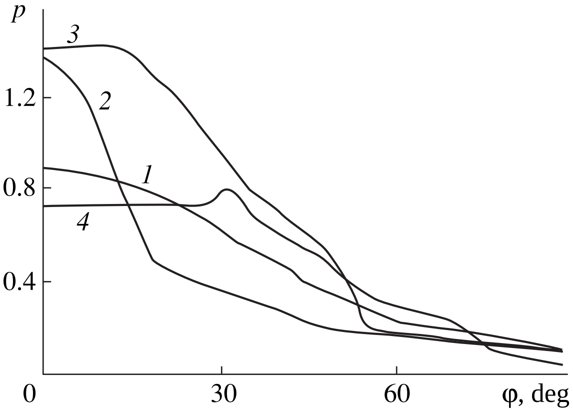

Fig. 3. Pressure distribution over the body surface at $t = 0.003$ (*1*), 0.2 (*2*), 0.4 (*3*), and 0.75 (*4*).

to the streamwise axis of the flow changes (c), which leads to flow reversal behind the front. Then, the inner shock wave reaches the curved body surface (d), is reflected from it (e), and returns to the bow wave (f). At the same time, a region of elevated pressure develops behind the inner-shock front, exceeding its steady-flow counterpart in amplitude and dimensions (the corresponding drag coefficient being higher than the steady-flow value by 40%). This leads to an increase in the velocity component tangential to the surface and a “piston” effect that drives the gas outwards (g). After that, the flow in the neighborhood of the nose is drastically restructured (h): the peak pressure is shifted downstream of the body nose (as marked by the thick isobar in Fig. 3), while an extensive pressure plateau appears in the neighborhood of the nose, where a circulation flow region with a steady-flow pattern similar to those shown in [9, 14, 17] develops. Note that the drag coefficient at this moment is lower than its steady-flow value by 30%. The inner shock that has reached the bow wave is reflected by it and moves back toward the body. This process is repeated, substantially decaying, over several cycles, depending on the input parameters; and the flow tends to its steady regime with low-amplitude “long-lived” pulsations.

Figure 2 shows a detailed illustration of the inner shock returning from the body to the bow wave. Here, pressure distributions along the symmetry axis of the problem are presented. Curve *1* corresponds to the initial moment of departure of the reflected inner shock from the body, curve *4* represents the inner shock approaching the bow wave, and curves *2* and *3* illustrate intermediate stages. In brief, the basic features of the process are as follows. First, the shock-front steepness and velocity remain approximately constant, signifying that the background flow ahead of the front is rather uniform. Second, the flow field behind the front is uniform, with an amplitude almost independent of time (in the interval shown here); that is, the flow is dominated by dynamics that are normal, rather than tangential, to the body.

It should be noted that a rather high pressure is observed in the vicinity of the axis immediately after the inner shock is reflected and starts moving away from the body. As the peripheral portion of the curved inner-shock front advances along the body surface, the flow rapidly expands and the pressure (as well as density) noticeably drops in the region bounded by the stagnation point and the symmetry axis (the "piston" effect of a shock drives the gas outwards).

Figure 3 shows the pressure distribution over the body surface as a function of the polar angle φ at various times during the first cycle. Curve *1* represents the steady distribution at the initial moment (which corresponds to Fig. 1a); curve *2*, the initial moment of reflection of the shock incident on the body surface (see Fig. 1d); curve *3*, the inner shock moving from the body toward the bow wave (see Fig. 1f); and curve *4* corresponds to the moment of return of the inner shock from the bow wave to the body (Fig. 1h), illustrating the shift of the pressure peak downstream of the body nose. Later on, the development of a reverse-flow region originates at a location lying between these points.

Figures 4a–4h show lines of constant flow pressure illustrating the basic stages of the second temporal cycle of the inner-shock movement and the spatiotemporal evolution of the flow pattern by analogy with that illustrated by Fig. 1. Here, the inner-shock intensity is obviously lower than that observed in the first cycle. Accordingly, it is less easily visualized and is highlighted in each panel as a thick isobar lying in the domain of peak pressure gradient within a somewhat "diffuse" front of the inner shock.

Figure 4a is completely analogous to Fig. 1h: having reached the bow wave in the first cycle, the inner shock is reflected by it, moves back toward the body across a region that is more uniform than in the first cycle (Figs. 4b, 4c), and again hits the body surface (Fig. 4d). Between the bow wave and the inner shock, an extensive region of constant pressure appears, which is easy to see in Fig. 4d, as it contains no isobars. Then, the curved inner shock is reflected by the body (Fig. 4e) and moves toward the bow wave and downstream along the body surface (Fig. 4f). Here, as in the first cycle, we again observe the "piston" effect driving the gas out of the neighborhood of the body nose (Fig. 4g) and a rather extensive region of uniform pressure develops here, initiating the formation of a circulation flow region in the vicinity of the stagnation point (note the isobars closing up at the symmetry axis). Then, the inner shock hits the bow wave (Fig. 4h) and this completes the second cycle.

Subsequent cycles basically repeat the first two, differing in some details. The decrement of the inner shock is determined by the dissipative properties of the fluid (mainly by the Reynolds number) and, to a lesser extent (in the range of parameters explored), by the temperature condition on the body surface. The respective cycle durations are 0.7 and 0.66. Thus, when the flow is perturbed by pulses with period $T = 0.68$ (for the given parameters of the problem), one may be able to produce interesting resonance phenomena by pumping energy into a decaying quasi-periodic process.

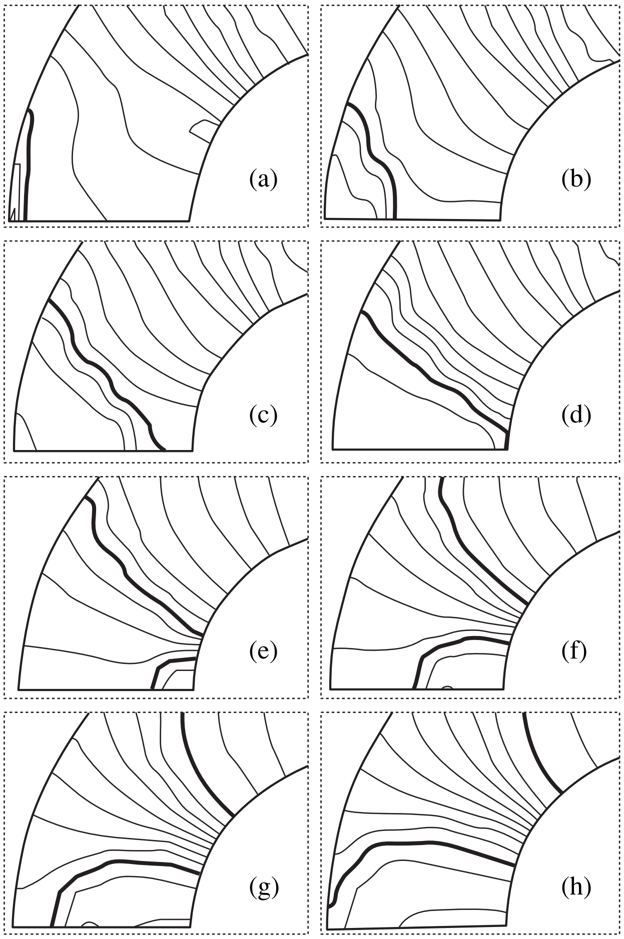

Fig. 4. Fragments of flow field (isobars) for $M_\infty = 10$, $Re_\infty = 0.83 \times 10^5$, and $I = 1.7$. The length scale is increased by a factor of 2 along the normal to the body; $t = 0.75$ (a), 0.8 (b), 0.85 (c), 0.9 (d), 0.95 (e), 1.0 (f), 1.05 (g), and 1.1 (h).

Figure 5 shows pressure distributions along the symmetry axis at various moments illustrating the pattern of oscillatory motion of the inner shock from the bow wave to the body and back during the first two cycles of the quasi-periodic process. Curves *1* and *3* correspond to the motion of the inner shock toward the body, while curves *2* and *4* represent its motion away from the body during the first two cycles. In particular, for these values of parameters, the average intensities of the shocks that move toward the body are 1.56 and 1.13 in the first and second cycles, respectively, while the corresponding intensities of reflected shocks are 1.76 and 1.19.

Figure 6 shows local and integral aerodynamic characteristics of the body, namely, the stagnation pressure p_0 (at the body nose) and the total (wave plus viscous)

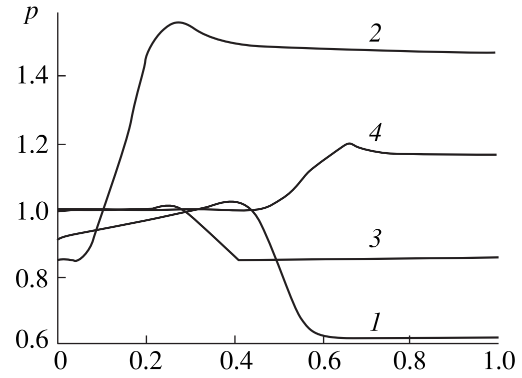

Fig. 5. Pressure distribution over the body surface at $t = 0.1$ (*1*), 0.4 (*2*), 0.8 (*3*), and 1.0 (*4*).

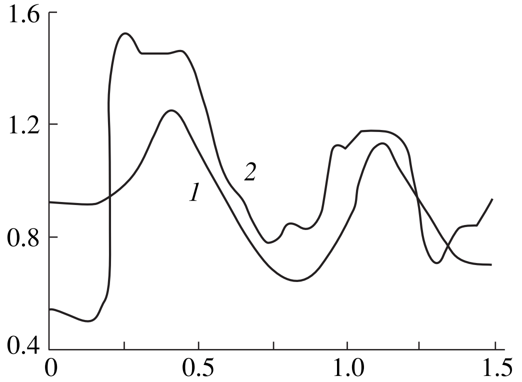

Fig. 6. Evolution of aerodynamic characteristics: (*1*) stagnation pressure p_0; and (*2*) drag coefficient C_x.

drag coefficient C_x, including their quasi-periodic temporal dynamics. One can single out several characteristic stages in the cyclic process that are specific to p_0 and C_x.

Let us consider the principal stages of p_0 evolution. A sharp rise in p_0 occurs at the moment of incidence of the inner shock on the body surface and during the initial stage of its reflection from the body. The value of p_0 increases by almost 70% over its previous background value. This is followed by a rather extensive temporal plateau of high p_0. This stage of the cycle corresponds to an interval when the inner shock moves from the body to the bow wave. Then, the "piston" effect associated with the advancement of the peripheral portion of the shock along the body surface begins to affect p_0, leading to its subsequent substantial decrease. This corresponds to the time interval when the inner shock returns from the bow wave to the body. It hits the body surface and is reflected by it, and the cyclic process is repeated for a somewhat different p_0.

Similar stages of a cyclic process are characteristic of C_x as well, but with two essential distinctions. First, since the drag coefficient C_x is an integral characteristic, its evolution (as compared to that of the local characteristic p_0) proceeds in a smoother manner and the sharp jumps in p_0 are damped. Second, the entire dynamics of C_x is slightly phase-shifted relative to that of p_0. In particular, the peak of p_0 at the moment of reflection of the inner shock by the body does not produce any peak in the drag coefficient C_x, because pressure is lowered over the entire body surface by the "piston" effect of the preceding cycle and the value of C_x is primarily determined by the integral of pressure over the body contour (with the orientation of the normal relative to the x-axis taken into account). Note that the contribution of the "viscous" component (which has an even greater damping effect on the peaks of flow characteristics) to the total C_x is no higher than 5% for a given M_∞ and Re_∞.

A quasi-periodic flow pattern of the type described here suggests that some resonance phenomena should be expected to occur when the external pulse recurrence frequency is adjusted in a special manner [20], and a moderate power input can lead to a substantial flow instability and development of significant pitching moments.

These phenomena can be used to design new methods for flow control around a body (see also some theoretical sketches in [4–7, 10, 13–17]). Even though the thermodynamic efficiency of sustaining a permanent "aerodynamic needle" for improving aerodynamic characteristics and reducing thermal loads in steady flight regimes seems questionable at the present time, this approach may prove to be effective in executing some vehicle maneuvers in a pulse-boosted regime.

REFERENCES

1. V. V. Vitkovskiĭ, G. N. Grachev, N. N. Gritsov, *et al.*, Teplofiz. Vys. Temp. **28**, 1156 (1990).
2. V. I. Artem'ev, V. I. Bergel'son, I. V. Nemchinov, *et al.*, Izv. Akad. Nauk SSSR, Mekh. Zhidk. Gaza, No. 6, 146 (1990).
3. G. I. Mishin, A. I. Klimov, and A. Yu. Gridin, Pis'ma Zh. Tekh. Fiz. **18**, 86 (1992).
4. P. K. Tret'yakov, G. N. Grachev, A. I. Ivanchenko, *et al.*, Dokl. Ross. Akad. Nauk **336**, 466 (1994).
5. P. K. Tret'yakov, A. F. Garanin, G. N. Grachev, *et al.*, Dokl. Ross. Akad. Nauk **351**, 339 (1996).
6. V. I. Bergel'son, S. V. Medvedyuk, I. V. Nemchinov, *et al.*, Mat. Model. **8**, 3 (1996).
7. S. I. Arafaĭlov, Izv. Akad. Nauk, Mekh. Zhidk. Gaza, No. 4, 178 (1987).
8. P. Yu. Georgievskiĭ and V. A. Levin, Tr. Mat. Inst. im. V.A. Steklova **186**, 197 (1989).
9. P. Yu. Georgievskiĭ and V. A. Levin, Pis'ma Zh. Tekh. Fiz. **14**, 684 (1988).
10. Yu. P. Golovachev and N. V. Leont'eva, Izv. Akad. Nauk, Ser. Mekh. Zhidk. Gaza, No. 2, 186 (1989).

11. Yu. P. Golovachev and N. V. Leont'eva, Zh. Vychisl. Mat. Mat. Fiz. **29**, 148 (1989).
12. Yu. P. Golovachev and N. V. Leont'eva, Zh. Vychisl. Mat. Mat. Fiz. **29**, 791 (1989).
13. N. V. Pogorelov, Izv. Akad. Nauk, Mekh. Zhidk. Gaza, No. 6, 130 (1990).
14. V. Yu. Borzov, I. V. Rybka, and A. S. Yur'ev, Inzh.-Fiz. Zh. **67**, 355 (1994).
15. Yu. P. Golovachev, *Numerical Simulation of Viscous Gas Flows in a Shock Layer* (Nauka, Moscow, 1996).
16. S. V. Guvernyuk and A. B. Samoĭlov, Pis'ma Zh. Tekh. Fiz. **23**, 1 (1997).
17. V. A. Levin, N. A. Afonina, P. Yu. Georgievskiĭ, *et al.*, Preprint No. 24, IM MGU (Institute of Mechanics, Moscow State Univ., 1997).
18. G. A. Tarnavskiĭ, Chislennye Metody Mekh. Sploshnoi Sredy **10**, 128 (1979).
19. M. K. Lebedeva, A. E. Medvedev, and G. A. Tarnavskiĭ, Avtometriya, No. 5, 76 (1994).
20. P. K. Tret'yakov, A. V. Tupikin, and V. I. Yakovlev, Preprint No. 9, ITPM SO RAN (Institute of Theoretical and Applied Mechanics, Siberian Division, Russian Academy of Sciences, 1997).

Translated by A. S. Betev

Technical Physics, Vol. 45, No. 3, 2000, pp. 374–376. Translated from Zhurnal Tekhnicheskoĭ Fiziki, Vol. 70, No. 3, 2000, pp. 87–89.
Original Russian Text Copyright © 2000 by Konshina.

BRIEF COMMUNICATIONS

A Correlation between Electrical and Optical Properties of a-C : H Films

E. A. Konshina

Vavilov State Optical Institute, All-Russia Research Center,
ul. Babushkina 36/1, St. Petersburg, 193171 Russia

Received October 6, 1998

Abstract—a-C : H films deposited from pure acetylene vapor in a glow-discharge plasma were investigated. Current density vs. applied voltage plots are presented for systems consisting of a transparent conducting electrode, an a-C : H film, and a mercury contact. The resistivity, absorption coefficient at a wavelength of 632.8 nm, and the optical energy gap of a-C : H films are related to the deposition rate. *© 2000 MAIK “Nauka/Interperiodica”.*

Visible-light-absorbing films of amorphous hydrogenated carbon (a-C : H) are finding application as light-blocking layers in light-controlled liquid-crystal reflection modulators [1]. This is a new solution to the problem of optically isolating write and reading radiations. Optical and electrical properties of a-C : H films depend on their structure and preparation conditions [2]. a-C : H light-blocking layers with optimum properties can be produced if the range of parameters for glow-discharge plasma deposition is known. This calls for further investigation of the electrical and optical properties of a-C : H films.

In this work, we study the dependence of the current density on the applied voltage for transparent conducting electrode/a-C : H/metal structures. Dependences of the a-C : H resistivity, absorption coefficient at a wavelength of 632.8 nm, and optical gap on the deposition rate are presented.

a-C : H films were prepared by chemical vapor deposition in a dc glow-discharge plasma. The plasma was produced with a planar magnetron [3]. Such a system, unlike a conventional diode one, provides high gas ionization and requires a lower-pressure vacuum reactor. The voltage U between the anode and the cathode (substrate carrier) varied between 700 and 900 V. The anode–cathode distance was 50 mm. The electrodes and a glass insulating cylinder form a quasi-closed volume to which an operating gas, pure acetylene, was applied. The gas pressure P in the chamber varied between 0.02 and 0.08 Pa. The films were deposited at room temperature onto glass substrates covered by an ITO transparent conducting electrode. The film thickness was measured with an MII-4M microinterferometer. The relative error was 10%. The film thickness was in the range of 0.1–0.3 μm. The deposition rate was determined as the film thickness–deposition time ratio.

A mercury droplet (Fig. 1a) was used as a metal contact in measuring current density I vs. applied voltage V dependences. The contact area was ~10^{-2} cm^2. Figure 1b shows a dark I–V curve for an a-C : H film with a resistivity $\rho = 2 \times 10^9$ Ω cm. I–V curves for all ITO/a-C : H/Hg systems were symmetric if ρ of the a-C : H films fell into the 7×10^8 Ω cm–1×10^{12} Ω cm range. Symmetric I–V characteristics for positive and

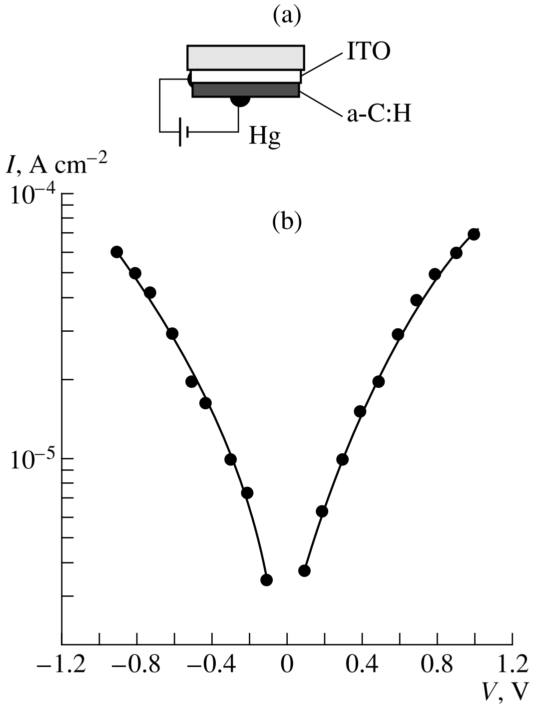

Fig. 1. (a) Substrate/ITO/a-C : H/Hg contact structure and (b) the current density I plotted against applied voltage U for an a-C : H film with $\rho = 2 \times 10^9$ Ω cm.

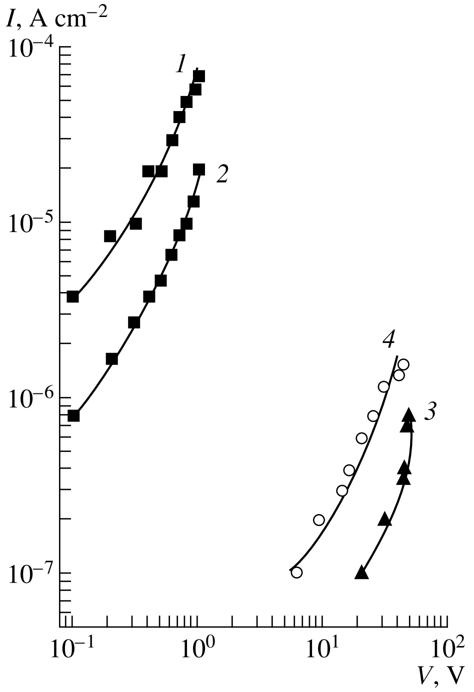

Fig. 2. Dark *I*–*V* characteristics for ITO/a-C : H/Hg structures with a-C : H films obtained from the acetylene plasma at a constant discharge power $N = 3 \pm 0.2$ W and a pressure P = (*1*) 0.03, (*2*) 0.05, and (*3*) 0.05 Pa; (*4*) N = 5.4 W and P = 0.08 Pa.

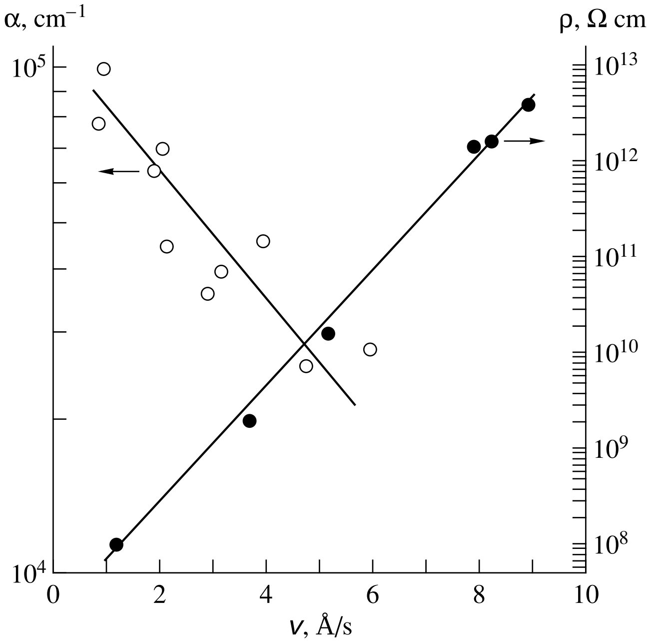

Fig. 3. Absorption coefficient α at 632 nm and the resistivity ρ vs. deposition rate v for a-C : H films obtained from the acetylene plasma.

negative applied voltages were also observed for metal/a-C : H/metal structures with Al and Cr upper contacts [4]. This indicates that the current in these structures does not depend on the contact electronegativity and is related to the a-C : H electron structure.

Figure 2 shows *I*–*V* curves for ITO/a-C : H/Hg contact systems with positive voltages applied to *a*-C : H films obtained under different conditions. As the pressure in the vacuum chamber increases from 0.03 (curve *1*) to 0.05 Pa (curve *2*) with the discharge power remaining constant ($N = 3 \pm 0.2$ W), the current density decreases at the same positive voltages. A further increase in P to 0.08 Pa at the same power leads to a substantial rise in the threshold voltage (curve *3*). Similar changes are observed when the discharge power rises to 5.4 W due to an increase in the voltage at P = 0.05 Pa (curve *4*). At different parameters of acetylene plasma deposition, the Taus optical gap E_T, which is determined by extrapolating an $(\alpha E)^{1/2}$ vs. E dependence, varied from 0.8 to 2.3 eV [5].

With increasing deposition rate v, the absorption coefficient α at a wavelength of 632.8 nm drops from 1×10^5 to $\sim 1 \times 10^4$ cm^{-1} (Fig. 3) and the light blocking efficiency of an a-Si : C : H semiconducting layer degrades [1]. This is due to a substantial effect of deposition rate on a-C : H optical constants [6, 7]. We succeeded in obtaining a resistivity vs. deposition rate dependence. As v grows from 1 to 10 Å/s, ρ exponentially rises by six orders of magnitude to $\sim 10^7$ Ω cm. For $10^8 < \rho < 10^{10}$ Ω cm, a-C : H films become conducting and have an energy gap of ~1 eV. For $v > 5$ Å/s, a-C : H insulating films are transparent in the visible range and have $E_T \sim 1.6$–2.0 eV. Figure 3 is an indication that a film satisfying light-blocking conditions and having an absorption coefficient of $\sim 5 \times 10^4$ cm^{-1} must have $\rho \sim 10^{10}$ Ω cm. This is consistent with the conductivity value of a liquid-crystal layer and provides high spatial resolution of a liquid-crystal modulator. Such light-blocking layers can be made by acetylene vapor condensation in a plasma at rates from 3 to 5 Å/s.

Thus, it was shown that dark *I*–*V* dependences of a-C : H films depend considerably on the pressure in the vacuum chamber and on the power of a dc glow discharge. The resistivity of the films is related to the deposition rate in the interval of 1–10 Å/s: as the rate increases, so does ρ from $\sim 10^7$ to $\sim 10^{13}$ Ω cm. The transparency of the films at a wavelength of 632.8 nm also rises. Light-absorbing a-C : H films with $\alpha \sim 5 \times 10^4$ cm^{-1}, used for light blocking in liquid-crystal modulators, have $\rho \sim 10^{10}$ Ω cm and an optical gap of ~1 eV. The results obtained can be used for fabricating liquid-crystal light modulators applied in systems for optic data transmission, conversion, recording, and processing.

REFERENCES

1. E. A. Konshina and A. P. Onokhov, Zh. Tekh. Fiz. **69** (3), 80 (1999) [Tech. Phys. **44**, 340 (1999)].
2. J. Robertson, Thin Solid Films **296**, 61 (1997).
3. A. V. Balakov and E. A. Konshina, Zh. Tekh. Fiz. **52**, 810 (1982) [Sov. Phys.—Tech. Phys. **27**, 521 (1982)].
4. S. Egret, J. Robertson, W. I. Milne, *et al.*, Diamond Relat. Mater. **6**, 879 (1997).
5. E. A. Konshina, Fiz. Tverd. Tela (S.-Peterburg) **37**, 1120 (1995).
6. E. A. Konshina and V. A. Tolmachev, Zh. Tekh. Fiz. **65**, 175 (1995) [Tech. Phys. **40**, 97 (1995)].
7. V. A. Tolmachev and E. A. Konshina, Diamond Relat. Mater. **5**, 1397 (1996).

Translated by V. A. Isaakyan

Technical Physics, Vol. 45, No. 3, 2000, pp. 377–379. Translated from Zhurnal Tekhnicheskoĭ Fiziki, Vol. 70, No. 3, 2000, pp. 90–92.
Original Russian Text Copyright © 2000 by Evard, Sidorov, Gabis.

BRIEF COMMUNICATIONS

Hydrogen Permeability of Amorphous and Recrystallized Iron Alloys

E. A. Evard*, N. I. Sidorov, and I. E. Gabis***
** Research Institute of Physics, St. Petersburg State University, St. Petersburg, 198904 Russia*
*** Institute of Metallurgy, Ural Division, Russian Academy of Sciences, Yekaterinburg, 620016 Russia*

Received March 12, 1999

Abstract—The hydrogen permeability of amorphous and recrystallized Fe alloys is investigated. It is found that the surface layers of both samples are enriched with metalloids, which interfere with the penetration of hydrogen from the molecular and atomic phases. The kinetics of curves of flow transition to a steady state upon ion irradiation in an amorphous alloy points to processes of reversible capture. The penetrating flow demonstrates Arrhenius dependence on temperature in the case of recrystallized samples and nonmonotonic dependence on temperature in the case of amorphous samples. A model of hydrogen penetration is suggested, which includes the reemission and diffusion processes; and estimates are obtained of the energy of activation of thermodesorption and diffusion. *© 2000 MAIK "Nauka/Interperiodica".*

Amorphous alloys differ from classical metals by the absence of ordered crystal lattice, which must lead to singularities of diffusion of interstitial impurities. Unfortunately, published data on diffusion in amorphous materials are scarce because of serious experimental difficulties associated with the need for performing measurements in a narrow temperature range (see, for example, [1–3]).

EXPERIMENT

We have investigated the hydrogen permeability of a membrane of amorphous and recrystallized iron alloys (Fe, 77.3; Ni, 1.1; Si, 7.7; B, 13.6; C, 0.2; P, 0.009) 25 μm thick. Preliminary degassing of a sample in vacuum was performed at a temperature of 300°C. Continuous annealing at a high temperature results in the formation of a polycrystalline structure with a characteristic grain size of 1 μm.

The steady flow time relaxation method was used to determine the parameters of diffusion. The admission of molecular hydrogen to the inlet side of a degassed sample at the maximum permissible temperature (300°C for amorphous and 400°C for recrystallized) did not result in a marked increase in the outward flow: for a hydrogen pressure of 10 torr, the flow amounted to 3.8×10^{12} cm^{-2} s^{-1}. It is known that the coefficient of attachment for hydrogen atoms is three to four orders of magnitude higher than for molecules [4]. However, the use of a dissociator (an incandescent tungsten filament at a distance of 10 mm from the sample) in the pressure range of 0.1–0.2 torr also failed to produce an appreciable penetrating flow.

Images of the surface of an amorphous strip in secondary electrons (200 and 800 magnification) demonstrated the presence of microswellings, which is associated with the process of capture of air bubbles during strip formation. It is further known [5] that iron alloys containing Si and B exhibit a tendency to enrichment of surface layers with these elements, which may prevent the adsorption and penetration of hydrogen into the bulk of material.

A glow discharge in an atmosphere of hydrogen was used for moving across the passivating layer. Hydrogen ions formed in the glow discharge penetrated easily into the bulk of the sample [4]. In so doing, we observed a marked penetrating flow. All investigations were performed at an inlet pressure of hydrogen of 2 torr, at which the discharge is most stable.

The temperature dependences of the steady-state flow were determined for amorphous and recrystallized samples. The measurement results are given in Fig. 1. One can see that, as the temperature in the amorphous material rises, the flow increases to reach the maximum value of 3.3×10^{13} cm^{-2} s^{-1} at 200°C and, on further heating, exhibits an anomalous decrease. The recrystallized sample follows the classical Arrhenius dependence with an activation energy of 17.9 kJ/mol and a maximum flow of 2.7×10^{13} cm^{-2} s^{-1} at 375°C.

The transition of flow to a steady state proceeds differently in different samples. In both cases, in the entire investigated temperature range, a fast phase shows up with characteristic times of transition to a steady state of the order of 30–60 s. For the amorphous membrane, after the fast phase (Fig. 2) at temperatures ranging from 125 to 225°C, a very slow rise in the outward flow is observed with the time of transition to a steady state of the order of 6000 s. A temperature rise leads to the disappearance of the slow component of penetrating flow and its general decrease.

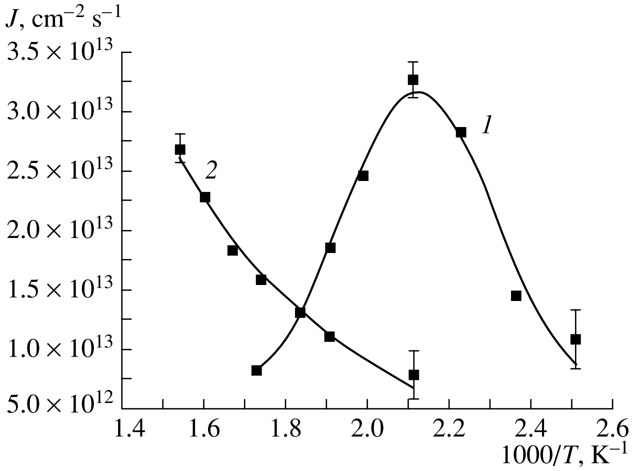

Fig. 1. The penetrating flow as a function of inverse temperature: (*1*) amorphous sample, (*2*) recrystallized sample.

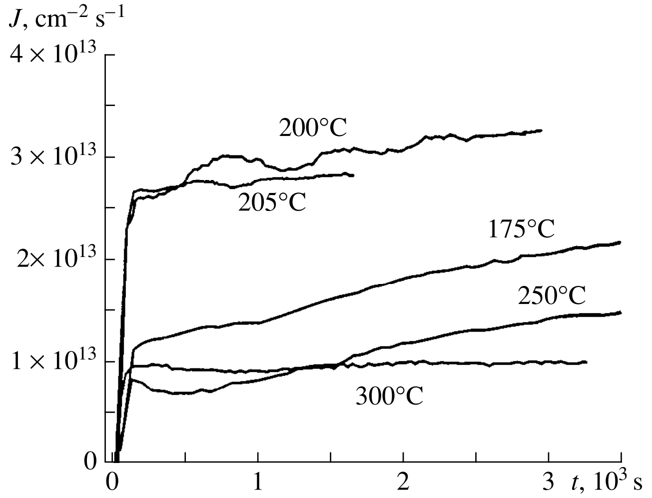

Fig. 2. The kinetics of transition of penetrating flow in an amorphous Fe alloy to a steady state.

DISCUSSION OF THE RESULTS

A delay in the establishment of a steady-state flow is most likely associated with the reversible capture of the diffusant [6]; in this case, as the temperature increases, the probability of release of hydrogen from the traps increases faster than the probability of capture. Indeed, as the temperature rises, an increase in the slow component is observed up to 200°C, after which it starts to decrease; it is this behavior that is characteristic of traps with the energies of activation of release and capture $E_{\mathrm{rel}} > E_{\mathrm{trap}}$.

A decrease in the penetrating flow in the amorphous sample as the temperature rises from 200 to 300°C may be attributed to the surface processes under conditions of ion irradiation. The absorption of relatively low-energy (~200 eV) hydrogen ions occurs at a distance of 30–70 Å from the surface [7]. Because the penetrating flow is three orders of magnitude less than that incident on the inlet surface ($\nu_f \sim 10^{16}$ cm^{-2} s^{-1}), the balance of flows is written as $\nu_f = \nu_m + \nu_r$, where $\nu_r = \nu_f C_1/C_{\max}$ and $\nu_m = b_1\exp(-E_1/RT)C_1$ are the flows of ion-induced remission and thermodesorption on the inlet side, C_1 is the concentration of hydrogen in the undisturbed alloy structure in the vicinity of the inlet surface, and b_1 is the preexponential factor. The maximum attainable concentration in the surface layer $C_{\max}$ at 300 K (when thermodesorption is insignificant) is estimated at 10^{18} atoms/cm^3 [8, 9]. We assume that the concentration C_2 on the outlet side is much less than C_1 to derive for steady-state penetrating flow an expression of the form $J = A\exp(-E_d/RT)/(1 + B\exp(-E_1/RT))$, where E_d is the energy of activation of diffusion. The equation does not include the parameters of hydrogen interaction with traps, because, in the steady state, the capture and release of the diffusant proceed at the same rates and do not affect the magnitude of steady-state flow. The approximation results are given in Fig. 1 by solid curves. A fairly good agreement with the experimental data is exhibited by the energy values of $E_d^{\mathrm{am}} = 40.8$ and $E_I^{\mathrm{am}} = 86.7$ kJ/mol for the amorphous sample and $E_d^{\mathrm{er}} = 71.2$ and 51.7 kJ/mol for the crystalline sample. The use of the parameter $C_{\max}$ in the calculation has no effect on the activation energies: it affects only the preexponential functions.

Therefore, the surface processes and the correlation between the quantities E_d and E_I define the temperature dependence of steady-state flow. In the case of an amorphous alloy, the concentration C_1, according to calculations, has the value $C_{\max}$ up to a temperature of ~170°C and the rate of penetration is defined by diffusion, with the flow increasing. As the temperature continues to rise, the concentration C_1 drops exponentially and the inequality $E_d < E_I$ leads to a decrease in the flow. For a recrystallized alloy, the input concentration decreases within the entire temperature range and the inequality $E_d > E_I$ leads to the classical Arrhenius dependence $J \sim \exp(-E_a/RT)$, where $E_a = E_d - E_I \sim 19.6$ kJ/mol according to our calculation results, which is close to $E_a = 17.9$ kJ/mol (determined experimentally).

The difference in the values of the diffusion activation energy is, no doubt, due to the sample structure. The presence of excess free volume in the amorphous alloy provides for lower consumption of energy during migrations of hydrogen atoms from one interstice to another; in addition, some of the interstices may not have the regular shape of Bernal's cavities [2], but rather may be deformed. The energy of activation of thermodesorption in the recrystallized alloy is less than that in the amorphous alloy; i.e., $E_I^{\mathrm{cr}} < E_I^{\mathrm{am}}$, which may be attributed to rearrangement of the surface and to variation of the effect of the passivating layer on hydrogen desorption. Further investigations are required for detailed determination of the processes of hydrogen penetration.

ACKNOWLEDGMENTS

This study received support from the Integratsiya Federal Support Center, project no. 326.25.

REFERENCES

1. R. Kirchheĭm, F. Summer, and G. Schluckebier, Acta Metall. **30**, 1959 (1982).
2. A. I. Manokhin, *Amorphous Alloys* (Metallurgiya, Moscow, 1984).
3. J. B. Hubbard, T. Nguyen, and D. Bentz, J. Chem. Phys. **96**, 3177 (1992).
4. A. I. Livshits, Zh. Tekh. Fiz. **46**, 328 (1976) [Sov. Phys. Tech. Phys. **21**, 187 (1976)].
5. V. V. Nemoshkalenko, *Amorphous Metal Alloys* (Naukova Dumka, Kiev, 1987).
6. D. G. Herst, *CRRP-1124* (Chalk River, Atomic Energy of Canada, 1962), p. 129.
7. J. F. Ziegler, J. P. Biersack, and U. L. Littmark, *The Stopping and Range of Ions in Solids* (Oxford, Pergamon, 1985).
8. S. A. Grashin, Yu. A. Sokolov, A. E. Gorodetskiĭ, *et al.*, Preprint No. 3622/7, IAE (Inst. of Atomic Energy, Moscow, 1982).
9. Yu. A. Sokolov, A. E. Gorodetsky, and S. A. Grashin, J. Nucl. Mater. **125**, 25 (1984).

Translated by Henri A. Bronstein